ABSTRACT

NEXT-GENERATION FRAGMENT SEPARATORS
FOR EXOTIC BEAMS

Laura Leigh Bandura, Ph.D.
Department of Physics
Northern Illinois University, 2009
Bela Erdelyi, Director

The next generation of nuclear physics research will require advanced exotic beam facilities based on heavy-ion drivers. Exotic beams of rare nuclei will be produced via fragmentation and fission reactions resulting from a high-energy heavy-ion beam hitting a target. A large aperture fragment separator with superconducting magnets is needed for capture, selection, and transport of rare isotopes for experiments.

The code COSY INFINTIY uses powerful differential algebra (DA) methods for computing the dynamics of the beam in the fragment separator. A hybrid map-Monte Carlo code has been developed and added to COSY to calculate beam-material interactions. This code tracks the fragmentation and fission of the beam in target and absorber material while computing energy loss and energy and angular straggling as well as charge state evolution of the beam by implementing auxiliary codes such as ATIMA and GLOBAL. EPAX has been utilized to return the cross-sections of fragmentation products. The special case of fission has been treated by integrating the code MCNPX to accurately predict cross-sections and dynamics of exotic beams produced by a ^{238}U beam incident on a Li or C target.

Fragment separator designs based on optical symmetries and optimized to be aberration-free are presented. For isotope separation, the Bρ-ΔE-Bρ method is used,

requiring the addition of an energy absorber. Shaped surfaces are used in order to reduce optical aberrations, resulting in a high-purity rare isotope beam.

Beam purity is investigated for four rare isotope production mechanisms, namely light and heavy nuclear fragmentation and light and heavy nuclear fission. Each of these presents unique challenges due to the dynamics of the beam and background contamination produced. Optimized fragment separator settings are presented for each production reaction mechanism and purity results are shown after each selection stage. These include a first- and second- stage achromatic selection and gas cell branch with monochromatic wedge.

The hybrid map-Monte Carlo code extensions added to COSY provide an integrated beam dynamics-nuclear processes design optimization and simulation framework that is efficient and accurate. The code may be used to optimize any fragment separator system for the selection of any rare isotope.

NORTHERN ILLINOIS UNIVERSITY
DEKALB, ILLINOIS

AUGUST 2009

NEXT-GENERATION FRAGMENT SEPARATORS FOR EXOTIC BEAMS

By

LAURA LEIGH BANDURA

A THESIS SUBMITTED TO THE GRADUATE SCHOOL

IN PARTIAL FULFILLMENT OF THE REQUIREMENTS

FOR THE DEGREE

DOCTOR OF PHILOSOPHY

DEPARTMENT OF PHYSICS

Thesis Director:
Bela Erdelyi

ACKNOWLEDGEMENTS

I have many people to thank for their help and support over the years. First is my adviser, Bela Erdelyi, who has always provided encouragement and infinite patience. Also, I thank Jerry Nolen and Shashikant Manikonda for providing guidance in my research pursuits. My committee members, Mary Anne Cummings and Philippe Piot, I have to thank for their time and efforts in support of me. Itacil Gomes and Guy Savard have made important contributions to this dissertation. Itacil provided data from MCNPX and Guy contributed data from simulations with the He gas cell.

My friends and family have been there for me in good times and bad. Thank you Mom & Dad, Darren, Olga, Kris, Josh, and Dan!

TABLE OF CONTENTS

Page

LIST OF TABLES

LIST OF FIGURES

LIST OF APPENDICES

Appendix Page

CHAPTER 1

Introduction

This dissertation is a comprehensive study of next-generation fragment separators for exotic beam facilities. Fragment separator designs based on optical symmetries will be discussed. Theory and procedures for optimization of an aberration-free system will be presented. The Bρ-ΔE-Bρ separation method is used, which has required the development of new simulation tools to account for beam-material interactions. A new hybrid map-Monte Carlo code within COSY INFINITY has been developed using the latest auxiliary codes for cross-sections, energy loss, and charge exchange. Transmission and separation purity of various rare isotope beams have been calculated using the code, and optimized fragment separator settings have been found.

1.1. The Need for Rare Isotopes

The atoms that make up the usual matter on earth are predominantly stable. They keep the same number of protons and neutrons over time. The protons and neutrons at the center of the atom make up 99.9% of the mass of the observable universe. In the universe that is less visible to us there are other "exotic" nuclei that determine how the universe evolves. We do not see these nuclei; however,

they are isotopes of the stable forms found on earth. These rare isotopes are radioactively unstable, meaning that they spontaneously decay into other more stable nuclei. The Chart of the Nuclides (Figure 1.1) shows the nuclei as a function of their neutron number and proton number. The nuclei that are stable and have very long half-lives are shown in black. These nuclei make up the everyday matter that we see. The unstable nuclei that have already been discovered are shown in pink. The nuclei shown in the green areas play an important part in determining the chemical composition of the universe. There is very little that is known about the properties of these nuclei [**1**].

A Facility for Rare Isotope Beams (FRIB) would produce a wide variety of beams of these unstable, "rare" isotopes at unprecedented intensities. These beams would allow a new class of experiments to be performed that would help to explain the structure of exotic nuclei which would, in turn, allow a better understanding of the structure of stable nuclei. There are many science drivers for a FRIB. These include nuclear structure and testing new structure concepts, production and properties of superheavy nuclei, and probing neutron skins. In nuclear astrophysics there are questions about the origin of the heaviest elements, the process of explosive nucleosynthesis, and the composition of neutron stars. Also, it is possible to test some fundamental symmetries with rare isotopes. Other scientific applications include stockpile stewardship, materials science, medical research, and nuclear reactors. These areas of research are highlighted in more detail below.

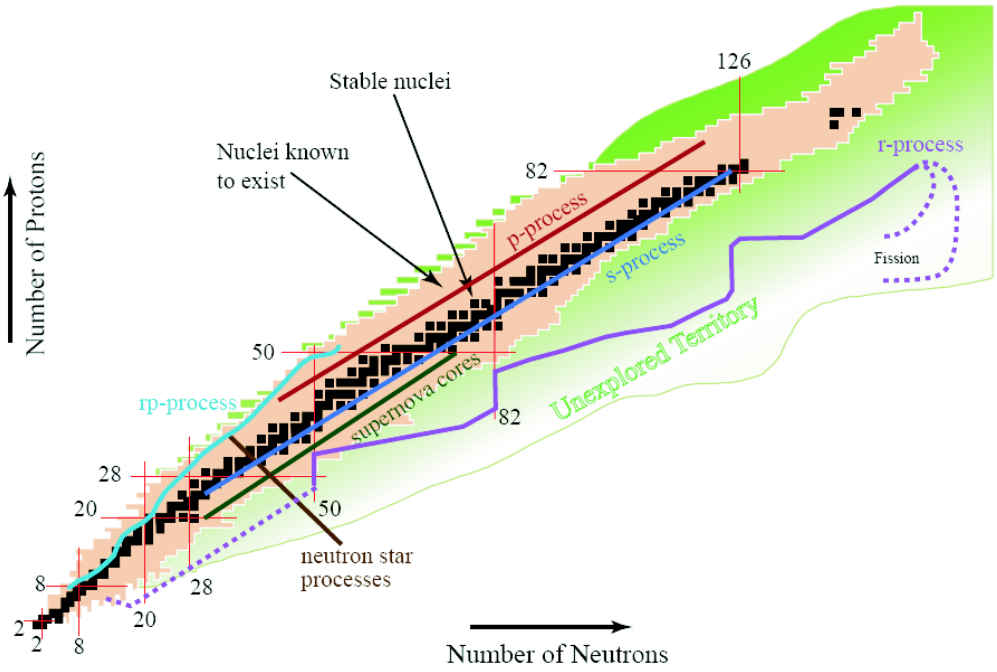

Figure 1.1. Chart of the Nuclides. Represents the nuclei as a function of neutron number and proton number. Nuclei that have very long half-lives and are the most stable are shown in black. Nuclei that have been discovered, but are unstable are shown in pink. Little is known about the nuclei in the green region. They are thought to play an important role in the evolution of the universe.

1.1.1. Nuclear Structure

Nuclear physicists have the need to understand how far the nuclear landscape extends beyond the "valley of stability." How exotic can a nucleus be and still remain bound? An artist's conception of the Valley of Stability is shown in Figure 1.2. The trend that exists in the valley of stability is that for light nuclei in the valley, the neutron number N is approximately equal to the proton number Z. As the number of protons increases, in the valley N is greater than Z since the

Coulomb repulsive force takes over. The walls of the valley of stability are steeper on the proton side because of the repulsive Coulomb interaction in the nucleus. Only a few protons can be added to the nucleus before it becomes unstable and decays. So, the proton dripline is not far from the valley of stability. The slope on the neutron side of the valley is not as steep. This is because, in general, many neutrons can be added to a nucleus without causing it to break apart. With a FRIB, these limits can be probed and many neutron-rich nuclei may be produced. A FRIB may be used to determine the masses of these nuclei and measure their decay modes. Theorists predict that there could be an undiscoverd island of superheavy nuclei that lie beyond the current most massive uranium stable nucleus.

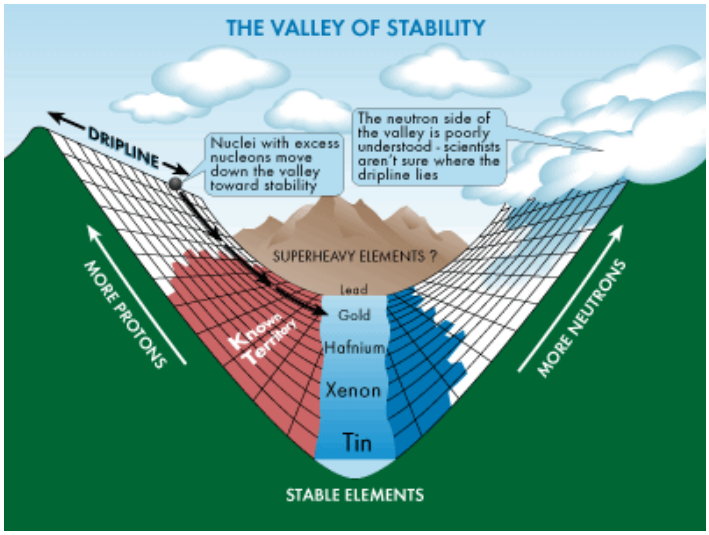

Figure 1.2. Valley of Stability. Represents the stable nuclei (in the valley) and the instability of the isotopes that are either neutron rich or deficient. When more protons are added to a nucleus, the nucleus becomes unstable faster than if more neutrons are added due to the repulsive Coulomb force.

There are many questions that exist relating to the shell structure of the nucleus. With nuclei that have N or Z as magic numbers, there are gaps in the energy spacing and angular momentum of low-lying levels. It is an open question as to whether this is a property just for nuclei near the valley of stability or whether it can be extended further for neutron-rich nuclei. It is thought that some of the known shell gaps can close significantly as the nuclei become neutron-rich and their radii increase. If this behavior is correct, then it will have an influence on the distributions of the heavy elements that are produced in supernovae.

A FRIB will allow nuclear scientists to produce neutron-rich, doubly magic nuclei. This is the case when both N and Z are magic numbers. If the shell gaps in these cases are unusual, then this indicates that the mean field and the interactions of valence nucleons with the rest of the nucleus are different from stable nuclei. These nuclei are probes of the inter-nucleon interaction. The FRIB will be able to produce the short-lived doubly magic nuclei ^{48}Ni, ^{56}Ni, ^{78}Ni, ^{100}Sn, and ^{132}Sn. The task will be to investigate their single-particle structure through one-nucleon transfer and knockout reactions. This will indicate if they exhibit magic shell-structure behavior.

Pairing and superfluidity is important in understanding the structure of a neutron star. This process is described by any attractive interaction between fermions. The fermions become pairs and influence the nuclear structure. At a FRIB one can control the number of nucleons, so pairing can be studied in detail. Scientists wish to study the influence of the pairing on the structure of the neutron-rich nuclei

far from stability. It is in these cases where diffuse neutron-rich "skins" are found. In nuclei with masses greater than 60 that are doubly magic, different superfluid phases may appear. These phases are characterized by nucleonic Cooper pairs carrying different isospin, spin, and total angular momentum.

Neutron skins develop as a result of combined nuclear and electrostatic forces. Nuclei that have a large neutron excess have extended neutron densities that develop as a result of neutrons occupying weakly bound quantum levels. These extended neutron "halos" or "skins" weaken the coupling of the outermost neutrons to the rest of the nucleus. Studying issues such as this with a FRIB will allow for better modeling of the neutron-rich environment of neutron stars.

The production of superheavy nuclei with a FRIB is a very intriguing concept. The heaviest element that exists naturally on earth is uranium. There are heavier elements, however, that may be synthesized in the laboratory or in stellar explosions. A FRIB may be able to synthesize long-lived superheavy nuclei. Quantum theory predicts that individual nucleon orbits in specific nuclear shapes reduce the energy so that they can overcome Coulomb effects and bind the nucleus. The theory also predicts that the neutron-deficient isotope will have a shorter lifetime than that of the neutron-rich isotope. There are discrepencies in the theories for the prediction of where in the N-Z region the superheavy nuclei may exist. A FRIB can play an important role in discovering the best processes by which the superheavy nuclei can be produced. One method that is proposed is to collide two nuclei with summed (N,Z) very near the superheavy candidate and detect

the fusion product. The other method is to collide two neutron-rich nuclei. The system would then decay into a superheavy ground state by evaporation of the excess neutrons.

1.1.2. Nuclear Astrophysics

....A FRIB will be useful for astrophysical applications because it is able to produce extremely high fluxes of unstable nuclei across a wide range of masses and particle separation energies. This quality is useful in studying three areas of the fundamental importance of unstable nuclei. One is the determination of the abundances of the elements and isotopes that are produced in stars and stellar explosions. Another is the necessity to understand the source of the energy generation in these stellar environments. In addition, it is unknown what the behavior of matter is at the extremes of the neutron excess found in neutron stars and supernovae. Each of these issues has yet to be addressed in the nuclear astrophysics community.

The landscape of elements and isotopes have been produced in nuclear explosive processes in stars since the Big Bang. The process of the formation of these nuclei is termed nucleosynthesis. Nucleosynthesis is a chain reaction that produces stable nuclei through the decay processes of less stable nuclei. The environments of novae, supernovae, and x-ray bursts are ideal to produce unstable nuclei because of the large abundances of free protons or neutrons at high temperatures. Supernovae alone can produce about 1500 isotopes by over 15,000 possible reaction channels. More data are needed in order to thoroughly understand these reactions. The

rates for these reactions are mostly theoretical and few measurements exist. A FRIB could help to confirm these theories and to calibrate them.

The nucleosynthesis of the heavy elements can proceed by three processes. These are the r-process (rapid neutron addition), rp-process (rapid proton addition), and the γ-process (photodisintegration reactions). These reactions can occur when there is a large density of free neutrons, γ-rays, or protons at high temperature. The r-process makes neutron-rich isotopes, the rp-process makes neutron-deficient isotopes from mass 60-120, and the γ-process makes heavy neutron-deficient isotopes up to mass 200. The production of nuclei by these processes depends on the binding energies, beta decay lifetimes, and cross-sections of some of the very unstable nuclei. A FRIB could be especially useful in the production of the isotopes involved in the r-process. It would then be possible to measure the decay lifetimes, masses, and other important properties.

The full energy generation process in novae is not completely understood. Initially it is generated from the CNO cycle. Though, as the temperature increases up to about half a billion degrees K, α-capture on the unstable nuclei ^{15}O and ^{18}Ne leads to proton capture sequences that lead to the production of nuclei along the proton drip line as well as energy generation. There is a great dependence of the production rate of the heavier nuclei on the binding energies, lifetimes, and cross-sections of the short-lived proton-rich nuclei. There is great uncertainty in the parameters that describe the α-capture on ^{15}O. With FRIB beam intensities, α scattering experiments can be performed to verify the predicted parameters.

Understanding the properties of exotic nuclei themselves can help us to understand the properties of matter at a more macroscopic level in instances such as the crust of a neutron star. This crust consists of layers of neutron-rich matter of increasing density. The nuclei become more neutron-rich by the process of electron capture. Neutron drip will occur at a density of about 4×10^{11} g/cm^3. At this point, the internal energy of the crust is released and it heats up. The timescale on which this happens depends on the rate of the electron capture and also the neutrino losses in the crust matter. A FRIB allows for the measurement of electron capture rates using charge exchange reactions on critical radioactive neutron-rich nuclei along dominant electron capture chains. Measurements of the Gamow-Teller strength distribution will also give information about the neutronization of the crust.

1.1.3. Fundamental Symmetries

Nuclear physics experiments have been successful in discovering fundamental symmetries in nature. The first violation of parity was observed from studies of ^{60}Co beta decays. These discoveries showed that physics is not the same if viewed in a mirror. Also, nuclear experiments gave way to the first direct detection of neutrinos and also the establishment of vector/axial-vector structure of weak interactions. There was also the establishment of a 2 eV/c^2 limit on the electron neutrino mass. These are all examples of the achievements of current radioactive

beam facilities. A facility such as a FRIB will allow for a wider range of isotopes to be used for studies of fundamental symmetries.

One symmetry that can be studied is CP, or charge-parity symmetry. A violation of CP symmetry is thought to be the cause of the dominance of matter over antimatter in the universe. It is proposed that an asymmetry between matter and antimatter developed as the universe cooled after the Big Bang. CP violation is consistent with the Standard Model but the level is much smaller than is necessary to account to the observed amount of matter in the universe. The best way to find a good source of CP violation is to look for a permanent electric dipole moment (EDM) in subatomic particles. There are several nuclei that have properties that enhance the effect of CP-violating interactions. The reason for this is that they have a static octupole deformation and closely spaced levels of opposite parity. This increases the mixing of quantum states due to the CP-odd nuclear forces. The calculations that have been done predict that the size of the EDM in these nuclei is expected to be several hundred to several thousand times larger than the most sensitive nucleus used now for EDM searches, ^{199}Hg. A FRIB will have the needed beam intensities to find an EDM.

1.1.4. Other Scientific Applications

There are several other science applications of a FRIB. These include stockpile stewardship, the medical and biologicial research applications of radionuclides,

materials science applications of radionuclides, and exotic beam applications to advanced reactor fuel cycles for transmutation of waste.

A FRIB would be useful in evaluating the status of the nuclear stockpile without any actual testing. The nuclear data needed to develop computational tools to model and evaluate the status could be gained from experiments performed at a FRIB. Currently, because of the extreme operating regimes of nuclear weapons, much of the information used to model the status is only theoretical. A rare isotope facility that is capable of creating isotopes at unprecedented rates could improve the models by getting experimental data such as the cross-sections of specific radioactive isotopes. Also the FRIB would be useful for the vast amount of information to be gained by the wide range of isotopes produced.

Medical applications of rare isotopes fall into three categories: imaging, targeted therapy, and radiotracers. All three categories need isotopes with very short lifetimes of less than one day. This is because the integrated dose to the patient should be as low as possible and hazardous waste should be minimal. To produce these isotopes, nuclear reactors or accelerators are needed. Reactors have the advantage of low cost, but the disadvantages are contamination of samples with multiple isotopes of the same element, resulting in less than desirable activity of the sample and limitations on the lifetimes of the isotopes when they are transported to the location of their use. Accelerators use charged particle reactions to produce the isotopes and there is the added benefit of in-flight separation to

produce a purer and more active sample. The disadvantages of using an accelerator are the high cost and low production rates. It should be noted that a FRIB would not produce enough samples for commercial medical use; however, it could produce enough to supply medical research studies.

In materials science applications rare isotopes have the function of being very high signal-to-noise in situ detectors of local atomic environments. By analyzing the decay products, usually gamma and beta decay, the angular and spectral content can indicate local field gradients and anisotropies in the material. Semiconductor research can exploit the characteristics of exotic isotope decays to detect low-density crystalline defects, impurities, and weak doping gradients. This helps in the development of high-performance semiconductors. Right now, the use of radioactive probes is limited by the fact that it is difficult to get a pure source of the needed isotopes. The in-flight separation that a FRIB offers could help to solve this problem.

The problem of long-lived radioactive waste may be dealt with by the accelerator transmutation of waste (ATW). ATW uses high-energy neutrons to burn or irradiate waste, causing the fission of the isotopes into more stable species. In order to do this more productively, the neutron cross-sections on unstable neutron-rich isotopes are needed in order to improve the design. This will determine the required levels of isotope separation and purity. Most of these cross-sections could be measured at a FRIB by direct neutron reactions. The great advantage of a

FRIB is the large volume production of the isotopes from which cross-section information may be extracted.

1.2. Introduction to FRIBs and Fragment Separators

In order to study exotic isotopes at an experimental level, there are three steps that must be taken 1.3. These include production, preparation, and observation. A FRIB must be able to function in order to perform each of these tasks effectively. There are two main approaches to studying rare isotopes. One is in-flight fragmentation and fission and the other is to study rare isotopes with reaccelerated beams. For the in-flight method, a high-energy, superconducting, heavy-ion driver linear accelerator is used to collide an intense, stable heavy-ion beam with a thin target. The resulting exotic beam is produced via projectile fragmentation and/or fission of the beam within the target. At this stage, a fragment separator is used to capture and separate the beam. The exotic nuclei are prepared by directing them onto an experimental target or stopping them in a gas cell. Reaccelerated beams can be used to study beams at lower energies for nuclear structure and astrophysics experiments. These beams are prepared in a couple of ways. The exotic beam can be taken from stopped beams in a gas cell and then subsequently reaccelerated to the required energies and directed onto an experimental target. Alternatively, they can be formed from the ISOL technique (Isotope Separation On-Line). This technique requires a high-energy proton driver to produce an intense proton beam that is directed onto a very thick target. The protons interact with nuclei of the

target material, producing exotic isotopes. These ions are then extracted from the target with electric fields and then accelerated to the desired energy and directed to a target. Among the methods described here, the experimenter must choose the best method that is appropriate for her experiment.

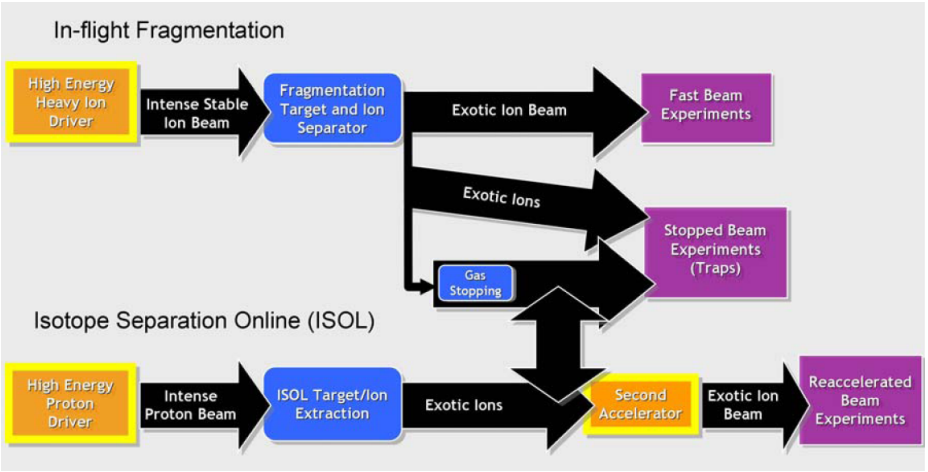

Figure 1.3. Techniques for producing and using rare isotope beams.

One key component of the process to obtain exotic beams for study and the subject of this thesis is the fragment separator. The role of the fragment separator is to separate an isotope of a desired mass and charge from all others produced in the production target. This machine uses electromagnetic fields to deflect or focus particles according to rigidity and by passing the beam through material to introduce a charge-dependent energy loss that can be exploited to purify the beam. This method will be elaborated on in the coming chapters, but first a survey of existing fragment separator facilities is presented.

In additon to the proposed FRIB in the U.S. [**2**], there are several other examples of rare isotope facilities around the world that are currently in stages from pre-conceptual design to commissioning. These include the NSCL at Michigan State University; RIBF at RIKEN, Japan [**3**]; the FAIR facililty at GSI, Germany [**4**]; the SPIRAL2 upgrade at GANIL, France [**5**]. Each of these facilities offers unique advantages to producing rare isotopes. Each of these facilites runs in a different energy regime, allowing for different reaction mechanisms and, therefore, a different range of rare isotopes. Low-energy reactions are more suitable for the study of fundamental nuclear structure studies, while higher energies are used to look at isotopes far from stability.

One of the proposed facilities for the FRIB is the Advanced Exotic Beam Laboratory (AEBL) at Argonne National Laboratory (Figure 1.4). The Argonne design would use a 400 kW, 200 MeV/u superconducting linear driver accelerator to accelerate beams up to ^{238}U. The driver concept would be coupled with the gas-stopping concept that was pioneered at Argonne. The existing ATLAS accelerator would be used to reaccelerate exotic beams for further experimentation. The benefits of having the facility at Argonne would be great as Argonne's nuclear physics program is world-leading and it also has great expertise in accelerator and target technology.

The proposed FRIB by MSU is shown below in Figure 1.5. The radioactive beam is accelerated by a superconducting RF driver linear accelerator that will provide 400 kW of power for all beams with uranium accelerated up to 200 MeV/u

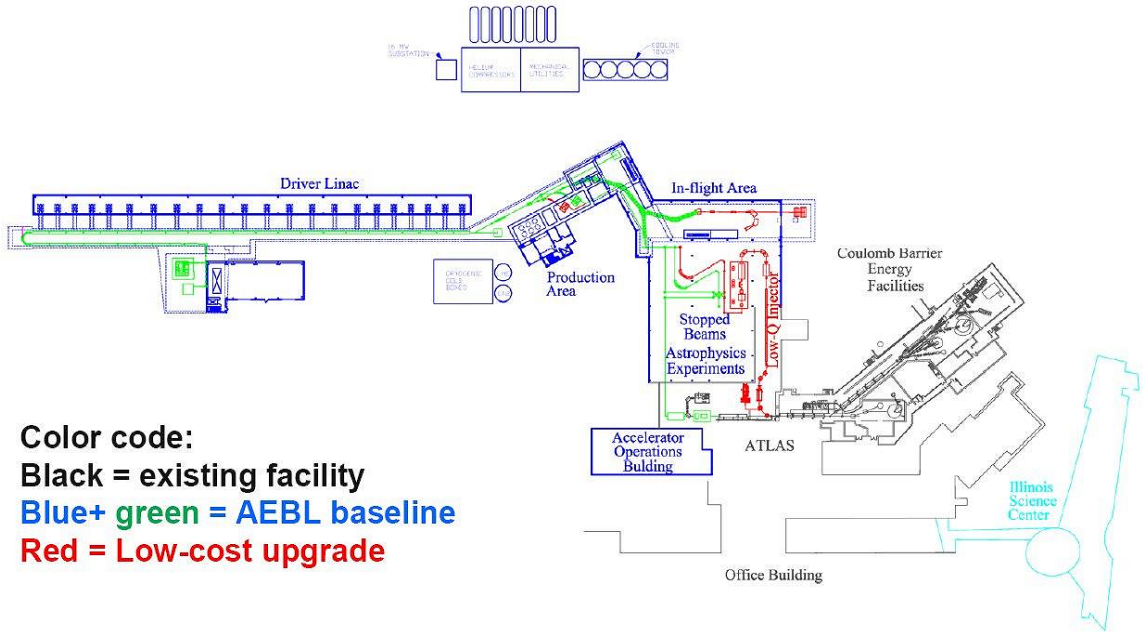

Figure 1.4. Proposed schematic for the Advanced Exotic Beam Laboratory (AEBL) at Argonne National Laboratory.

and lighter ions with increasing energy. Protons may be accelerated up to 600 MeV/u. There are two ECR ion sources that produce the primary beam. In this design there is space for the future addition of a third. There is also extra space in the linac tunnel and shielding in the production area for the future upgrade, up to an energy of 400 MeV/u for uranium. There is one in-flight production target. Included is the space and infrastructure to add up to two ISOL targets or an additional in-flight target with shielding. For reaccelerated beam experiments there is a superconducting RF reaccelerator for reaccelerated beams up to 12 MeV/u for uranium. The experimental areas include 47,000 sq ft for stopped, reaccelerated,

and fast beams. There are upgrade options to double the size of the experimental areas or to add a neutron scattering facility.

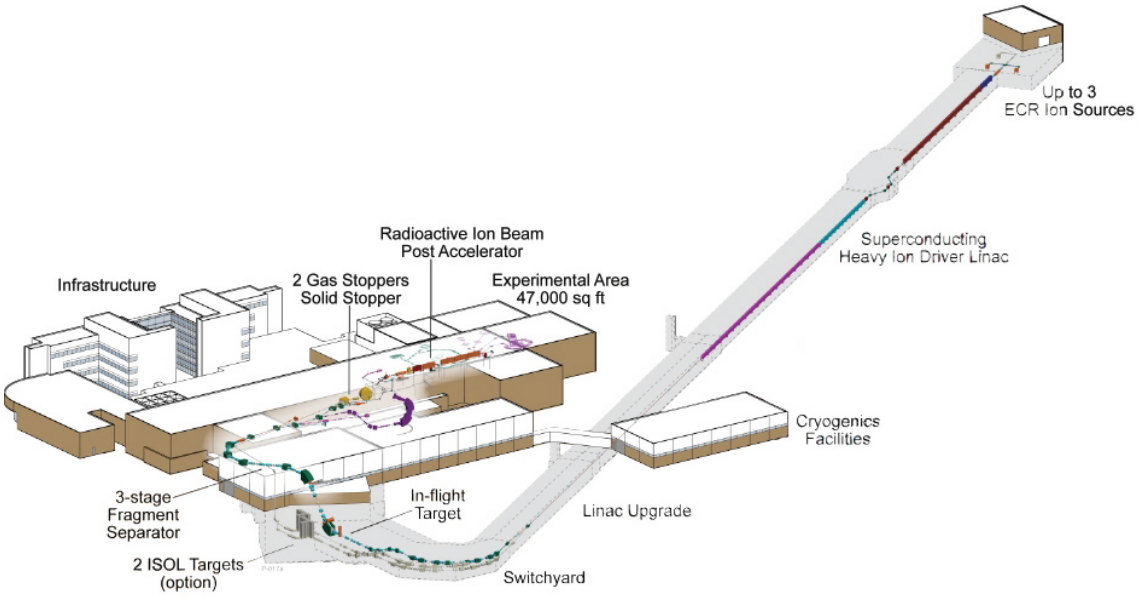

Figure 1.5. The current design of the FRIB that will be constructed at Michigan State University on the site of the National Superconducting Cyclotron Laboratory (NSCL).

The current fragment separator at the NSCL (National Superconducting Cyclotron Lab) at MSU is the A1900. It consists of iron-dominated superconducting magnets. It has four 45-degree dipoles and eight quadrupole triplets. The maximum rigidity the magnets can be set to is 6 Tm. The quadrupoles have a warm bore between 20 and 34 cm and the dipoles have a vertical gap of 9 cm. In order to correct higher order aberrations, sixteen of the quadrupoles have sextupole and octupole coils. The separator has a momentum acceptance of $\Delta p/p = 5\%$ and an

angular acceptance of $\Delta\Omega = 8\ msr$, making it one of the largest acceptance fragment separators in the world. The A1900 operates in an achromatic ion-optical mode with maximum dispersion at the intermediate image I2 (Figure 1.6). The dispersion is cancelled in the final focal plane FP [**6**].

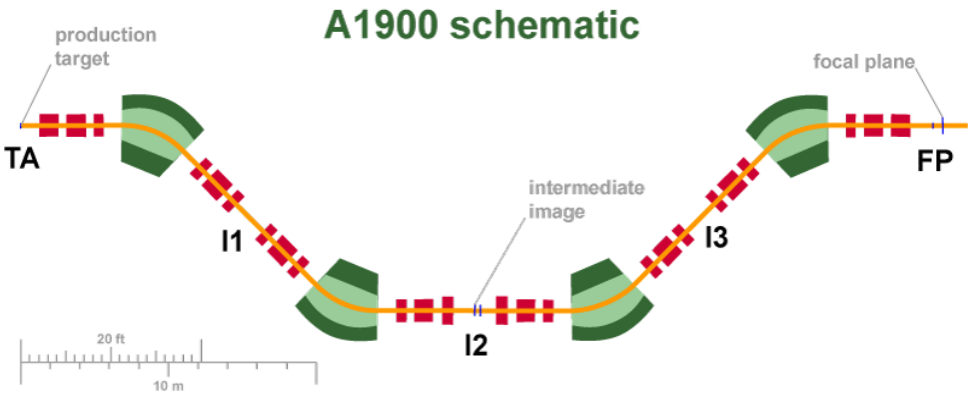

Figure 1.6. The A1900 is the current fragment separator at the NSCL at MSU. The schematic shows the focusing magnets (red) and the dipoles (greeen). Images are labelled I1, I2, I3. FP is the separation focal plane.

The RI Beam Factory (Figure 1.7) at RIKEN in Japan has a new high-power heavy-ion booster system that will consist of three ring cyclotrons that will boost the energies of the output beams to 440 MeV/u for light ions, and 350 MeV/u for very heavy-ions. The intensity of the beam is expected to be 1 pμA. The heavy-ion beams will be converted into intense rare isotope beams via projectile fragmentation or the in-flight fission of uranium ions by the isotope separator BigRIPS (Figure 1.8) [**7**]. BigRIPs has large angular and momentum acceptances. The angular acceptance is 80 mrad horizontally and 100 mrad vertically. The

momentum acceptance is 6%. The maximum rigidity that can be separated is 9 Tm. It is a long device (77 m). There are two separation stages possible. The first stage, from the production target to the focus F2, consists of four superconducting quadrupole triplets and two dipoles with a bending angle of 30 degrees and a mean bending radius of 6 m. These form a two-bend achromatic separator with an energy absorber placed at the momentum-dispersive focus F1. A high-power beam dump is placed inside the gap and exit of the first dipole D1. There are 7,000 tons of radiation shielding that surrounds the first stage. The first stage is followed by a telescopic system which transports the separated rare isotope beam to the second stage. The second stage is a four-bend achromatic spectrometer, which can be made into a second separation stage if another energy absorber is placed at the intermediate focus F5.

The Super FRS is the proposed upgrade to the current separator, FRS, at GSI in Germany. FAIR (Figure 1.9) is the proposed accelerator facility at GSI where the Super FRS (Figure 1.10) will reside. It is here where intense heavy-ion beams of 10^{12} particles/s will be produced at energies up to 1.5-2 GeV/u. The Super FRS will have a momentum acceptance of $\Delta p/p = 2.5\%$. The horizontal angular acceptance is $\Delta\phi_x = 40$ mrad and in the vertical is $\Delta\phi_y = 20$ mrad. The maximum rigidity the separator will be able to handle is 18 Tm. The Super FRS consists of a pre-separator and a main separator that each has an energy absorber. In terms of ion optics, there are six 28-degree dipole magnets with quadrupole

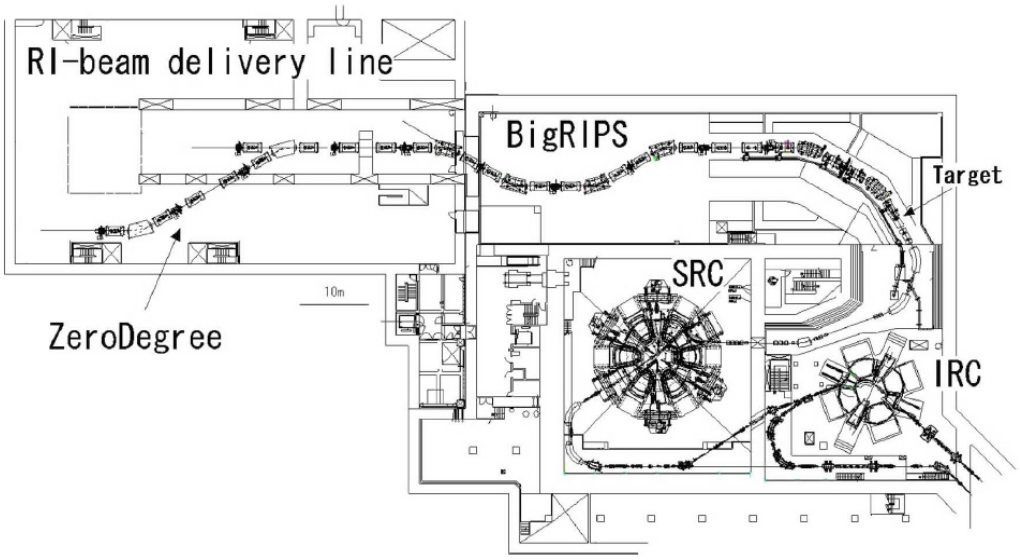

Figure 1.7. Schematic of the RI Beam Factory (RIBF) at the RIKEN facility in Japan.

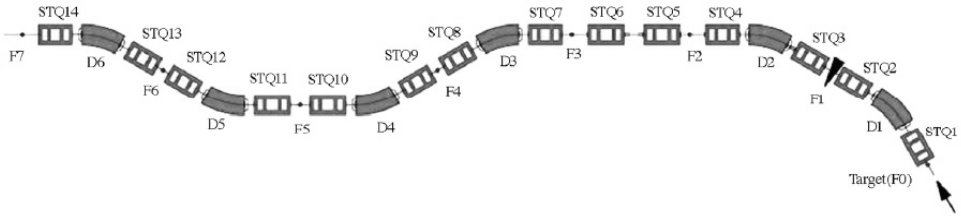

Figure 1.8. BigRIPS is the fragment separator located at the RI Beam Factory (RIBF) at RIKEN.

triplets on either side. Sextupole and octupole magnets are used to correct higher order aberrations.

The SPIRAL2 project is the upgrade to the current rare isotope facility at GANIL in France 1.11. The SPIRAL2 concept is to use a multi-beam driver to

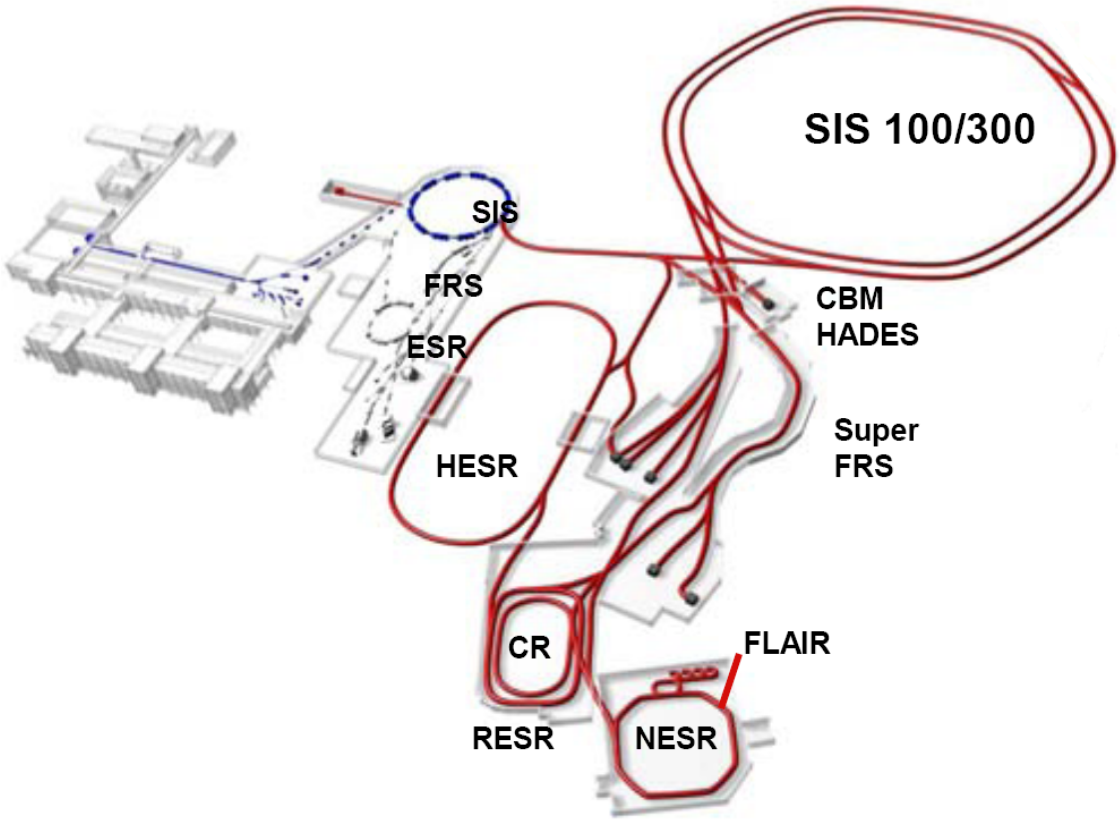

Figure 1.9. The proposed FAIR accelerator facility at GSI in Germany.

produce beams to be used for both ISOL and in-flight techniques. A superconducting linac with an acceleration potential of 40 MV will be able to accelerate 5 mA deuterons up to 40 MeV and 1 mA heavy-ions up to 14.5 MeV/u. The reactions available at this energy include fusion, fission, and fragmentation to produce exotic beams. One unique characteristic of the SPIRAL2 project is that it will be able to run five beams in parallel for multi-user experimentation.

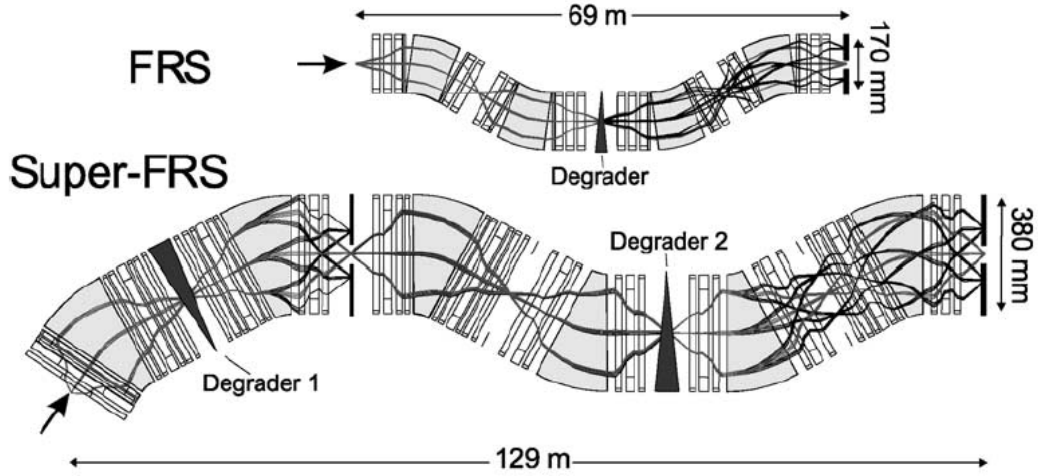

Figure 1.10. Schematics of the existing fragment separator FRS at GSI and the proposed upgrade SuperFRS.

LISE is the spectrometer at GANIL in France. This machine has a momentum acceptance of $\Delta p/p = 2.5\%$. The transverse emittance is limited to 16π mm mrad. LISE has low maximum magnetic rigidity, so there is an upgrade (LISE2000) that will add another branch to the fragment separator to allow rigidities up to 4.3 Tm.

1.3. Plans and Progress Towards a FRIB in the U.S.

In the late 1990's the nuclear structure and nuclear astrophysics communities joined together to propose a rare isotope accelerator that would produce unstable atomic beams at very large intensities. The joint NSF-DOE Nuclear Science Advisory Committee released a report in 1999 in support of RIA (Rare Isotope Accelerator). Based on the studies over the past decade, the U.S. Department of Energy Office of Science made a determination that a Facility for Rare Isotope

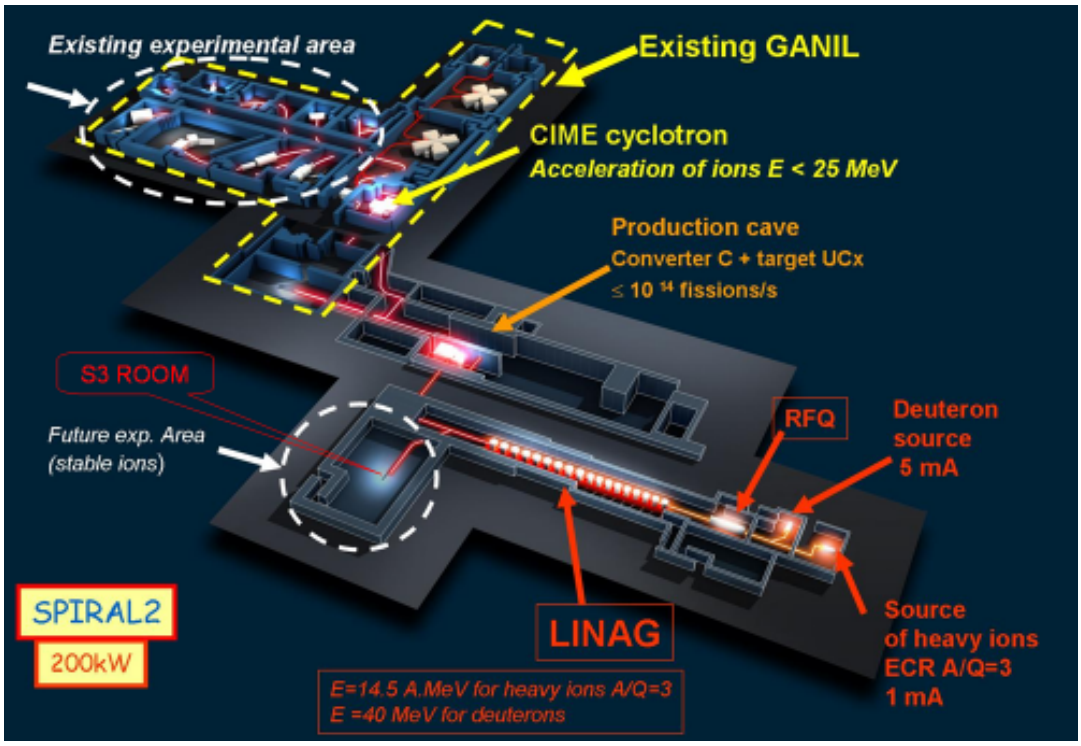

Figure 1.11. The proposed SPIRAL2 facility at GANIL. S^3 is the propsed mass separator.

Beams (FRIB) should be established. A high priority was placed on a FRIB and elaborated on in the DOE/National Science Foundation Nuclear Science Advisory Committee's 2007 Long Range Plan and the 2003 DOE report entitled "Facilities for the Future of Science: A Twenty-Year Outlook."

On May 20, 2008 a Funding Opportunity Announcement (FOA) was released to solicit applications for the design of FRIB. This was done to encourage competition between universities and national laboratories to produce the best possible facility. With applications due at the end of July 2008, a final decision on site

for a FRIB was made in December 2008. Two organizations submitted applications to receive the project. These facilities were University of Chicago/ Argonne National Laboratory LLC and Michigan State University. Michigan State University was ultimately chosen to receive the contract based on investigation by the Merit Review Panel. They came to this decision by evaluating the applications against Merit Review criteria stated in the FOA. Among these criteria were the scientific and technical merit of the project and consideration of the user community, the appropriateness of the proposed method or application, competency of the applicant personnel, and proposed resources, reasonableness, realism and appropriateness of the proposed budget. These criteria are imposed by federal regulation. The Department of Energy will provide funding up to $550 million over approximately 10 years to design and construct the facility. The funding will be subject to appropriations from Congress [**8, 9**].

1.4. Tools for Design, Optimization, and Simulation

There are many codes available that can be used to model fragment separators. These include the codes LISE++, and MOCADI, with the assistance of other codes such as MCNPX, MARS, and PHITS. These codes each have some strengths, but they also have major limitations. The code developed in this thesis with COSY INFINITY overcomes the limitations that the other codes possess.

The code LISE++ was designed by O. Tarasov and D. Bazin at MSU and has been in use by nuclear physicists for years to determine optimal parameters for

an exotic beam experiment with a fragment separator. This program is used to predict the intensity and purity of exotic beams with fragment separators. It can be used to tune experiments and the results can be used to compare to on-line data. Within the program, the fragment separator is specified by using "blocks." The "blocks" that are available as presets within the program are the current separators that exist around the world. These include the A1900 and S800 at the NSCL at MSU, LISE3 at GANIL, FRS and Super FRS at GSI, and BigRIPS and RIPS at RIKEN.

LISE++ [**10**] is able to model all aspects of the nuclear physics relevant for the fragment separator. These aspects include fragmentation, fisssion, and fusion-evaporation cross-sections, momentum and angular distributions of of fragments, energy loss in materials, and ionic charge state distributions. Some ion optics calculations are available. LISE++ was an upgrade to the previous code which included tools like the physical parameters calculator, database of nuclear properties, and relativistic two-body kinematics calculator. LISE++ includes these tools as well as some new tools. The "range optimizer" calculates the thickness and angle of an absorber used to slow down particles in order to stop them in a gas cell. The "Bρ/Eρ analyzer" will calculate and plot the trajectories of ions in the magnetic and/or electric dipoles depending on the energy and emittance of the beam and the settings of the dipole. The utility of this is to calculate the position of a primary beam trap in the dipole chamber to avoid scattering of a primary beam on the walls. The "evaporation calculator" is a tool that allows

one to visualize the dynamics of the de-excitation process in the case of the projectile fragmentation reactions using the fast analytical abrasion ablation model or fusion-residue reactions with the LisFus model.

Programs that calculate the charge states of fragments after passing through material are "Charge" and "Global." These have been added to LISE++. They can calculate atomic charge-changing cross-sections, charge state evolution, and equilibrium charge state distributions of heavy-ions penetrating matter. In the case of GLOBAL any energy can be used between 30 and 2000 MeV/u.

A new package within LISE++ has been developed to visualize the changes in the beam envelope along the separator. It is possible to plot the vertical and horizontal angular distributuions as well as the spatial distributions. Energy and momentum distributions are also available.

While there is integrated beam-material interactions and optics in the LISE++ code, the optics modeling is only to first order and there is no optical optimization allowed.

MOCADI [**11**] is a Monte Carlo code that is used to calculate the transport of the products of nuclear reactions such as fragmentation, fission, and fusion-evaporation. This can be done through optical systems such as a fragment separator. The ion-optical matrices of the fragment separator are computed by the program GICOSY which allows for high-order correction of aberrations. Energy loss in material is computed by ATIMA and cross-sections are calculated by the EPAX program for fragmentation products and PACE2 for fusion-evaporation products.

The charge state of the beam can be computed by the program CHARGE or GLOBAL. The main drawback of MOCADI for optimization of fragment separator experiments is that it is not an integrated approach. The ion optics must be computed separately from the Monte Carlo code which computes the dynamics of the beam in matter.

MCNPX (Monte Carlo N-Particle eXtended) [**12**] is the Los Alamos $3-D$, time-dependent Monte Carlo radiation transport code. The code has the ability to model the interactions of radiation with all particle types at all energies. It uses a combination of the latest nuclear cross-section data libraries, and where libraries are not available, physics models are used. For the transport of heavy charged particles, the Bethe-Bloch formalism has been enhanced to include values and interpolation procedures recommended in the ICRU Report 37 [**13**].

The MARS [**14**],[**15**] code is a set of Monte Carlo programs used for a detailed simulation of hadronic and electromagnetic cascades in an arbitrary three-dimensional geometry of shielding, accelerator, detector, and spacecraft components. It has a large energy range spanning from a fraction of an eV up to 100 TeV. It offers a fully theoretically consistent modeling of exclusive and inclusive distributions of secondary particles from spallation, fission, and fragmentation. It was developed beginning in 1974 at IHEP, SSCL, and Fermilab. The code combines the well-established theoretical models for strong, weak, and electromagnetic interactions of hadrons, heavy-ions, and leptons, including ionization energy loss calculated via the Bethe-Bloch method and multiple scattering. A system can

contain up to 105 objects ranging from microns to hundreds of kilometers. There are up to 100 composite materials with arbitrary three-dimensional magnetic and electric fields. There are powerful two- and three-dimensional graphical user interfaces for visualizing geometries, materials, fields, particle trajectories, and the results of the code. The MAD-MARS Beam Line Builder has been developed to build beam line and accelerator models in the MARS format by using a beam line description of the MAD accelerator design code. This has allowed for an extended set of supported element types which includes almost all of those supported by MAD as well as an arbitrary number of beam lines. There are more sophisticated algorithms and new data structures that enable more searches through the beam line geometry. Tunnel geometry can now be included in the code. Unfortunately, there is no optics optimization available within this code.

The PHITS (particle and heavy-ion transport) [**16**] code is one of the first general-purpose heavy-ion transport codes. It is a Monte Carlo code that is applicable at energies of several MeV/u to hundreds of GeV/u. There are many codes that are integrated to form PHITS. These include SPAR, JQMD, and NMTC/JAM. The heavy-ion transport method in PHITS proceeds as follows: Shen's formula is used to calculate the heavy-ion total reaction cross-section SPAR is used to calculate the stopping powers and ranges for muons, pions, protons, and heavy-ions at energies from zero to several hundreds of GeV. Then the JQMD (JAERI quantum molecular dynamics) code is used to analyze various aspects of

heavy-ion reactions as well as nucleon-induced reactions. It can be used to estimate the yields of emitted light particles, fragments, and of excited residual nuclei resulting from the heavy-ion collision. The secondary particles produced after a heavy-ion collision are transported by the NMTC/JAM code. This code is limited in that there are no optics integrated in the code (external electric or magnetic fields). Also, the codes PHITS and MARS are both single-event generators, which are very slow.

COSY INFINITY has the ability to model beam dynamics to arbitrary order. This is necessary to create a high-order fragment separator design. Optimizers within COSY are used to find the best quadrupole (first order), sextupole (second order) and octupole (third order) settings. COSY can model even higher order corrections, but for our situation it is sufficient to model the optics to third order. More details about COSY will be elaborated on in the coming chapters.

CHAPTER 2

Code Development

2.1. COSY INFINITY

2.1.1. Differential Algebra and Its Use Within COSY INFINITY

The particle optics code COSY INFINITY uses differential algebraic (DA) methods for the computation and manipulation of maps of arbitrary order for arbitrary field arrangements. The code is primarily used for the simulation, analysis, and design of particle optical systems. The first release of the code was in 1989 and the most recent edition is Version 9 [**17**], released in 2005. There are other codes that also use DA techniques that have been developed over the past fifteen years, but all are focused on high-energy accelerators. These include MXYZPTLK (FNAL), ZLIB (SLAC), DACYC (TRIUMF), TLIE (UMaryland), PTC (KEK), SIXTRACK (CERN), and UAL (BNL). COSY is unique in that it has special features that make it useful not only for high-energy accelerators but also for a FRIB fragment separator and other applications.

The diffential algebraic techniques involved in the computations at the heart of COSY INFINITY were developed in an attempt to solve analytic problems by algebraic means. The simplest nontrivial diffential algebra is found on $\mathbb{R}^2$. If we consider the set of all ordered pairs (q_0, q_1), where q_0 and q_1 are real numbers, then

scalar and vector multiplication are defined as:

$$(q_0, q_1) + (r_0, r_1) = (q_0 + r_0, q_1 + r_1) \tag{2.1}$$

$$t \cdot (q_0, q_1) = (t \cdot q_0, t \cdot q_1) \tag{2.2}$$

$$(q0, q1) \cdot (r0, r1) = (q0 \cdot r0, q0 \cdot r1 + q1 \cdot r0) \tag{2.3}$$

The ordered pairs, along with the previous operations, are called ${}_1D_1$. The element

$$d = (0, 1) \tag{2.4}$$

is known as the infinitesimal or differential. It is so small that its square vanishes. For any $(q_0, q_1) \in_1 D_1$,

$$(q_0, q_1) = (q_0, 0) + (0, q_1) = q_0 + d \cdot q_1. \tag{2.5}$$

The first component of (q_0, q_1) is termed the real part and the second component is the differential part. The derivation of ${}_1D_1$ is represented by a map ∂ from ${}_1D_1$ into itself and will turn the algebra ${}_1D_1$ into a differential algebra. Define $\partial : {}_1D_1 \longmapsto {}_1D_1$ as:

$$\partial(q_0, q_1) = (0, q_1). \tag{2.6}$$

It should be noted that

$$\partial\{(q_0, q_1) + (r_0, r_1)\} = \partial(q_0 + r_0, q_1 + r_1) = (0, q_1 + r_1) \tag{2.7}$$

$$= (0, q_1) + (0, r_1) = \partial(q_0, q_1) + \partial(r_0, r_1) \tag{2.8}$$

and

$$\partial\{(q_0, q_1) \cdot (r_0, r_1)\} = \partial(q_0 \cdot r_0, q_0 \cdot r_1 + q_1 \cdot r_0) = (0, q_0 \cdot r_1 + q_1 \cdot r_0) \tag{2.9}$$

$$= (0, q_1) \cdot (r_0, r_1) + (q_0, q_1) \cdot (0, r_1) \tag{2.10}$$

$$= \{\partial(q_0, q_1)\} \cdot (r_0, r_1) + (q_0, q_1) \cdot \{\partial(r_0, r_1)\} \tag{2.11}$$

This holds for all $(q_0, q_1), (r_0, r_1) \in_1 D_1$. Therefore, ∂ is a derivation and hence $({}_1D_1, \partial)$ is a differential algebra. In beam physics, ${}_1D_1$ can be used for the automated computation of derivatives.

Assume that we have the values and derivatives of two functions f and g at the origin. These are put into real and differential components of two vectors in ${}_1D_1$ that have the form $(f(0), f'(0))$ and $(g(0), g'(0))$. Let's assume that we need the derivative of the product $f \cdot g$, which is given by $f'(0) \cdot g(0) + f(0) \cdot g'(0)$. This is the second component of the product $(f(0), f'(0)) \cdot (g(0), g'(0))$, where the first component of the product is $f(0) \cdot g(0)$. Therefore, if two vectors contain the values and derivatives of two functions, then their product contains the values and derivatives of the product function.

The operation [] is defined from the space of differentiable functions to ${}_1D_1$ from

$$[f] = (f(0), f'(0). \tag{2.12}$$

From this we have

$$[f + g] = [f] + [g], \tag{2.13}$$

and

$$[f \cdot g] = [f] \cdot [g]. \tag{2.14}$$

All intrinsic functions typically found on computers are representable by a finite number of additions and multiplications. Any function f representable by finitely many additions, subtractions, multiplications, divisions, and intrinsic functions on ${}_1D_1$ satisfy the relationship

$$[f(x)] = f([x]). \tag{2.15}$$

For all $r \in \mathbb{R} \subset_1 D_1$,

$$(f(r), f'(r)) = f(r + d), \tag{2.16}$$

where $f(r)$ and $f'(r)$ are equal to the real and differentiable parts of $f(r+d)$. Equation 2.16 can be rewritten as

$$f(r+d) = f(r) + d \cdot f'(r). \tag{2.17}$$

Hence, to obtain the derivative of a function to machine precision all is needed is the evaluation of the function in DA. This example for scalar functions of one variable and first-order derivatives can be extended to vector functions of several variables and arbitrary high-order derivatives. This is implemented in COSY as the ${}_nD_v$ structure. A more thorough analysis of DA methods may be found in [**18**].

The transfer map methods involved in the DA computations are represented by the transfer map $\mathcal{M}$, which is the flow of the system ODE and is given by

$$\overrightarrow{z}_f = \mathcal{M}(\overrightarrow{z}_i, \overrightarrow{\delta}), \tag{2.18}$$

where $\overrightarrow{z}_i$ and $\overrightarrow{z}_f$ are the initial and final conditions, and $\overrightarrow{\delta}$ is system parameters.

Each element in the fragment separator has an effect on the dynamics of the beam. In order to figure out what the coordinates of the particles in the beam are at any point, the maps of the fragment separator components may be composed with each other and with a vector representing the coordinates of the beam. The final coordinates of a particle in the beam, $\vec{z}_f$ may be expressed as $\vec{z}_f = \mathcal{M}(\vec{z}_i)$,

where $\mathcal{M}$ is the map of the fragment separator and $\vec{z} = (x, a, y, b, l, \delta)$ is a vector with six components being the canonically conjugate phase space variables. These coordinates are defined as follows:

(2.19) x = position in meters,

(2.20) y = position in meters,

(2.21) a = $\frac{p_x}{p_0}$ momentum in x-direction divided by momentum of reference particle,

(2.22) b = $\frac{p_y}{p_0}$ momentum in y-direction divided by momentum of reference particle,

l = $-\frac{(t - t_0)v_0\gamma_0}{(1 + \gamma_0)}$ time-of-flight-like coordinate with v_0 equal to velocity of reference particle,

(2.23) δ = $\frac{(K - K_0)}{K_0}$ relative kinetic energy deviation from reference particle.

To first order, the map is just a matrix. However, at higher orders, the map is represented by nonlinear terms. The Taylor expansion for the map is given by

$$z_{m,f} = \sum_{j=1} z_{j,i}\{(z_{m,f}|z_j) + \frac{1}{2}\sum_{k=1} z_{k,i}\{(z_{m,f}|z_j z_k)$$

$$+\frac{1}{3!}\sum_{l=1} z_{l,i}\{(z_{m,f}|z_j z_k z_l) + ...\}\}. \tag{2.24}$$

The first-order coefficients, $(z_{m,f}|z_j)$, are the elements of the linear transfer matrix. All of the coefficients of the higher order terms, $(z_{m,f}|z_j z_k)$ and $(z_{m,f}|z_j z_k z_l)$, are termed "aberration coefficients." These coefficients multiplied by the initial coordinates are termed "aberrations." These terms may be computed to arbitrary order. In our studies, these coefficients of the Taylor expansion are found internally by COSY.

The DA method allows for very efficient computation of high-order Taylor transfer maps, and the normal form method [**19**] can be used for analysis of nonlinear behavior since it works to arbitrary order. In addition, it can keep system parameters in maps. The algorithms are transparent and effort is independent of computation order, although memory requirements are order-dependent. COSY has many built-in DA tools and algorithms necessary for the simulation of optical systems.

2.1.2. A Description of the Capabilities of COSY INFINITY

COSY INFINITY can evaluate transfer maps of systems to arbitrary order. There are no approximations to the particle motion or field description of the magnetic or electric elements. There is a large collection of elements that can be called from within COSY. The input language is very flexible as it uses its own programming language, which is object oriented.

There are many elements that make up COSY. The DA package comprises 27,500 lines of code, while the compiler/executer for the COSY language is 6,500 lines. Optimizers make up about 2,000 lines and graphical interfaces are about 2,800. Altogether there are about 38,800 lines of standard FORTRAN77/90 compilation/execution in one step without any linking. Incremental compilation is possible. Physics routines are located in COSY.FOX and are compiled only once. The user file DEMO.FOX has examples for many of the features in COSY.FOX. There are F90 and C++ interface packages and validated computation packages. COSY-VI is the validated integration package and COSY-GO is the validated global optimization package. The reference and programming manuals for COSY are available online [**20**].

COSY INFINITY will run on a variety of environments. These include Linux and Standard UNIX, Microsoft Windows PC, VAX VMS, HP, IBM Mainframes, and CRAY. Many graphic output options are available and include PGPLOT, Direct PostScript, LATEX picture mode, GKS, graPHIGS, Direct Tektronix, and low-resolution ASCII.

The COSY code is based on standard FORTRAN77. The code uses its own programming language, which is object oriented, and is often compared to PASCAL. A COSY user only needs to to know the COSY programming language in order to run the code. The user is free from any FORTRAN programming. The syntax of the code is simple, allowing for calls to optical elements. The types of elements available in COSY are listed in Table 2.1. These elements may

Table 2.1. Listing of the various elements available in COSY INFINITY.

Elements in COSY
Magnetic and electric multipoles/fringe fields
Superimposed multipoles/fringe fields
Combined function bending magnets with curved edges/fringe fields
Electrostatic deflectors/fringe fields
Wien filters/fringe fields
Wigglers/fringe fields
Solenoids with various confingurations/fringe fields
3-tube electrostatic round lens with various configurations/fringe fields
Fast fringe fields (SYSCA)
General electromagnetic elements with measured data
Glass lenses, mirrors, prisms with arbitrary surfaces
Misalignments: position, angle, rotation

be called arbitrarily for any number of particle beam optics applications. Some common applications of the COSY elements include the interactive design of spectrometers, interactive design of accelerator lattices, high-order analyses including optical aberrations, fringe field analysis, measured fields, error analysis, parameter dependences, closed-orbit and lattice parameters, and normal form resonant and non-resonant resonance driving terms.

Among the special features of COSY are the analysis of spin motion and computation of fringe fields. Fringe fields may be computed in a variety of ways in COSY. Measured field data may be used as long as it is supplied as points on an equidistant grid in Cartesian coordinates. The evaluation of the field strength is then done by Gaussian interpolation [**21**]. Another way to calculate the fringe fields in COSY is by the SYSCA fast fringe field method. This method is based on a combination of geometric scaling in TRANSPORT coordinates and symplectic

rigidity scaling. This method uses parameter-dependent symplectic representations of fringe field maps that are stored on files to approximate the fringe field using symplectic scaling. The time for executing this procedure is two to three orders of magnitude less than if one were to directly integrate the fields.

2.1.3. Things Missing in COSY That Are Needed

While COSY's powerful DA methods are necessary for an accurate simulation of fragment separator beam dynamics, there are a few things that are lacking in the model. The master version of COSY did not have the ability to take into account beam-material interactions, which is necessary for heavy-ion fragmentation and fission. In order to track heavy-ions of different masses and charges through the fragment separator and to look at how these different particles interact with materials such as the target and absorber wedge, much code development was needed.

While the map representation of the target and absorber wedge exist in the current master version of COSY, they needed to be extended to include the most recent energy loss functions based on the ATIMA procedure, which uses spline interpolations rather than the existing Bethe-Bloch function for energy loss.

For fragmentation and fission, a Monte Carlo code needed to be developed to track the interactions of the heavy-ions within the target or absorber material. Auxiliary codes had to be implemented in order to determine how many and what type of particles are produced from a fragmentation or fission of an isotope of a

given nuclear mass A and nuclear charge Z given a target of a specified A and Z. For fragmentation reactions, a cross-section is needed that is based on the A and Z of the parent particle, child particle, and target material. The calculation for the cross-section of a fission reaction requires the values of all of these including the energy of the primary beam.

2.2. Auxiliary Codes Implemented in COSY

There were four auxiliary codes implemented in COSY for the simulation of beam-material interactions [**22**]. These include EPAX for returning the cross-section of isotopes produced by nuclear fragmentation and MCNPX for the cross-sections of isotopes produced by the fission and fragmentation of a ^{238}U beam. MCNPX is also used to determine the particle dynamics in the ^{238}U case. ATIMA was used to calculate energy loss, and energy and angular straggling. GLOBAL is used to determine the charge states of all particles as they pass through matter.

2.2.1. EPAX

EPAX [**23**] is a code that was proposed in 1990 by Summerer et al. to provide a universal empirical parameterization of fragmentation cross-sections. Originally, since there was little heavy-ion-induced experimental data available, this parameterization was based on multi-GeV proton-induced spallation cross-sections. Recently, the parameterization has changed with new experimental data from the projectile fragmentation of heavy nuclei such as ^{197}Au and ^{208}Pb on H_2 targets.

This has allowed for a more stringent comparison between proton- and heavy-ion-induced isotope distributions. By this comparison, it is indicated that for heavy nuclei the two reactions lead to different isotopic distributions, that cannot be obtained from each other by just scale factors. This is because the heavy-ion-induced reactions deposit more excitation energy in a nucleus than do the proton-induced reactions. This makes the product distribution broader and more neutron-deficient. In both cases, however, it is possible to describe the isotopic yield distributions by Gaussian-like analytical functions with parameters that vary smoothly as a function of the fragment mass.

The characteristics of the EPAX formula are elaborated on in [**23**]. However, the result of these characteristics yields the following formula to describe the cross-section σ of an isotope with atomic mass A and nuclear charge Z:

$$\sigma(A,Z) = Y_A \sigma(Z_{prob} - Z) = Y_A \exp(-R\,|Z_{prob} - Z|^{U_{n(p)}}), \tag{2.25}$$

where Y_A represents the mass yield, which is the sum of the isobaric cross-sections with fragment mass A. The second term, $\sigma(Z_{prob} - Z)$, describes the charge dispersion, which is the distribution of elemental cross-sections with a given mass around its maximum, Z_{prob}. The shape of the charge dispersion is controlled by the width parameter R and the exponent U_n for neutron-rich side or U_p for proton-rich

side. The factor $n = \sqrt{\frac{R}{\pi}}$ exists to normalize the integral of the charge dispersion to unity.

2.2.2. GLOBAL

The code GLOBAL [**24**] for charge state calculations uses the Runge-Kutta method to numerically solve the equation

$$\frac{dY_n(x)}{dx} = \sum_{n' \neq n} \sigma(n', n) Y_{n'}(x) - \sigma_{tot}(n) Y_n(x), \tag{2.26}$$

where $Y_n(x)$ is the yield of projectile ions in state n. Here x is the penetration depth in $atoms/cm^2$ in the target, $\sigma(n', n)$ is the cross-section in cm^2 for a transition from projectile state n to n', and $\sigma_{tot}(n) = \sum_{n' \neq n} \sigma(n, n')$ is the total charge-changing cross-section for an ion with n initially attached electrons. The aim is to parameterize the cross-sections $\sigma(n', n)$ so that they are useful over a wide range of applicability. In order to obtain the $\sigma(n', n)$'s, the cross-sections for electron loss and capture must be known. Electron loss is given by

$$\sigma(n, n-1) = n_K \sigma_K^l + n_L \sigma_L^l + n_M \sigma_M^l, \tag{2.27}$$

where n_K, n_L, n_M are the number of electrons and $\sigma^l_K, \sigma^l_L, \sigma^l_M$ are the cross-sections of the K, L, and M shells, respectively. Similarly, the cross-section for electron capture is given by:

$$\sigma(n, n+1) = \frac{2 - n_K}{2}\sigma^c_K + \frac{8 - n_L}{8}\sigma^c_L + \frac{18 - n_M}{18}\sigma^c_M. \tag{2.28}$$

Screening and excited-state effects are taken into account and are described in detail in [**24**]. By using fitted range-energy relations, GLOBAL can determine the projectile energy at any depth in the target so that the ionization and capture cross-sections can be adjusted to the projectile energy at the collision point.

2.2.3. ATIMA

The program ATIMA [**25**] was developed at GSI to calculate various physical quantities which describe the slowing down of protons and heavy-ions in matter for kinetic energies ranging from 1 keV/u to 450 GeV/u. These quantities include the stopping power, energy loss, energy loss straggling, angular straggling, range, range straggling, and other beam parameters such as the magnetic rigidity, time of flight, and velocity.

The physics of the program is based on the theory of Lindhard and Soerensen (LS) for energies above 30 MeV/u. This theory includes shell correction, a Barkas term, and the Fermi-density effect. Below 10 MeV/u, an older version of Ziegler's

SRIM program is used. In the energy regime between 10 MeV/u and 30 MeV/u an interpolation between the two theories is used. The energy loss straggling comes from the LS theory above 30 MeV/u, and below 10 MeV/u the theory of Firsov and Hvelplund is used.

2.2.4. MCNPX

MCNPX has been upgraded to include the reactions and transport of energetic heavy-ions such as ^{238}U. These calculations are necessary in order to accurately model the dynamics of beams used in projects such as a FRIB. The original MCNPX was the result of the merger of the two codes MCNP and LAHET. Previously, LAHET was used to produce and transport 34 particle types using the physics model ISABEL. With the latest code MCNPX 2.5.0, released in April 2005, the number of allowed isotopes for transport and interaction is 2200 with the incorporation of the LAQGSM physics model. These isotopes range from ^{5}He to ^{259}Fm and are clustered around the line of stability in the Table of Isotopes [**26**].

2.3. COSY Extensions for Fragmentation and Fission

It was necessary to treat fragmentation and fission separately due to the codes that are currently available to model such phenomena. For beams where fragmentation is the only production mechanism, traditional methods are good enough for

predicting cross-sections and dynamics of the beam. However, for fission, cross-sections are not given by the same methods, and the dynamics of the beam are more complicated. The individual treatments of fragmentation and fission are the topic of this section.

2.3.1. Fragmentation

2.3.1.1. Cross-sections for Fragmentation Case. In the case of any primary beam below ^{238}U, the cross-sections of the secondary particles produced via fragmentation of the beam are found by the procedure EPAX. The parameters that are input into this procedure are the nuclear mass and charge of the primary beam and the nuclear mass and charge of the product. Also, it is necessary that the target's nuclear mass, nuclear charge, and thickness are input. The cross-section in millibarns is returned.

2.3.1.2. Kinematics for Fragmentation Case. The secondary particles that emerge from the target have different kinematics depending on the production mechanism by which they were formed. For nuclear fragmentation, the angular divergence and momentum deviation of the secondary particle will be solely based on its mass and on the initial mass of the nucleus that fragments. This is called the "Fireball" method, where the momentum is given by a Gaussian distribution with the standard deviation given by

$$\sigma = \frac{85}{c_{light}} \sqrt{\frac{A_c(A_p - A_c)}{A_p - 1}}, \tag{2.29}$$

where A_p is the nuclear mass of the parent and A_c is the nuclear mass of of the child particle. The momentum of the new fragment is modified by adding a random number chosen from the Gaussian distribution with standard deviation σ. Then the perpendicular and parallel components are found. The parallel component will be used to calculate energy loss and straggling, and the perpendicular component will be used to calculate the angular divergences and angular straggling.

2.3.2. Fission

2.3.2.1. Cross-sections for Fission Case. In contrast to the fragmentation process, the cross-section of a fission product is energy dependent. MCNPX was used in order to find the cross-section of all the isotopes produced by a ^{238}U beam. Due to time considerations, MCNPX could only be run for a few particular cases, i.e., ^{238}U beam energies, target material. The cases chosen were based on the energy regimes of existing fragment separators which range from about 100 MeV/u to 1500 MeV/u. The proposed FRIB's fragment separator would have a maximum energy of 200 MeV/u for a ^{238}U beam. There were eight particular cases that were run to give the cross-sections and dynamics for four different ^{238}U beam energies (200, 400, 800, and 1500 MeV/u) incident on both C and Li target

materials. For the simulations, the uranium beam was assumed to be point-like with no angular divergence or energy spread. Both C and Li targets each had a thickness of 0.1068 g/cm^2. The output from MCNPX is the number of particles of each isotope produced N_{prod}. This number includes all the isotopes produced by all nuclear processes. With this number, the cross-section of the isotope may be computed by the formula

$$\sigma_{cs} = \frac{N_{prod}\ A}{N_0 x \rho N_A}, \tag{2.30}$$

where A is the nuclear mass of the target, N_0 is the number of source ^{238}U particles, x is the target thickness, ρ is the target density, and N_A is Avogadro's number. The number of source ^{238}U particles used in each run was between 6×10^8 and 1×10^9. The cross-sections of all the isotopes resulting from the 200, 400, and 1500 MeV/u cases are shown in Figures 2.1 and 2.2.

The output from MCNPX was limited in that it did not provide cross-section data for isotopes that are either neutron-deficient (near the proton drip line) or neutron-rich (near the neutron drip line). This is due to the fact that the target thickness used in the run was small and the number of source particles was not large enough to produce any particles of the rare isotopes in this regime. Because of this fact it was necessary to interpolate the cross-sections for these isotopes near the drip lines for which a cross-section did not exist. This was accomplished by

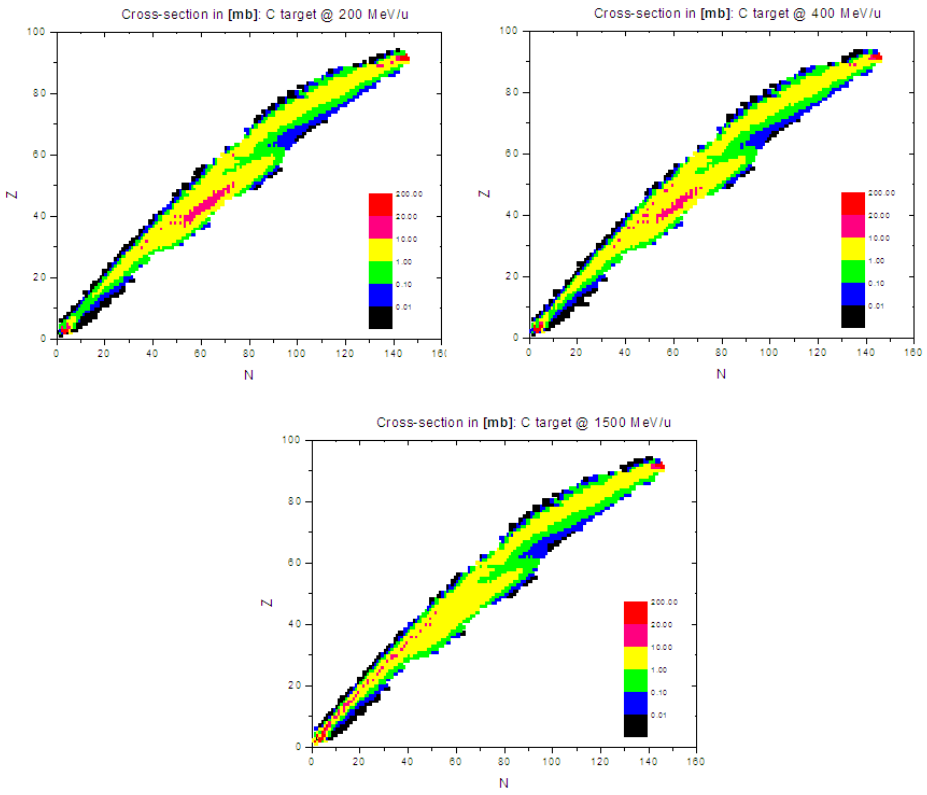

Figure 2.1. Cross-sections for all isotopes in mb for a ^{238}U beam incident on a 0.1068 g/cm^2 C target.

fitting the cross-sections of the last two maximum and two minimum isotopes, for constant Z, on the neutron-rich and -deficient sides of the Chart of the Nuclides to an exponential function. This exponential takes the form

$$\sigma_{cs} = Ke^{-N}, \tag{2.31}$$

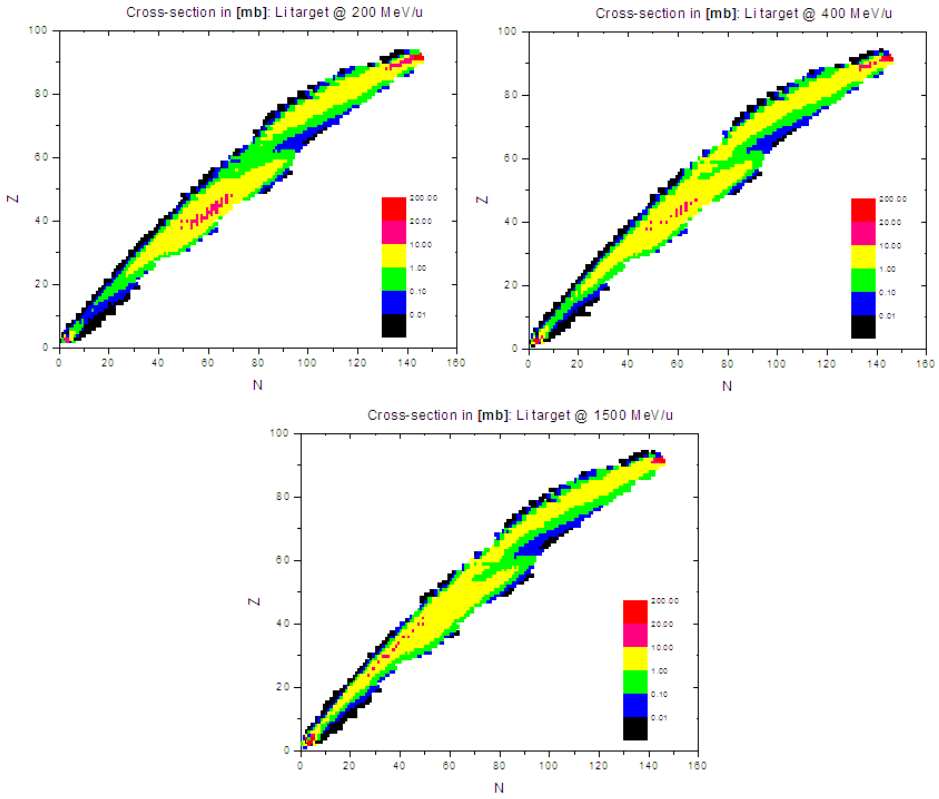

Figure 2.2. Cross-sections for all isotopes in mb for a ^{238}U beam incident on a 0.1068 g/cm^2 Li target.

where K is a multiplicative constant and N is the number of neutrons for neutron-rich isotopes, and

$$\sigma_{cs} = K(e^{-N} - 1), \tag{2.32}$$

for neutron-deficient isotopes.

The cross-section data provided by MCNPX were used to interpolate the cross-section of the fission products as a second-order polynomial in energy given by

$$\sigma_{cs} = c_0 + c_1 E + c_2 E^2, \tag{2.33}$$

where E is the energy of the ^{238}U beam and the c_n's are the coefficients of the interpolation for a given isotope with nuclear mass A and nuclear charge Z. The coefficients of this polynomial are listed in a file that is read in once by COSY and stored in an array each time the code is run. This method is very fast and uses very little memory.

2.3.2.2. Kinematics for Fission Case. For fission, the coordinates are not only based on the masses of the nuclei as is the case for fragmentation. There is an extra energy release that results from the fissioning nucleus. This extra energy release means that the products will have a large δ, or energy spread, and also large angular divergences. If δ and the angular coordinates of the products are plotted, then the result is a "fuzzy" spherical shell that represents the phase space that is occupied by fission products. The spheres shown in Figures 2.3 and 2.4 are for ^{132}Sn particles produced by a ^{238}U beam at different energies incident on C and Li targets.

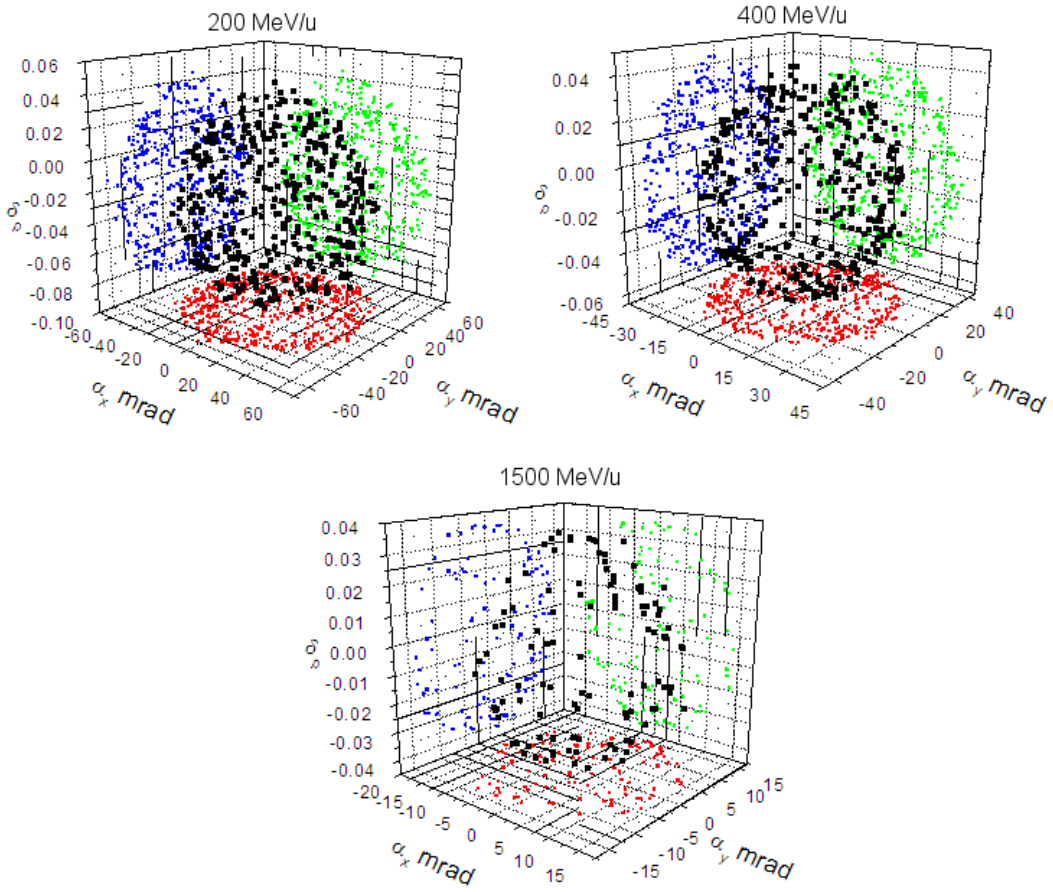

Figure 2.3. Coordinates of a ^{132}Sn beam produced by a ^{238}U beam at 200, 400, and 1500 MeV/u incident on a C target. Black dots are the actual coordinates, while the colored dots are the projections onto the planes. δ_p is the momentum deviation and α_x and α_y are the horizontal and vertical angular divergences, respectively.

The fact that all fission products are emitted from the target in a sphere like the one described can be used to model the dynamics. More precisely, the coordinates of these fission products are best represented by a spherical shell with some thickness. In order to get the initial conditions of each isotope that will pass

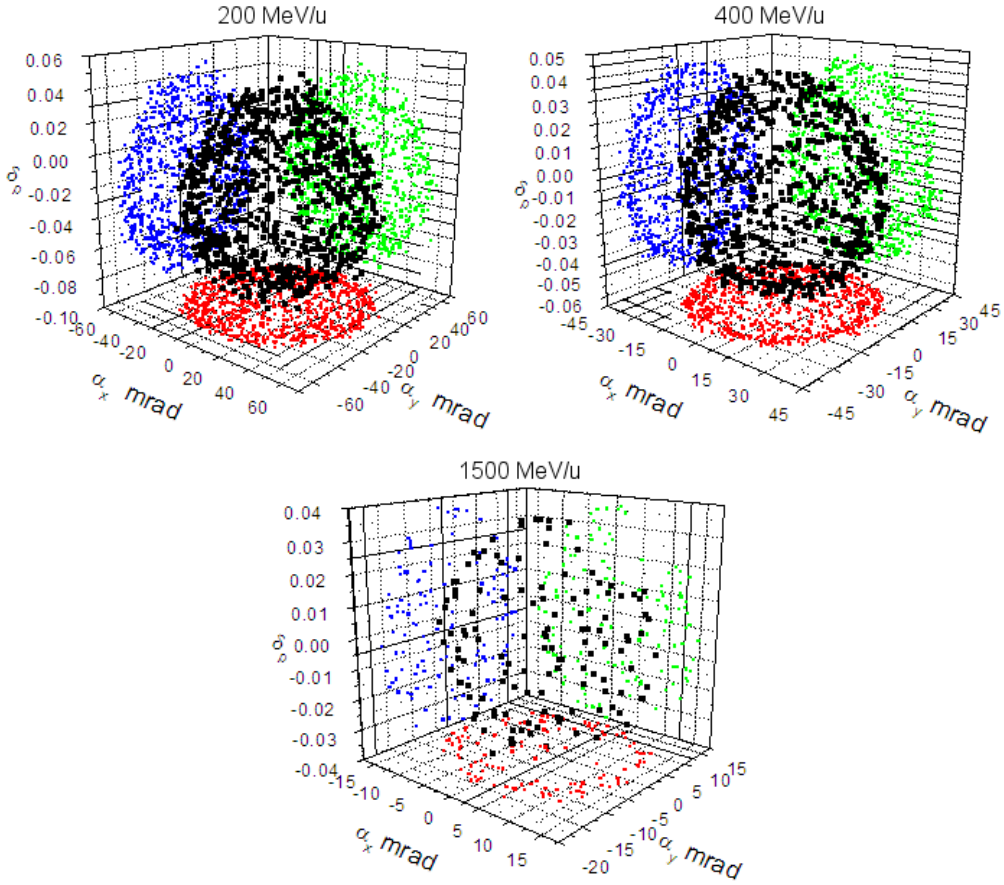

Figure 2.4. Coordinates of a ^{132}Sn beam produced by a ^{238}U beam at 200, 400, and 1500 MeV/u incident on a Li target. Black dots are the actual coordinates, while the colored dots are the projections onto the planes. δ_p is the momentum deviation and α_x and α_y are the horizontal and vertical angular divergences, respectively.

through the fragment separator, we must have a method to obtain the "sphere" of each isotope in a random manner. The first step in obtaining the sphere is to normalize the coordinates of the fuzzy spherical shell to unity. After this normalization is complete, each particle is represented by the value of its radius in

the sphere. Figures 2.5 and 2.6 are histograms that represent how many ^{132}Sn particles are located at each radius for different energy and target material combinations. From these histograms, it is noted that with low energy, the thickness of the spherical shell is large, with the most particle density at larger radii. As the energy increases, the thickness of the spherical shell becomes thinner and more dense and, hence, represents a lower beam emittance.

Using this representative "phase space unit sphere" we can uniformly choose the new coordinates of the ^{238}U products based on the output of MCNPX. To obtain the coordinates in a random fashion on the unit sphere, we first uniformly pick a δ from -1 to 1. Next, we introduce the angle ϕ, in the a, b plane. If we uniformly pick a ϕ that is between 0 and 2π, then this gives the a, b, and δ coordinates:

$$a = r\cos\phi, \tag{2.34}$$

$$b = r\sin\phi, \tag{2.35}$$

$$\delta = \sqrt{1-r^2}, \tag{2.36}$$

where $r = \sqrt{1-\delta^2}$. The coordinates on the unit sphere must be transformed to an ellipsoid that corresponds to the distribution of each isotope in real space. This is done by picking a random number based on standard deviation and mean of each isotope's distribution, assuming it is Gaussian. This number $R_{A,Z}$ is a random

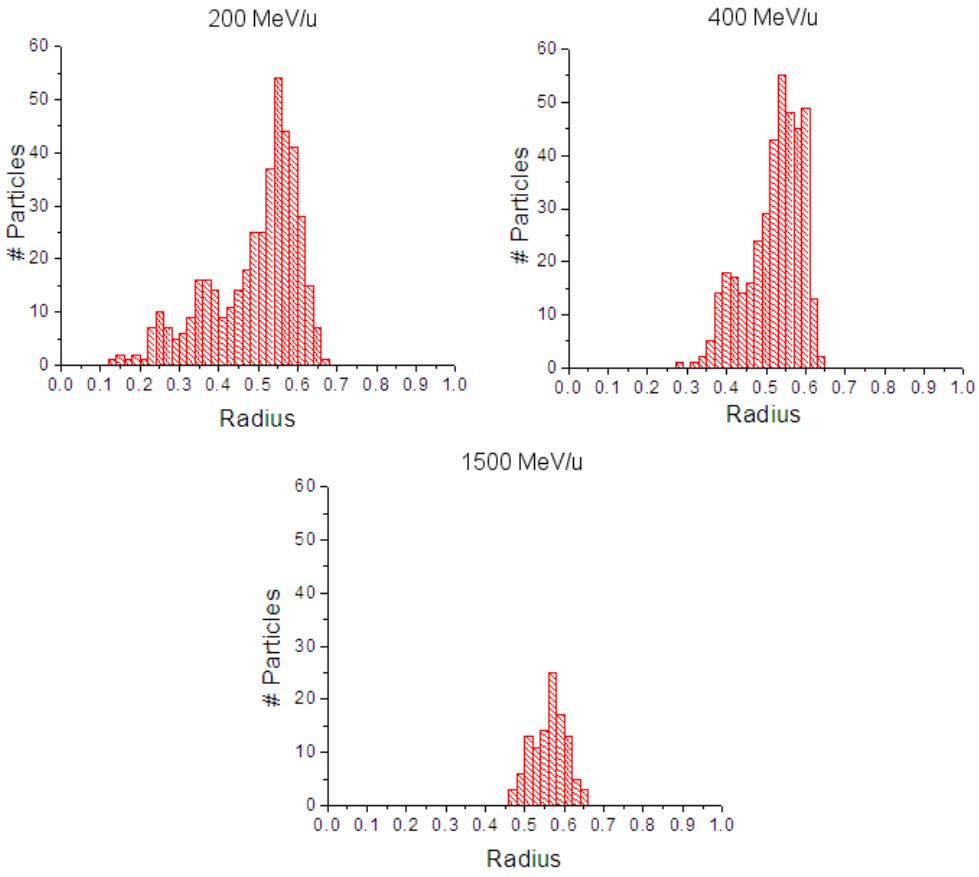

Figure 2.5. Histograms that represent the number of ^{132}Sn particles that have various radii after normalization to a unit sphere (C Target). The cases are for a ^{238}U beam with energies of 200, 400, and 1500 MeV/u incident on a C target.

number that is used to select the "fuzziness" of the sphere. This number must be multiplied by the maximum values of a, b, δ predicted from the interpolations to transform the sphere to the phase space ellipsoid. The final coordinates of the particle with nuclear mass A and Z after this transformation are

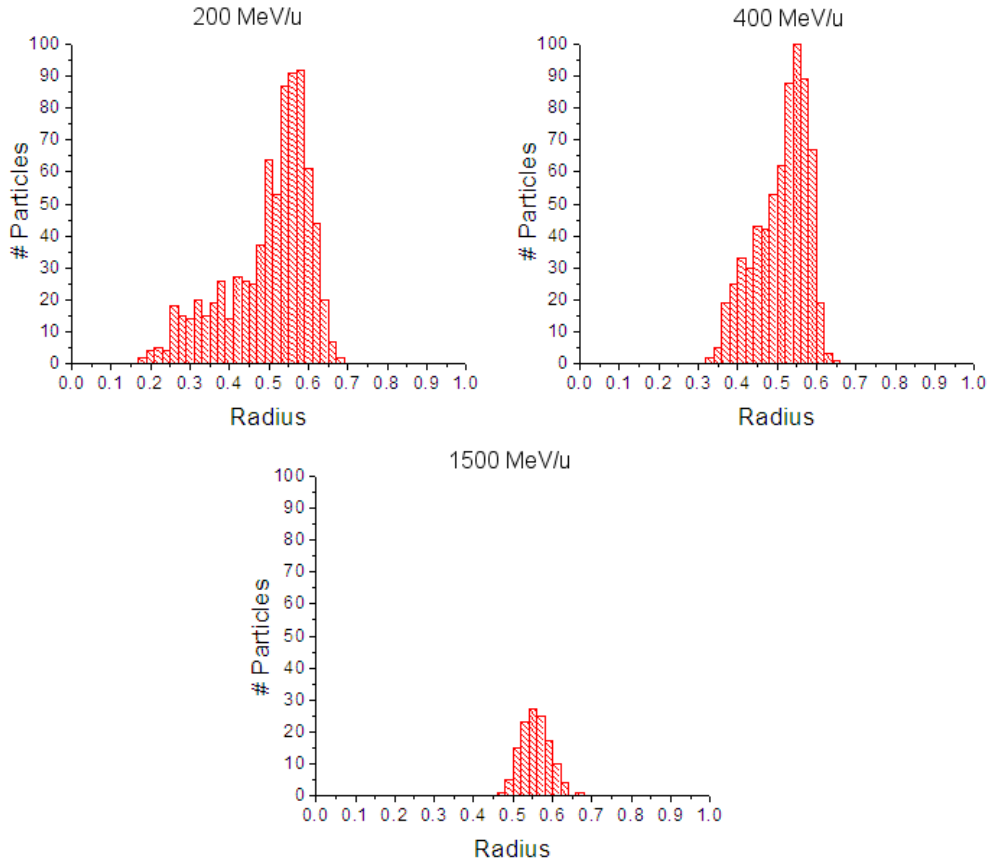

Figure 2.6. Histograms that represent the number of ^{132}Sn particles that have various radii after normalization to a unit sphere (Li Target). The cases are for a ^{238}U beam with energies of 200, 400, and 1500 MeV/u incident on a Li target.

$$a_{A,Z} = R_{A,Z} a_{max} a, \tag{2.37}$$

$$b_{A,Z} = R_{A,Z} b_{max} b, \tag{2.38}$$

$$\delta_{A,Z} = R_{A,Z} \delta_{max} \delta. \tag{2.39}$$

The initial coordinates of the fission and fragmentation products of the ^{238}U beam on the C and Li targets depend heavily on the A and Z of the product. Therefore, the products were classified into three groups: Group 1 ($A < 80$), Group 2 ($79 < A < 141$), Group 3 ($A > 140$). Interpolations for the maximum angles (a_{max}, b_{max}), maximum energy deviation (δ_{max}), and average energy of the uranium beam were constructed based on distributed data points in the A, Z plane. In addition to the maximum values of the phase space coordinates, the standard deviation $\sigma(A, Z)$ and average value $\mu(A, Z)$ of the Gaussian normalized coordinate distribution needed to be interpolated. The values of the coefficients for these polynomial interpolations for the three groups (mass ranges) are shown in Tables 2.2-2.4. Also shown (Figure 2.7) is the interpolation of the standard deviation as a function of energy and the nuclear mass, for masses between $A = 38$ and $A = 75$. The function that is plotted is

$$\begin{aligned} \sigma &= 6.30 \times 10^{-2} + 5.93 \times 10^{-5} E_{AVG} \\ &\quad + 2.78 \times 10^{-4} A - 1.35 \times 10^{-7} E_{AVG} A \\ &\quad - 2.48 \times 10^{-8} E_{AVG}^2 - 3.63 \times 10^{-6} A^2, \end{aligned} \tag{2.40}$$

The interpolating polynomial for the average energy of the fragment is a function of the energy of the uranium beam and the fragment's A and Z:

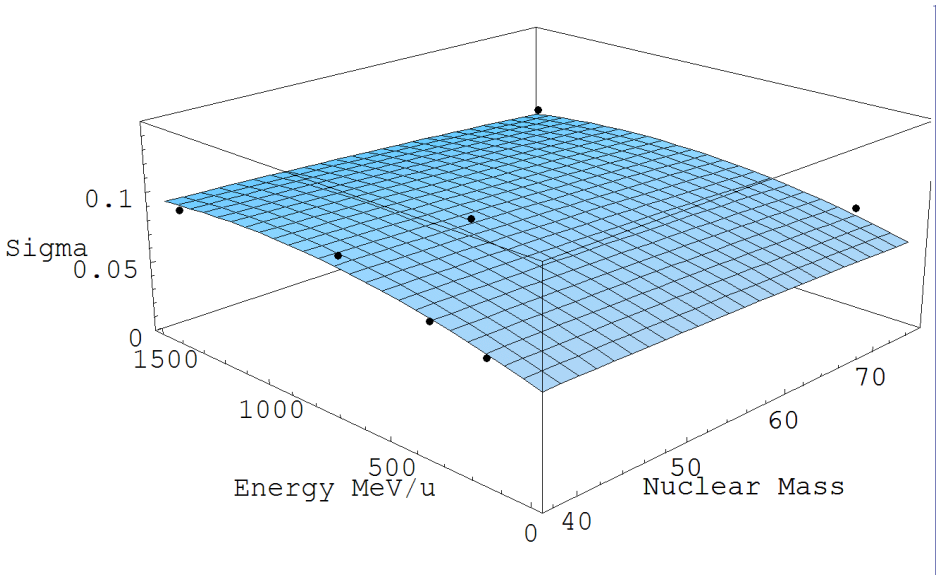

Figure 2.7. Interpolation for the standard deviation (sigma) of the normalized coordinates as a function of energy for nuclear masses from $A = 38$ to $A = 75$. Data points from MCNPX are shown to illustrate accuracy of the interpolation.

$$E_{AVG} = c_{1,1} + \frac{c_{1,3}}{E_U} + \frac{c_{1,4}}{A} + \frac{c_{1,5}}{Z} + c_{1,7}E_U + c_{1,8}A + c_{1,9}Z + c_{1,13}AE_U$$
$$+c_{1,14}ZE_U + c_{1,15}AZ + c_{1,17}E_U^2 + c_{1,18}A^2 + c_{1,19}Z^2. \quad (2.41)$$

The polynomial $P(m)$ for the interpolations of a_{max}, b_{max}, and δ_{max} are based on the energy of the uranium beam, the A and Z of the fragment, and the average energy of the fragment. The coefficients are the $c_{m,n}$'s where $m = 1 \rightarrow 5$ for E_{AVG}, σ, μ, $Angle_{max}$, and δ_{max}, respectively. The index n is the number of the line in Tables 2.2-2.4.

Table 2.2. Interpolation coefficients for Group 1 (A<80). The column with the heading "Exp" refers to the exponent of the interpolation variable. The first digit in the "Exp" column is the exponent of the variable "EAVG," the second is "EU," third is "A," and fourth is "Z."

$E_{avg}(MeV/u)$	σ	μ	$Angle_{max}$	δ_{max}	Exp
-6.87×10^{-2}	6.30×10^{-2}	5.99×10^{-1}	1.50×10^{-1}	3.34×10^{-1}	0000
0	0	0	1.09×10^{1}	1.99×10^{1}	-1000
0	0	0	0	0	0-100
0	0	0	0	0	00-10
0	0	0	0	0	000-1
0	5.93×10^{-5}	-4.07×10^{-4}	-9.52×10^{-6}	-9.85×10^{-6}	1000
8.45×10^{-1}	0	0	0	0	0100
3.52×10^{-1}	2.78×10^{-4}	-6.85×10^{-3}	-2.89×10^{-3}	-5.83×10^{-3}	0010
0	0	0	0	0	0001
0	0	0	0	0	1100
0	-1.35×10^{-7}	1.93×10^{-6}	0	0	1010
0	0	0	0	0	1001
1.31×10^{-3}	0	0	0	0	0110
0	0	0	0	0	0101
0	0	0	0	0	0011
0	-2.48×10^{-8}	1.30×10^{-7}	0	0	2000
3.46×10^{-5}	0	0	0	0	0200
-4.23×10^{-3}	-3.63×10^{-6}	6.40×10^{-2}	1.74×10^{-5}	3.58×10^{-5}	0020
0	0	0	0	0	0002

$$
\begin{aligned}
P(m) \;=\; & c_{m,1} + \frac{c_{m,2}}{E_{AVG}} + \frac{c_{m,3}}{E_U} + \frac{c_{m,4}}{A} + \frac{c_{m,5}}{Z} + c_{m,6}E_{AVG} \\
& + c_{m,7}E_U + c_{m,8}A + c_{m,9}Z + c_{m,10}E_{AVG}E_U \\
& + c_{m,11}AE_{AVG} + c_{m,12}E_{AVG}Z + c_{m,13}AE_U + c_{m,14}ZE_U \\
& + c_{m,15}AZ + c_{m,16}E_{AVG}^2 + c_{m,17}E_U^2 + c_{m,18}A^2 + c_{m,19}Z^2
\end{aligned}
\tag{2.42}
$$

Table 2.3. Interpolation coefficients for Group 2 (79<A<141). The column with the heading "Exp" refers to the exponent of the interpolation variable. The first digit in the "Exp" column is the exponent of the variable "EAVG," the second is "EU," third is "A," and fourth is "Z."

$E_{avg}(MeV/u)$	σ	μ	$Angle_{max}$	δ_{max}	Exp
2.95×10^{1}	-7.82×10^{-2}	5.32×10^{-1}	6.3×10^{-2}	7.07×10^{-2}	0000
0	0	0	7.25	1.91×10^{1}	-1000
0	0	0	0	0	0-100
0	0	0	0	0	00-10
0	0	0	0	0	000-1
0	5.68×10^{-6}	-6.81×10^{-5}	6.3×10^{-2}	7.07×10^{-2}	1000
1.01	0	0	0	0	0100
1.37	-1.05×10^{-2}	1.27×10^{-2}	-1.32×10^{-3}	-2.23×10^{-3}	0010
-4.95	3.03×10^{-2}	3.12×10^{-2}	2.47×10^{-3}	6.93×10^{-3}	0001
0	0	0	0	0	1100
0	8.63×10^{-8}	2.81×10^{-6}	0	0	1010
0	-6.72×10^{-7}	-5.64×10^{-6}	0	0	1001
3.56×10^{-5}	0	0	0	0	0110
1.55×10^{-5}	0	0	0	0	0101
1.91×10^{-1}	1.35×10^{-3}	4.16×10^{-4}	1.32×10^{-4}	8.22×10^{-4}	0011
0	8.42×10^{-9}	1.55×10^{-8}	0	0	2000
-3.35×10^{-6}	0	0	0	0	0200
-4.2×10^{-2}	-2.62×10^{-4}	-8.05×10^{-5}	-2.21×10^{-5}	-1.68×10^{-4}	0020
-2.01×10^{-1}	-1.77×10^{-3}	-5.75×10^{-4}	-1.9×10^{-4}	-1.04×10^{-3}	0002

2.3.3. Monte Carlo Implementation

A solely map-based approach is not sufficient to model the evolution of an exotic beam in the fragment separator. It is impossible to take into account fragmentation and fission of the beam in matter in such an approach. There are also many other effects that are nondeterministic. Stochastic effects such as energy and angular straggling in matter and charge exchange demand a Monte

Table 2.4. Interpolation coefficients for Group 3 (A>140). The column with the heading "Exp" refers to the exponent of the interpolation variable. The first digit in the "Exp" column is the exponent of the variable "EAVG," the second is "EU," third is "A," and fourth is "Z."

$E_{avg}(MeV/u)$	σ	μ	$Angle_{max}$	δ_{max}	Exp
-5.33×10^{1}	1.38×10^{-1}	-4.16×10^{-2}	5.44×10^{-2}	1.53×10^{-1}	0000
0	0	0	1.99	2.97	-1000
0	0	0	0	0	0-100
0	0	0	0	0	00-10
0	0	0	0	0	000-1
0	1.27×10^{-5}	4.19×10^{-5}	-2.47×10^{-6}	-1.38×10^{-6}	1000
1.02	0	0	0	0	0100
2.44×10^{1}	-5.89×10^{-4}	2.87×10^{-3}	-2.71×10^{-4}	-8.97×10^{-4}	0010
0	0	0	0	0	0001
0	0	0	0	0	1100
0	-1.62×10^{-7}	-7.7×10^{-7}	0	0	1010
0	0	0	0	0	1001
-1.23×10^{-5}	0	0	0	0	0110
0	0	0	0	0	0101
0	0	0	0	0	0011
0	7.84×10^{-9}	4.6×10^{-8}	0	0	2000
-8.48×10^{-6}	0	0	0	0	0200
-3.91×10^{-4}	2.01×10^{-6}	-6.77×10^{-6}	1.94×10^{-7}	1.08×10^{-6}	0020
0	0	0	0	0	0002

Carlo method. To compute the extent of the stochastic effects, the most up-to-date programs such as ATIMA for calculating energy loss and angular straggling have been integrated into COSY as simple procedures. A manual detailing the procedures invoked in the Monte Carlo code is found in Appendix A.

To get an accurate view of the evolution of the beam, any material that the beam passes through must be divided up into "slices." There are a couple of reasons to do this. One reason is that some of the rarer isotopes would not be

produced at all if the whole target or wedge material thicknesses were used. By the same argument, each slice cannot be too thick, as it won't account for multiple fragmentations or fissions. Having slices that are too thin increases the run time of the program. Also, the data acquired from MCNPX assumes a very thin thickness ($0.1068\ g/cm^2$), so any deviation from this thickness per slice will give increasingly inaccurate results. The approximations for the cross-sections and dynamics will be worse. A target thickness on this order will not be used for a FRIB, so for the most accurate approximations, more than one slice per target is used. The target thicknesses used would typically be about 30%-40% of the range of the primary beam in the target material. Convergence tests have been performed to determine how many slices are necessary for a normal target thickness. This value is approximately one slice per 10% of the projectile's range in the target material. The number of slices, however, is input by the user, so more slices or fewer slices may be used. Particles are transported through the target by computing the map of each target or wedge slice and, in addition, the beam is allowed to fragment or fission only once per slice. The results of the creation of the particles in each slice, and the dynamics that occur must be composed slice by slice to get the full results of the beam's isotopic composition and dynamics for a whole target or absorber.

2.3.4. File and Data Manipulations and Automated System Setup

New file and data constructs were a necessary addition to COSY for the Monte Carlo code to run quickly and efficiently. The procedures involved in tracking the

particles through the system is memory intensive and the amount of data that is generated is vast. For example, it is essential to keep track of how many particles of each type of isotope exist at key locations in the fragment separator. In addition, the coordinates and charge state of each particle must also be known. It was realized that the best way to keep track of these data was to have two different types of files: "ISOTOPES.DAT" and PARTICLESAAAZZZ.DAT." In addition, a HISTORY.DAT file is needed to keep track of what type and how many of each isotope are formed from other isotopes. The ISOTOPE.DAT file's purpose is to keep track of the total number of particles in the system, the A and Z of each isotope created in target or absorber material, and the number of each isotope. This file is updated for every section of the fragment separator and for every slice of target or wedge material. There exists one PARTICLESAAAZZZ.DAT file for every isotope in the system. In each file there is one entry for each particle of the isotope. This entry contains the unique ID, charges state Q of the particle, as well as all phase space coordinates of the particle, including magnetic rigidity. These files are updated by applying the map of each fragment separator section to the coordinates. A detailed description of these files is located in Appendix B. For typical cases, the data generated for the target is 600-700 MB and for the whole system up to around 2 GB.

A directory structure was developed to keep track of the isotope and particle files at key locations in the fragment separator. These locations include the target, after optics of first section, collimation before first wedge, after wedge, optics of

second half, and collimation at the end (achromatic image point). For a two-stage separator, the second stage directory is identical in directory structure. In the case of a fragment separator with gas cell branch there are subdirectories for the optics of the gas cell branch, collimation before the monochromatic wedge, and the monochromatic wedge itself.

A user-input section is located in the code. This allows the user to specify parameters and employ certain features of the code without requiring great study of the code itself. This section is quite simple with explanations given for each input parameter. A list of these input parameters are given in Table C.1 located in Appendix C. Once the program containing this input is executed, the code is fully automated and requires no further user interaction.

2.3.5. Steps in the Monte Carlo Calculations

All bookkeeping and particle tracking procedures are executed for each slice. The procedure "SLICE" is executed once per slice, which calculates all of the characteristics of the beam as it passes through matter. These characteristics include charge states, energy loss and angular straggling, and fragmentation and fission. The procedure "ABSORBER" passes the results of one slice on to the next. The steps followed for each slice of target or absorber material are illustrated in a flow chart shown in Figure 2.8.

2.3.5.1. Transport. Since there are isotopes of many A, Z combinations, energies, and coordinates, the effective thickness that each isotope sees can be quite

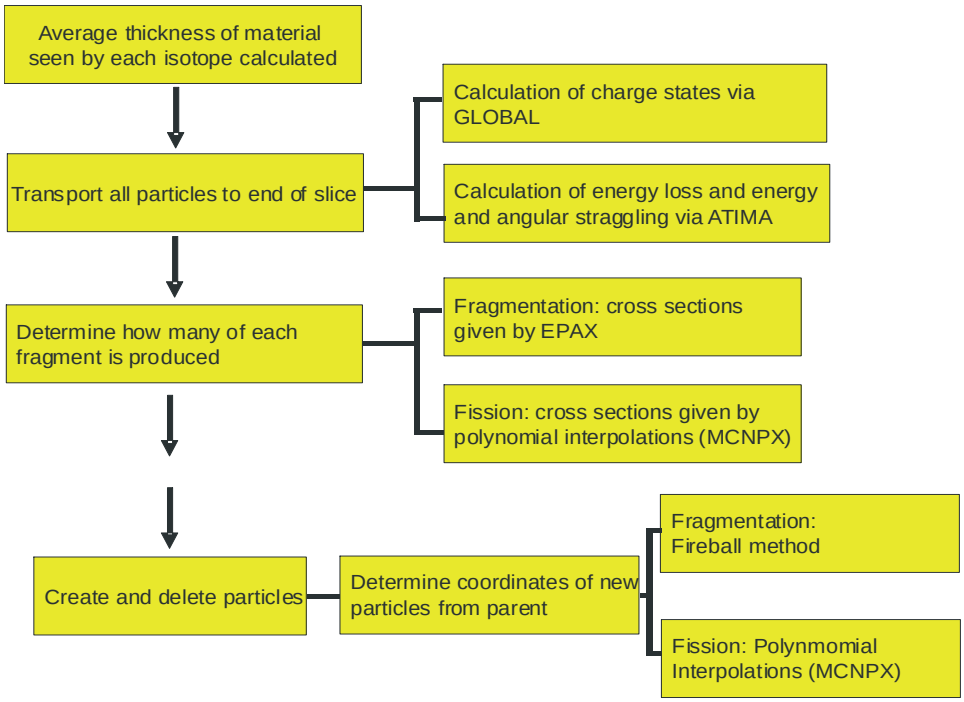

Figure 2.8. Flow chart representing the main steps followed in the Monte Carlo code.

different. We begin by calculating the average thickness seen by each type of isotope by randomly selecting, for each isotope, 1000 (or less if 1000 do not exist) particles from the PARTICLESAAAZZZ.DAT file for each isotope. These particles are sent through the slice and the average thickness is computed and saved for later use in calculating charge exchange and the cross-section, since these calculations are based on the thickness of the target or absorber. After the average

thickness is calculated, the particles are transported to the end of the slice by applying the map of one absorber slice to the particle coordinates that are in the file. The resulting new coordinates are used as initial coordinates for the following slice. At the end of the slice, the charge state is determined for each particle. This can be done in two ways and is chosen by an option in the user input section: either the average thickness of each isotope is used to calculate the new charge state or the new charge state can be determined particle by particle, i.e., looking at the thickness of each slice that each individual particle sees. The former is a much faster method than the latter. The energy loss and energy and angular straggling are computed using ATIMA [**25**].

2.3.5.2. Determine How Many Particles Are Produced. The next step is to determine how many new particles are created by the fragmentation or fission of the beam in a particular slice. The cross-section is determined from EPAX in the case of fragmentation, where the existing isotopes are entered as input parameters along with the average thickness seen by each isotope. The cross-section is calculated internally by EPAX, and returned for use in calculating how many new particles of each isotope are produced by using Eqn 2.30. For fission, the process is the same except the cross-section is returned by the MQECROSS procedure, which returns the cross-section that is computed by a second-order polynomial in energy based on data provided by the program MCNPX.

2.3.5.3. Create and Delete Particles. The coordinates of the new particles are determined by the particle from which they are created in both the fragmentation

and fission cases. In the fragmentation case, new particles will have coordinates chosen by the Fireball method, where the momentum of the new particle is chosen from a Gaussian distribution based on the nuclear masses of the parent and child particles (Eqn 2.29). This method is not valid for determining the coordinates of a fission product, however. The dynamics of the fission products are dependent on the energy of the ^{238}U primary beam. Polynomial interpolations for the mean and standard deviation are used to randomly pick the coordinates of the child particles from a Gaussian distribution.

After the new particles are created, there must be a certain number of old particles deleted. In the Fireball method it is assumed that there is a one-to-one correspondence in the number of particles created and deleted. For fission, however, this is not the case. More than one new particle can come from one nucleus. For fission, by examining how many ^{238}U nuclei remain after all the residuals are created in the output from MCNPX, we could determine how many to delete from the PARTICLESAAAZZZ.DAT and ISOTOPES.DAT files. A simple polynomial interpolation in the energy of the ^{238}U beam is used to find how many to delete as a function of energy. Once it is known how many to delete, then the particular particles to be deleted in PARTICLESAAAZZZ.DAT are determined randomly.

CHAPTER 3

Fragment Separator Design

The general method used for separation of isotopes of different rigidities is called the $B\rho-\Delta E-B\rho$ (rigidity-energy loss-rigidity) method, which makes use of dipole magnets for rigidity selection and an energy absorber to achieve an additional dependence on the A and Z of the isotope since each isotopes loses energy at a different rate in a given absorber material. These concepts are illustrated in Figure 3.1, where a one-stage separator is shown with a gas cell branch to capture the selected ion in a He gas catcher. A separation may be enhanched by including multiple separation stages with the $B\rho - \Delta E - B\rho$ method.

When the fragment separator is designed, the magnet optics are determined first without the wedge absorber. This is necessary because the wedge will amplify any existing aberrations in the system and destroys some symmetries that are useful in the basic design. The first-order layout is determined first, with the constraints explained below. The use of symmetries in the design of the fragment separator optics has the effect of eliminating or constraining certain coefficients in the map [**27**]. This method leads to optical solutions that are inherently lower in aberrations. The various symmetries which are exploited include time independence, mid-plane, symplectic, and mirror symmetry.

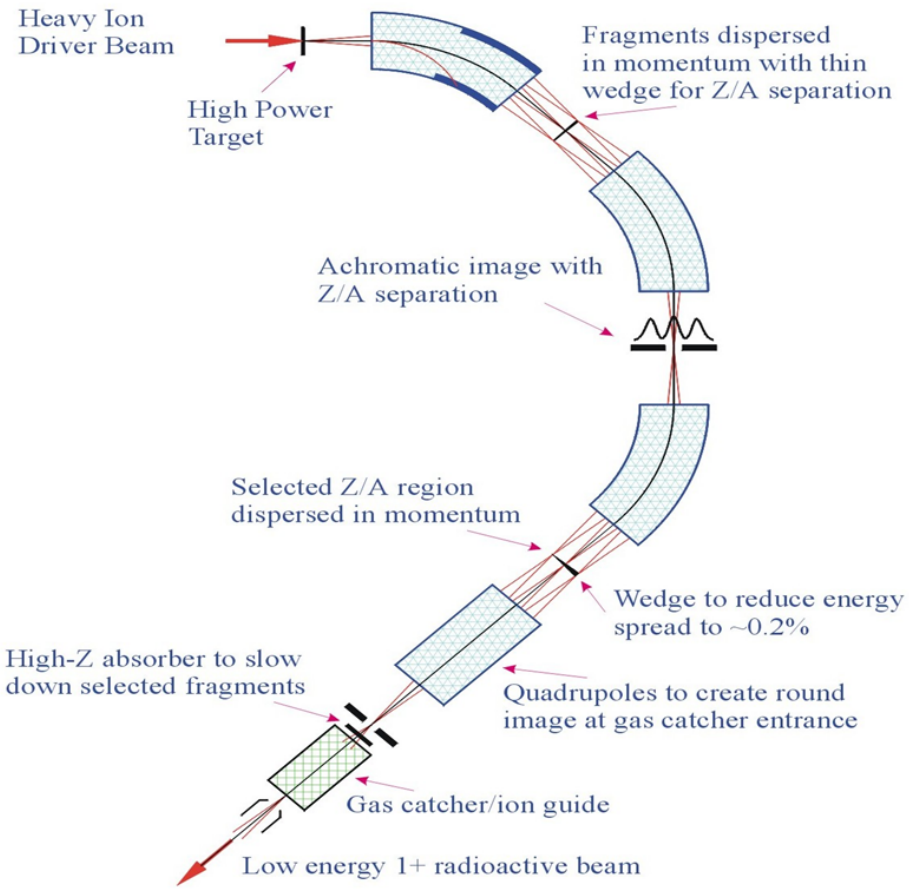

Figure 3.1. Overhead view of one-stage separator with gas cell branch showing how particles are separated at each stage.

3.1. Symmetries Used in Fragment Separator Design

3.1.0.4. Time-independence symmetry. Since there are no time-dependent fields in the fragment separator, the energy of the system is conserved. This condition implies that all derivatives in the map with respect to the time-of-flight-like coordinate, l, are zero except for the first-order matrix element $(l|l) = 1$. The element $(\delta|\delta) = 1$. So all of the δ-dependent aberrations are zero.

3.1.0.5. Mid-plane symmetry. For the layout of the fragment separator with the x-plane as the separation plane, the system is constrained to have $y = 0$ as the symmetry plane. This condition cancels half of the aberrations, given by:

$$(x|x^{i_x}a^{i_a}y^{i_y}b^{i_b}l^{i_l}\delta^{i_\delta}) = 0 \text{ if } i_y + i_b \text{ is odd}, \tag{3.1}$$

$$(a|x^{i_x}a^{i_a}y^{i_y}b^{i_b}l^{i_l}\delta^{i_\delta}) = 0 \text{ if } i_y + i_b \text{ is odd}, \tag{3.2}$$

$$(y|x^{i_x}a^{i_a}y^{i_y}b^{i_b}l^{i_l}\delta^{i_\delta}) = 0 \text{ if } i_y + i_b \text{ is even}, \tag{3.3}$$

$$(b|x^{i_x}a^{i_a}y^{i_y}b^{i_b}l^{i_l}\delta^{i_\delta}) = 0 \text{ if } i_y + i_b \text{ is even}, \tag{3.4}$$

$$(l|x^{i_x}a^{i_a}y^{i_y}b^{i_b}l^{i_l}\delta^{i_\delta}) = 0 \text{ if } i_y + i_b \text{ is odd}, \tag{3.5}$$

$$(\delta|x^{i_x}a^{i_a}y^{i_y}b^{i_b}l^{i_l}\delta^{i_\delta}) = 0 \text{ if } i_y + i_b \text{ is odd}. \tag{3.6}$$

3.1.0.6. Symplectic symmetry. Since the fragment separator is basically a system of magnetic fields, it is Hamiltonian and, therefore, obeys symplectic symmetry. This symmetry, in terms of the map M is $M = Jac(\mathcal{M})$, where $Jac(\mathcal{M})$ is the Jacobian of map $\mathcal{M}$, and can be expressed as

$$M^T J M = J, \tag{3.7}$$

where J is a $2n \times 2n$ matrix with the form

$$J = \begin{pmatrix} 0 & I \\ -I & 0 \end{pmatrix}, \tag{3.8}$$

where I is the $n \times n$ unit matrix.

3.1.0.7. Mirror symmetry. Time reversal or "mirror symmetry" occurs in electromagnetic fields and, hence, the fragment separator. This indicates that if the system evolves forward in time to some final configuration, then the time reversal operator applied to the final configuration will lead back to the initial configuration of the system. $\mathcal{M}_r$ is the map of the system in reversed order and the time reversal operator is defined as

$$\mathcal{R}(x, a, y, b, l, \delta) = (x, -a, y, -b, -l, \delta). \tag{3.9}$$

This implies that

$$\mathcal{M}_r \circ \mathcal{R}(\vec{z}_f) = \mathcal{R}(\vec{z}_i) \tag{3.10}$$

or

$$\mathcal{M}_r = \mathcal{R} \circ \mathcal{M}^{-1} \circ R. \tag{3.11}$$

The relations derived from this condition can be found in [**27**].

3.2. Fragment Separator Optics

In addition to the symmetries described above, there are many key optical properties that an operational fragment separator must possess. These properties assume the primary beam fragments or fissions in the target and the optical setup begins adjacent to the location from which the isotopes are produced. Also, it is assumed that they are confined in a small area of real space in the xy-plane. It is understood that large variations in the angular divergences (a,b) and energy divergence (δ) are possible.

The fragment separator must be imaging. This means that the final positions of the particles in the beam must be independent of initial angle. This property is called "point-to-point," which mathematically means that the linear matrix elements $(x|a)$ and $(y|b)$ are zero. Also, the beam must be "parallel-to-parallel." The final angles of the beam are independent of initial position. In this case the linear matrix elements $(a|x)$ and $(b|y)$ must be zero. Also, it is imposed by mirror symmetry that $(a|\delta)$ be zero [**27**]. In other words, the final angles are independent of the initial energy divergence. The magnification of the separator without the energy absorber is unity, so $(x|x) = 1$. This indicates that the beam is the same size at the beginning and end of a separation stage to first order. If the energy absorber is added to the system, then the magnification is slightly higher and the

beam size is increased at the end of a separation stage. An example of a general fragment separator is shown in Figure 3.2.

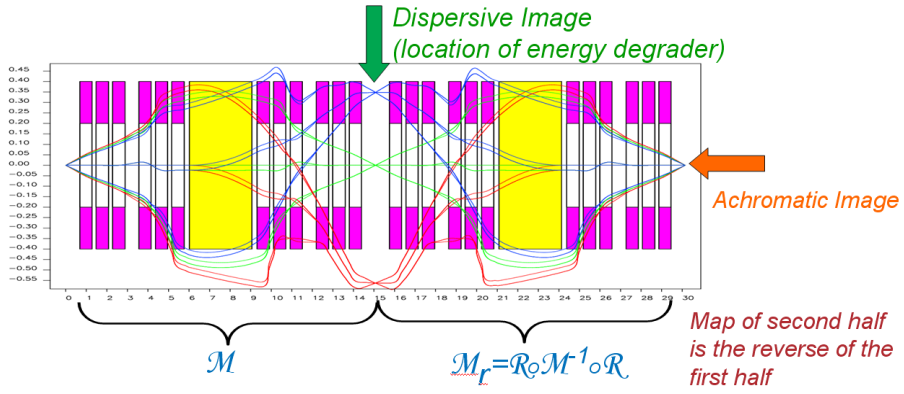

Figure 3.2. Example of a fragment separator. The dispersive image is indicated by the green arrow. The achromatic image is indicated by the orange arrow. The map of the second half of the separator is the reverse of the first half. Multipoles are shown in pink and dipoles in yellow. The green rays represent particles of a reference rigidity. Blue rays indicate particles of higher rigidity and red rays have lower rigidity. The map of the first half of the separator is represented by M, and the second half is the reverse of the first half and represented by the map M_r.

3.3. Optimized Third-Order Fragment Separator

After making use of symmetries in the design principle and numerical optimization with wedge computation at higher orders, a separator was designed to be nearly aberration-free to third order. The parameters of this design are outlined in Table 3.1 and are shown for a beam rigidity of 8 Tm. This is the design which

Table 3.1. Fragment separator parameters for a beam with rigidity 8 Tm. Field strengths are given at distances from beam axis.

	Field Strength at 20 cm (T)	**Field Strength 40 cm (T)**
Quadrupoles		
Q1	1.1709	2.3422
Q2	-1.2087	-2.4174
Q3	-1.2076	-2.4152
Q4	1.1009	2.2019
Sextupoles		
S1	0	0
S2	0.1240	0.4960
S3	0.1617	0.6468
S4	-0.2114	-0.8456
Octupoles		
O1	0.0533	0.4264
O2	0.2200	1.7600
O3	0.2668	2.1344
O4	-0.0886	-0.7088
O5	-0.0639	-0.5112
O6	0.0420	0.3360
O7	0.0946	0.7568
O8	0.0632	0.5056
Dipoles		
Radius (m)	5	
Angle (degrees)	35	
Gap Width (m)	0.212	
Field (T)	1.5997	
Drifts		
L1	0.40	
L2	0.25	
L3	0.10	

is used in examples throughout this thesis, with magnets scaled for the rigidity of the isotope to be selected.

The design consists of the first quarter containing two quadrupole doublets with sextupole and octupole terms, followed by a dipole. The first half is mirror symmetric about the dipole. In addition, the second half is mirror symmetric to the first half, making the whole system double mirror symmetric. The first-order layout is shown in Figure 3.3. The beam envelope for a typical ^{132}Sn rare isotope beam remains mostly contained within the magnet apertures to a third-order approximation. The third-order beam trajectories are shown in Figure 3.4 as projections in the xz-plane and yz-plane. A view of the fragment separator from above is shown in Figure 3.5.

3.4. An Alternate Fragment Separator Design

An alternate third-order design for the fragment separator was developed in an attempt to find an even better solution to reduce aberrations. While the design presented here meets this qualification, it is impossible to build with the given superconducting magnet technology due to the extreme field strengths as shown in Table 3.2 for the octupole strengths. In addition to this problem, there is also a very large beam envelope that occurs with this design. In practice this would translate into great reduction in transmission due to losses of of exotic fission products emitted with large angles and energy deviations.

The design consists of six quadrupole magnets with sextupole and octupole terms, followed by a dipole. The quadrupole and sextupole terms are mirror symmetric about the dipole and, as in the layout in the original design, also have

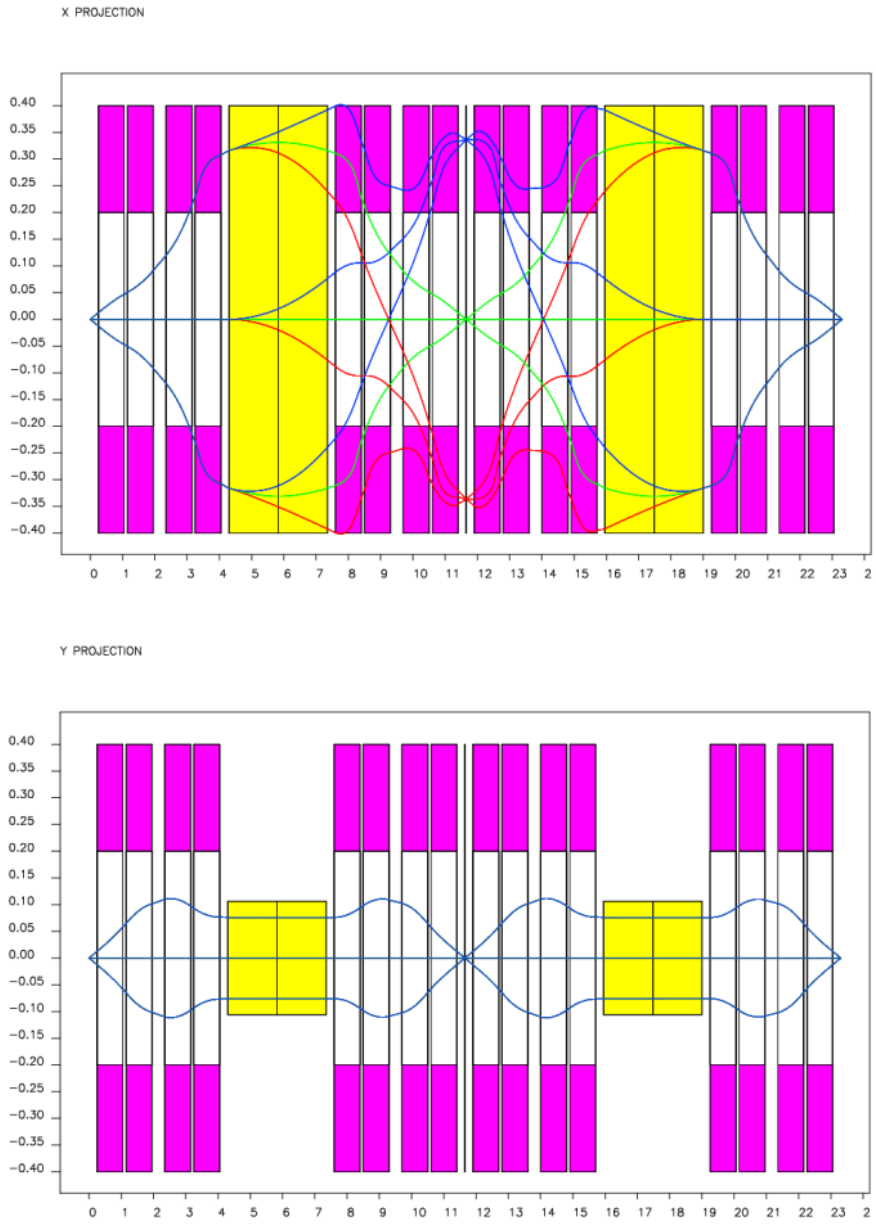

Figure 3.3. First-order beam trajectories in a one-stage separator. x-projection is shown above and y-projection below. Multipole magnets are shown in pink and dipoles in yellow. The green rays represent particles of a reference rigidity. Blue rays indicate particles of higher rigidity and red rays have lower rigidity. The scale is in meters.

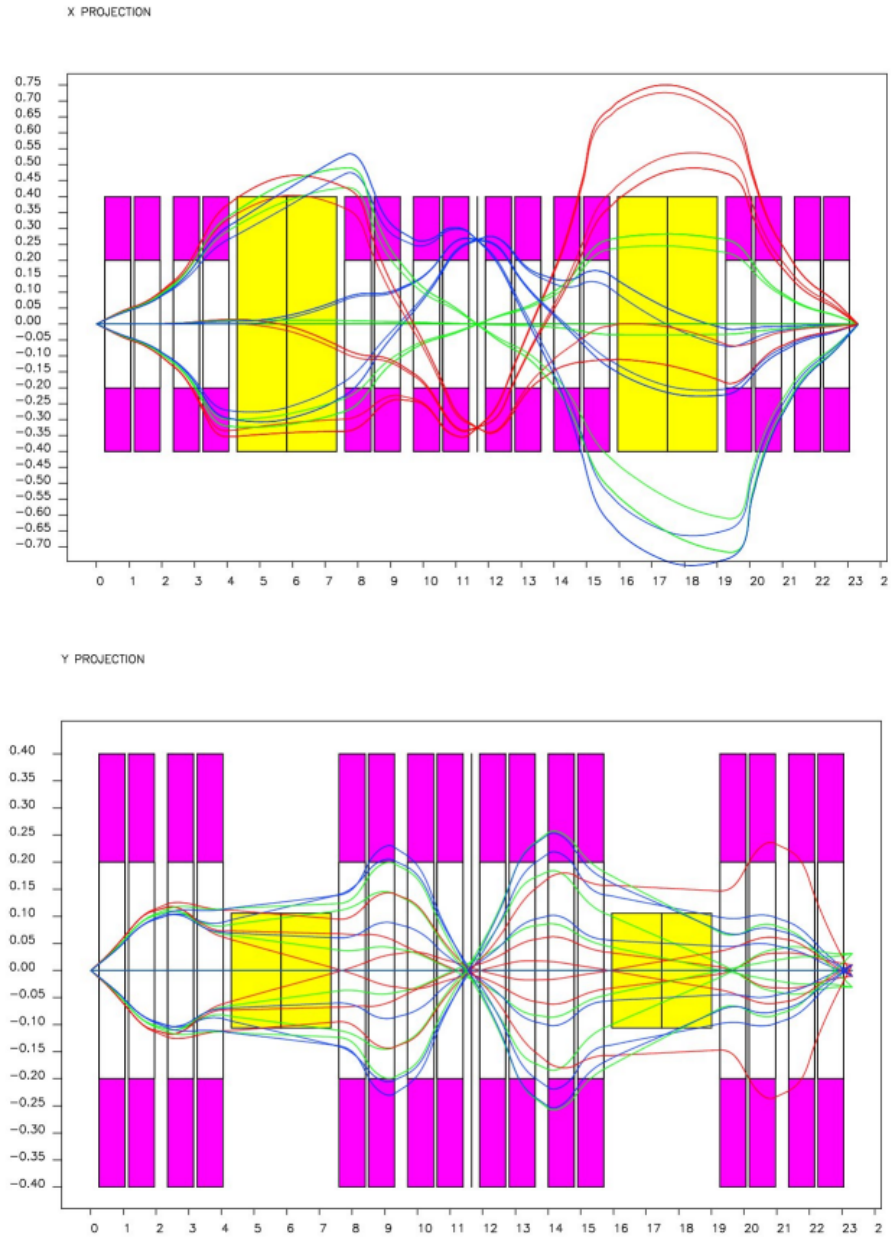

Figure 3.4. Third-order beam trajectories in a one-stage separator. x-projection is shown above and y-projection below. Multipole magnets are shown in pink and dipoles in yellow. The green rays represent particles of a reference rigidity. Blue rays indicate particles of higher rigidity and red rays have lower rigidity. The scale is in meters.

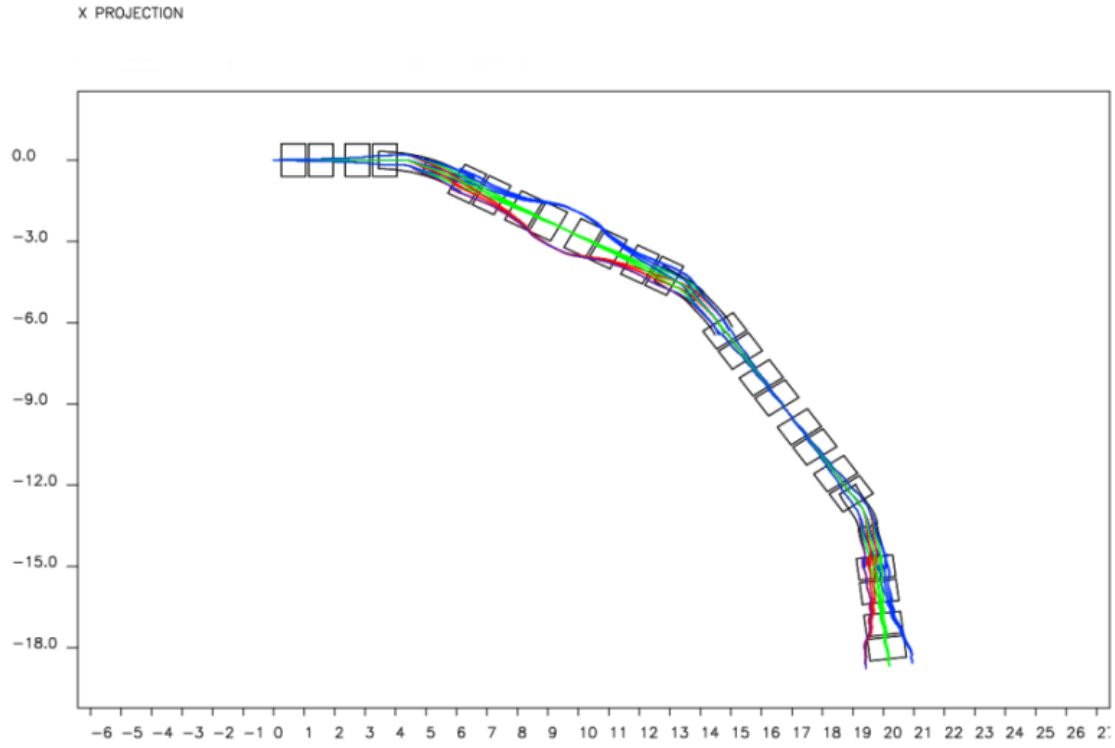

Figure 3.5. A view of the chosen fragment separator design from above. The scale of x (vertical) and z (horizontal) is in meters.

mirror symmetry about the center of the fragment separator and, hence, double mirror symmetry.. The octupole terms, however, do not have this characteristic. There are twelve independent octupole terms that are mirror symmetric only about the center of the separator. The values of the magnets are shown in Table 3.2. The drift lengths between the magnets are as follows: 1.2 m before the first multipole and after the third, 0.42 m between multipoles, and 0.2 m between dipoles and multipoles. All of the drift lengths exhibit double mirror symmetry. The layout is shown below in Figures 3.6.

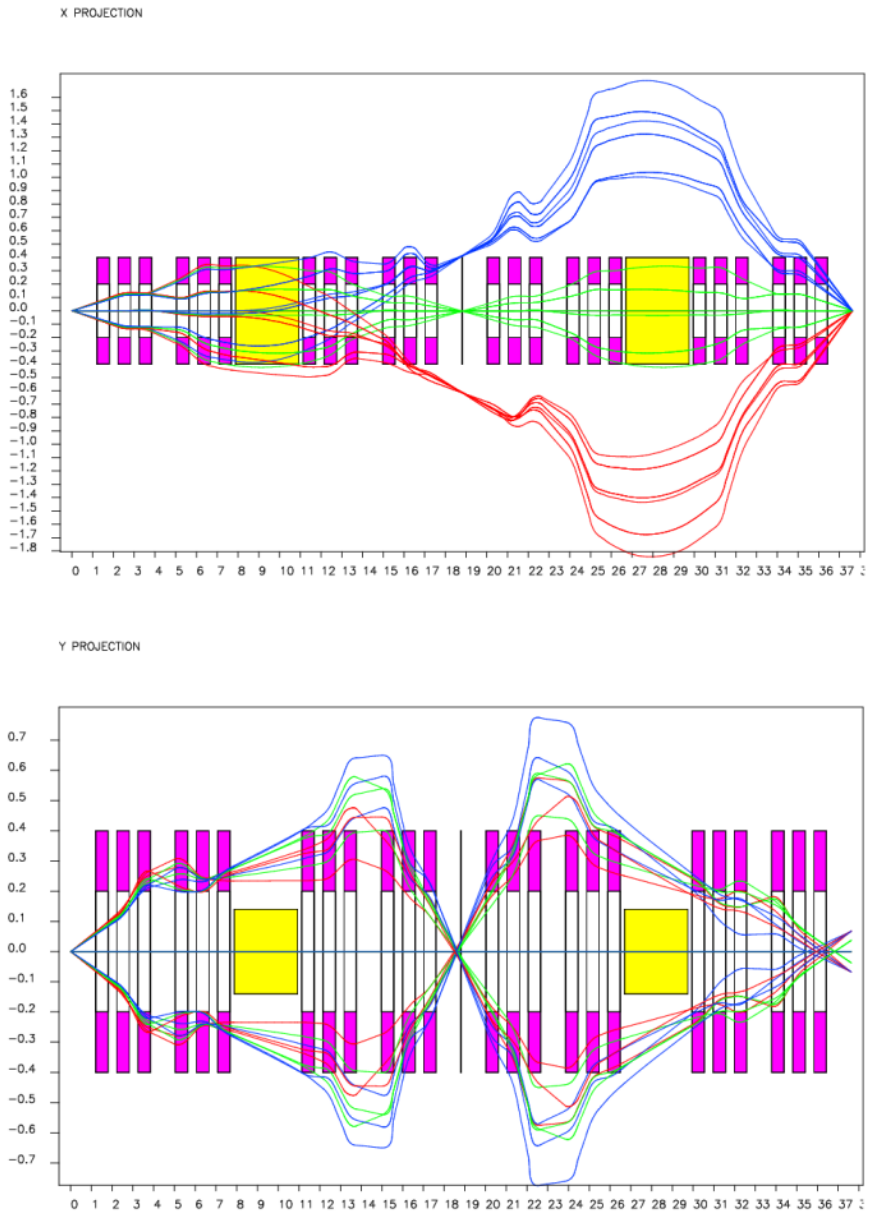

Figure 3.6. Alternative design for fragment separator. Third-order beam trajectories in a one-stage separator. x-projection is shown above and y-projection below. Multipole magnets are shown in pink and dipoles in yellow. The green rays represent particles of a reference rigidity. Blue rays indicate particles of higher rigidity and red rays have lower rigidity. The scale is in meters.

Table 3.2. Alternate fragment separator parameters for a beam with rigidity 8 Tm. Field strengths are given at distances from beam axis.

	Field Strength at 20 cm (T)	**Field Strength at 40 cm (T)**
Quadrupoles		
Q1	0.0033	0.0068
Q2	2.3203	4.6406
Q3	-2.5352	-5.0704
Q4	-1.3182	-2.6365
Q5	1.4872	2.9743
Q6	0.0030	0.0060
Sextupoles		
S1	-0.4400	-1.7600
S2	0.7331	2.9326
S3	-0.6500	-2.600
S4	0.2500	0.9983
S5	0.1132	0.4529
S6	-0.1372	-0.5490
Octupoles		
O1	0.2190	1.7490
O2	0	0
O3	-0.7498	-5.9986
O4	0.4134	3.3075
O5	0	0
O6	-0.0540	-0.4318
O7	-0.0251	-0.2008
O8	0	0
O9	-0.0604	-0.4832
O10	0.2194	1.7555
O11	0	0
O12	-0.4012	-3.2096

3.5. General Optics with Absorber Wedge

The absorber wedge is an element of the fragment separator that allows further purification of a rare isotope beam by exploiting energy loss characteristics of the

isotope that the fragment separator is tuned for. The energy loss of each isotope is according to its nuclear mass A and nuclear charge Z and also depends on the type of material used for the absorber. Absorber wedges are typically made out of aluminum for rare isotope experiments, since a low Z material minimizes straggling, but other materials may be used as well.

The wedge is typically run in achromatic mode, where the wedge has variable thickness along the separation plane. The location of the wedge is typically at a dispersive image of the separator, where the isotopes are dispersed in x according to rigidity. At the dispersive image, higher rigidity particles will pass through larger thicknesses of material and low-rigidity particles will traverse smaller thicknesses. The wedge is shaped such that the coordinate δ is kept constant for all particles of the selected isotope. As particles with different A, Z pass through the wedge, they are deflected so that their trajectories put them at a different location than the selected isotope at the end of the separator. A monochromatic wedge is also possible, but will require a different shaping in x such that $\delta = 0$ for the chosen isotope after it passes through the wedge. Figure 3.7 shows the wedge's integration into the fragment separator.

3.6. Second-Order Analytic Theory with Absorber Wedge

For optimal separation of rare isotopes, the $B\rho - \Delta E - B\rho$ (rigidity-energy loss-rigidity) separation method is used. In order to achieve energy loss that will aid in the selection of isotopes, beam-material interactions must be exploited by

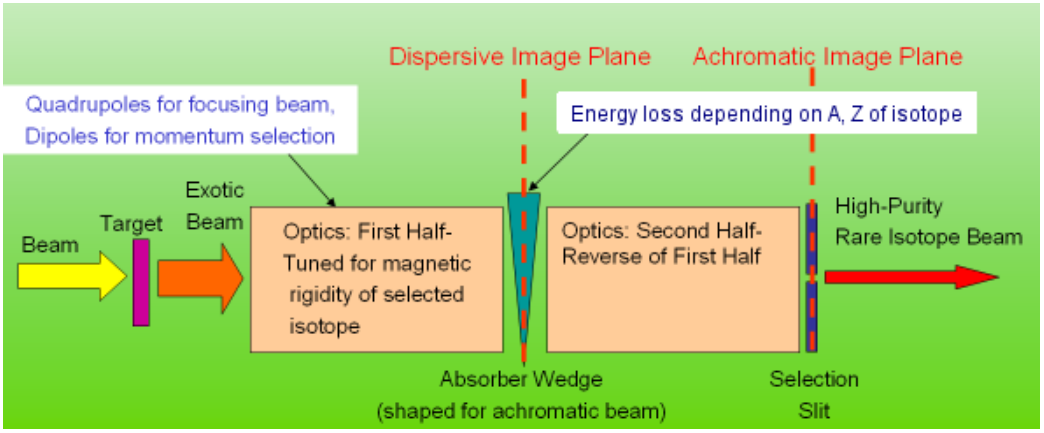

Figure 3.7. Diagram depicting the absorber's integration into the optical system.

using shaped absorber wedges. In the map approach, the wedge absorber is viewed as an optical element, where it is represented by the map of a drift with energy loss. The map of the wedge has six components. The first four (x, a, y, b) are the components of a drift. The fifth is related to the time of flight and is omitted here. The sixth is the momentum component that is given by Eqn 3.12:

$$\begin{aligned}(3.12) \qquad \delta_f \;=\; & (\delta|x)_w x_i + (\delta|a)_w a_i + (\delta|\delta)_w \delta_i + (\delta|xx)_w x_i^2 \\ & + (\delta|xa)_w x_i a_i + (\delta|aa)_w a_i^2 + (\delta|x\delta)_w x_i \delta_i \\ & + (\delta|a\delta)_w a_i \delta_i + (\delta|bb)_w b_i^2 + (\delta|\delta\delta)_w \delta_i^2,\end{aligned}$$

where the subscript w denotes a wedge map element.

It is important to know which symmetries described in the previous section are broken or maintained by the introduction of the wedge. The wedge will maintain midplane symmetry but will break the time independence, mirror, and symplectic symmetry used in the design of the fragment separator optics. One of the issues with the wedge is to see whether or not some of the properties of the mirror-symmetric symplectic system can be recovered. Since there is energy loss in the wedge, the symplectic symmetry is lost because the system is no longer Hamiltonian. Fortunately, symplectic symmetry only enters into the fragment separator design at third order. Mirror symmetry alone determines the layout up to second order. It is necessary to determine whether it is possible to keep the whole separator with the energy absorber mirror symmetric. For this to happen, time reversal invariance is necessary. This property is described in the following way: if a particle enters the absorber with δ_i and exits with δ_f, then going backwards in time it would enter with δ_f and exit with δ_i along the same trajectory. Logically, this is possible since there is no fundamental physics law involving energy loss of heavy charged particles in matter that forbids it.

Since the beam-material interactions in the wedge such as fragmentation and multiple Coulomb scattering induce detrimental stochastic effects, it is necessary to minimize the amount of material in the system. Also, as described above, it is optimal to place the wedge at a mirror symmetric point in the system. It follows from the mirror symmetric layout that a particle entering the wedge with a particular δ_i will also exit with the same δ_i. So, the absorber wedge should preserve

the existing dispersion without the absorber. From Eqn 3.12, it follows that $(\delta|x)_w \neq 0$ and x_i should be δ_i-dependent. This implies that the absorber should be placed at the dispersive image of the fragment separator. $(\delta|x)_w$ being nonzero requires that the absorber should have a thickness variation in x. This means that the absorber should be wedge-shaped. If this is done, it induces a nonzero $(\delta|a)_w$. At second order we can control the quantity $(\delta|xx)_w$ by introducing a symmetric surface curvature to the wedge. By modifying the thickness of the wedge at the center, $(\delta|\delta)_w$ and $(\delta|\delta\delta)_w$ can be controlled somewhat.

In order to see the aberrations of the full system, one must compose the wedge map with map of the rest of the separator optics. The optical design of the fragment separator is a second order achromat. This was computed in [**27**]. The map for the system up to the mirror symmetric point is given by Eqns 3.13-3.17.

$$
\begin{aligned}
(3.13) \qquad x_f &= -x_i + (x|\delta)\delta_i + (x|xx)x_i^2 + (x|aa)a_i^2 \\
&\quad +(x|x\delta)x_i\delta_i + (x|yy)y_i^2 + (x|bb)b_i^2 + (x|\delta\delta)\delta_i^2, \\
(3.14) \qquad a_f &= -a_i + (a|xa)x_ia_i + (a|a\delta)a_i\delta_i + (a|yb)y_ib_i, \\
(3.15) \qquad y_f &= -y_i + (y|xy)x_iy_i + (y|ab)a_ib_i + (y|y\delta)y_i\delta_i, \\
(3.16) \qquad b_f &= -b_i + (b|xb)x_ib_i + (b|ay)a_iy_i + (b|b\delta)b_i\delta_i, \\
(3.17) \qquad \delta_f &= \delta_i
\end{aligned}
$$

The map for the second half is just the reverse of 3.13-3.17. This can be computed by Eqn 3.11. Up to second order, the map of the full system is the identity without the wedge. This is also shown in [**27**]. The entire map is computed by

$$\mathcal{M}_{tot} = R \circ \mathcal{M}^{-1} \circ R \circ \mathcal{M}_d\left(-\frac{l_w}{2}\right) \circ \mathcal{M}_w \circ \mathcal{M}_d\left(-\frac{l_w}{2}\right) \circ \mathcal{M}, \tag{3.18}$$

where l_w is the length of the central thickness of the wedge. Analytically, this composition can be performed by a program such as MATHEMATICA [**28**]. To first order the result is:

$$M_{tot} = \begin{pmatrix} 1-(x|\delta)(\delta|x)_w & (x|\delta)[\frac{l_w}{2}(\delta|x)_w - (\delta|a)_w] & 0 \\ 0 & 1 & 0 \\ 0 & 0 & 1 \\ 0 & 0 & 0 \\ -(\delta|x)_w & \frac{l_w}{2}(\delta|x)_w - (\delta|a)_w & 0 \end{pmatrix} \tag{3.19}$$

$$\begin{pmatrix} 0 & (x|\delta)[(x|\delta)(\delta|x)_w + (\delta|\delta)_w - 1] \\ 0 & 0 \\ 0 & 0 \\ 1 & 0 \\ 0 & (x|\delta)(\delta|x)_w + (\delta|\delta)_w \end{pmatrix}.$$

Two parameters are free to choose. Both the length and the opening angle of the wedge can be changed in order to simplify Eqn 3.19. In a realistic case, the reaction kinematics in a thick target would lead to particles having large initial angles (a) and large energy spreads (δ). This means that the two parameters should be used to minimize $(x|a)_{tot}$ and $(x|\delta)_{tot}$. The opening angle of the wedge will determine $(\delta|x)_w$ and the length l_w will influence the values of $(\delta|\delta)_w$ and $(\delta|a)_w$. For a given beam-wedge combination, the angle and length can be modified to satisfy Eqns 3.20 and 3.21:

$$\frac{l_w}{2}(\delta|x)_w - (\delta|a)_w = 0 \tag{3.20}$$

$$(x|\delta)(\delta|x)_w + (\delta|\delta)_w - 1 = 0. \tag{3.21}$$

These conditions determine the optimal wedge parameters from the point of view of the optics. Given this simplification Eqn 3.19 is reduced to:

$$M_{tot} = \begin{pmatrix} (\delta|\delta)_w & 0 & 0 & 0 & 0 \\ 0 & 1 & 0 & 0 & 0 \\ 0 & 0 & 1 & 0 & 0 \\ 0 & 0 & 0 & 1 & 0 \\ -(\delta|x)_w & 0 & 0 & 0 & 1 \end{pmatrix}. \tag{3.22}$$

Eqn 3.20 happens to be a geometrical condition that is always satisfied. A proof of this can be found in [**29**]. This condition implies that the wedge maintains the imaging property of the system for any wedge thickness. Also, for a given thickness, there is one angle that cancels the total dispersion. The thickness is a free parameter and can be used to optimize quantities like the resolution of the separator.

Eqn 3.22 is proof that the identity map cannot be recovered when the wedge is in the system. The magnification, $(x|x)_{tot} = (\delta|\delta)_w$, will always be greater than unity. There will always be an increased momentum spread that is directly proportional to the initial size of the beam. Since the determinant of Eqn 3.22 is equal to $(\delta|\delta)_w$, there will always be an increase in transverse emittance.

The map at second order is very complicated, but it can be simplified by assuming that the initial beam size is very small ($x_i, y_i \rightarrow 0$). If this assumption is made, then the second-order map is given by:

$$x_f = (x|aa)_{tot}a_i^2 + (x|a\delta)_{tot}a_i\delta_i + (x|bb)_{tot}b_i^2 + (x|\delta\delta)_{tot}\delta_i^2, \tag{3.23}$$

$$a_f = 0, \tag{3.24}$$

$$y_f = 0, \tag{3.25}$$

$$b_f = 0, \tag{3.26}$$

$$\delta_f = (\delta|aa)_{tot}a_i^2 + (\delta|a\delta)_{tot}a_i\delta_i + (\delta|bb)_{tot}b_i^2 + (\delta|\delta)_{tot}\delta_i^2. \tag{3.27}$$

The total map terms that are explicit in x_f are:

$$\begin{aligned}(x|aa)_{tot} &= (x|aa)[1-(\delta|\delta)_w] - \frac{l_w}{2}(\delta|xx)_w(x|\delta) \\ &\quad + \frac{l_w}{2}(\delta|xa)_w(x|\delta) + (\delta|aa)_w(x|\delta),\end{aligned} \tag{3.28}$$

$$\begin{aligned}(x|a\delta)_{tot} &= l_w(\delta|xx)_w(x|\delta)^2 - (\delta|xa)_w(x|\delta)^2 \\ &\quad + \frac{l_w}{2}(\delta|x\delta)_w(x|\delta) - (\delta|a\delta)_w(x|\delta),\end{aligned} \tag{3.29}$$

$$(x|bb)_{tot} = (x|bb)[1-(\delta|\delta)] + (\delta|bb)_w(x|\delta), \tag{3.30}$$

$$\begin{aligned}(x|\delta\delta)_{tot} &= (x|\delta\delta)[1-(\delta|\delta)] + (\delta|xx)_w(x|\delta)^3 \\ &\quad + (\delta|x\delta)_w(x|\delta)^2 + (\delta|\delta\delta)_w(x|\delta).\end{aligned} \tag{3.31}$$

There are four aberrations that appear in these equations that can be controlled, namely, $(x|aa)$, $(x|bb)$, $(x|\delta\delta)$, and $(\delta|xx)_w$. The first three are determined only

by the magnetic optics in the separtor. The last, $(\delta|xx)_w$, is controlled by shaping the wedge to have a particular surface curvature. Solving Eqns 3.28-3.31 for these aberrations we get:

$$(x|aa) = \frac{1}{(\delta|x)_w}\left[\frac{l_w}{4}(\delta|xa)_w + \frac{l_w^2}{8(x|\delta)}(\delta|x\delta)_w - \frac{l_w}{4(x|\delta)}(\delta|a\delta)_w - (\delta|aa)_w\right], \tag{3.32}$$

$$(x|bb) = -\frac{(\delta|bb)_w}{(\delta|x)_w}, \tag{3.33}$$

$$(x|\delta\delta) = \frac{1}{(\delta|x)_w}\left[\frac{(x|\delta)^2}{l_w}(\delta|xa)_w - \frac{(x|\delta)}{2}(\delta|x\delta)_w - \frac{(x|\delta)}{l_w}(\delta|a\delta)_w - (\delta|\delta\delta)_w\right], \tag{3.34}$$

$$(\delta|xx)_w = \frac{(\delta|xa)_w}{l_w} - \frac{(\delta|x\delta)_w}{2(x|\delta)} + \frac{(\delta|a\delta)_w}{l_w(x|\delta)}. \tag{3.35}$$

If Eqns 3.32-3.35 are satisfied, then all aberrations will vanish giving $(\delta|aa)_{tot} = (\delta|a\delta)_{tot} = (\delta|bb)_{tot} = (\delta|\delta\delta)_{tot} = 0$. Therefore, the separator can be made to be free of aberrations up to second order with the wedge in place for an initial point-like beam. However, it is not always true that these equations have a unique solution. In addition to this fact, if it does have a solution it would not be the same for every beam-material combination. In the case of Eqn 3.35, changing the curvature will change $(\delta|xx)_w$, but it will also change $(\delta|xa)_w$. In order to satisfy Eqn 3.34, additional multipoles would be required. If there is no exact solution,

numerical optimization can be employed to minimize the aberrations as much as possible. The same numerical optimization procedures can be extended to higher orders of computation.

3.7. Numerical Computations Involving Transfer Map of Energy Absorber

The nuclear physics community has devoted much energy in the development of computer codes that are accurately able to predict the energy loss of heavy-ions in matter. One of these codes is the program ATIMA [**25**]. This code uses spline interpolations to compute the energy loss and energy and angular straggling for every projectile and energy absorber material combination. The nature of the polynomial interpolations allows the evaluation of energy-loss functions easy to implement in differential algebra (DA), which is optimal for COSY. From within COSY, Eqn 3.36 is used to find the final energy of a particle after going through material of thickness T:

$$range(E_i) - range(E_f) - T = 0. \tag{3.36}$$

This function is solved implicitly within COSY, where $range(E)$ is returned by ATIMA. However this is not yet in DA form. In order to cast it into this form we must have the DA evaluation of the range function and also the effective thickness of material that is seen by each particle. The thickness depends on the length and shape of the absorber and the initial conditions of each particle. If the entrance

and exit surfaces of the wedge are described by two polynomials, then DA allows for the projection of the trajectory of an arbitrary particle onto these surfaces and calculation of the distance between these points giving the thickness T. Also the explicit dependence on the particle's initial conditions is kept. A more detailed explanation can be found in [**30**]. This formulation is given by

$$range[E_{i,0}(1+\delta_i)] - range[E_{f,0}(1+\delta_f)] - T(\vec{z}_i) = 0, \tag{3.37}$$

where $E_{i,0}$ and $E_{f,0}$ are the initial and final energies of the reference particle. δ gives the energy deviation from the reference particle. This is a complicated nonlinear and multivariable function that is of the form $f(\vec{z}_i, \delta_f) = 0$, which must be solved for δ_f. Assume that $\vec{z}_i$, the initial coordinates, which also can contain parameters like mass and charge, is n-dimensional. Introduce the n-dimensional identity operator I_n. If I_n.and f are combined, we obtain an $n+1$-dimensional dimentional operator that can be regarded as a map, $N_{n+1} = (I_n, f)$. This gives:

$$N_{n+1}(\vec{z}_i, \delta_f) = (\vec{z}_i, 0). \tag{3.38}$$

By construction, N_{n+1} is origin preserving and has a nonvanishing Jacobian determinant at the origin, and hence DA methods can be used within COSY for the explicit inversion to arbitrary order. The following is obtained:

$$(\vec{z}_i, \delta_f) = N_{n+1}^{-1}(\vec{z}_i, 0) \tag{3.39}$$

This directly gives the energy component of the wedge map:

$$\delta_f = [N_{n+1}^{-1}(\vec{z}_i, 0)]_{(n+1)th\ component}. \tag{3.40}$$

Again, the other components of the map are the same as a drift of the same length as the thickness of the wedge that the reference particle sees, so the whole wedge map is known at this point. It should be known that a similar procedure could be used to calculate the time of flight by spline interpolation. Also, if the equations of motion within the wedge are known, a DA integration would allow for wedge map computation from first principles.

3.8. Numerical Results of Optical Effects of Energy Absorbers

Here we use the theory described in the previous section to numerically calculate the effects of integrating the wedge into the fragment separator. There are several effects due the introduction of a uniformly shaped wedge with zero angle. One linear effect of the absorber is the induced energy dispersion, $(x|\delta)$, at the end of the system. With increasing absorber thickness, the dispersion grows monotonically. (Figure 3.8) This is directly correlated with the beam size at the end of

the separator. While there is not a great dependence on energy, the dispersion is more for lower energies.

The magnification of the fragment separator is unity without the wedge. With the introduction of the wedge, the magnification is always greater than one. As the thickness of the wedge is increased, the magnification increases. This increase of the linear matrix element $(x|x)$ is shown in Figure 3.9 for beam energies of 200 and 400 MeV/u. The magnification increase is great, almost doubling for a wedge that has a thickness of 50% of the range of the beam.

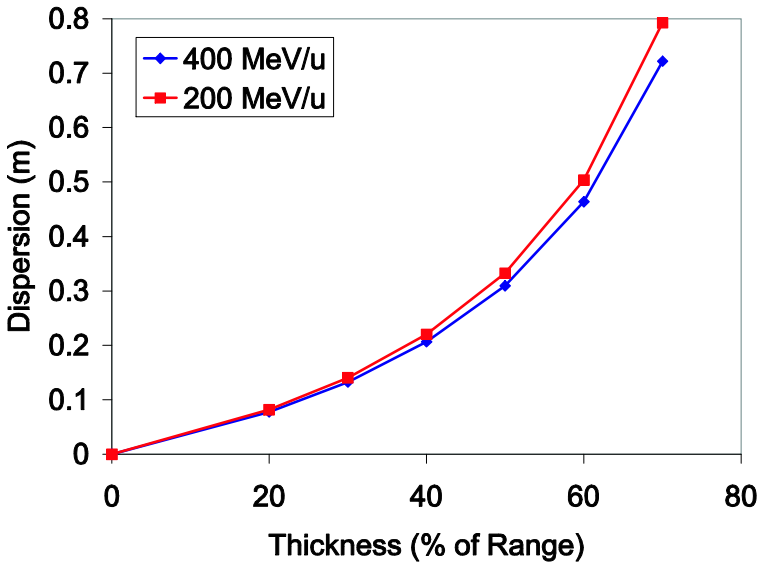

Figure 3.8. If the wedge is not shaped (uniform), then dispersion is introduced at the no-wedge achromatic image.

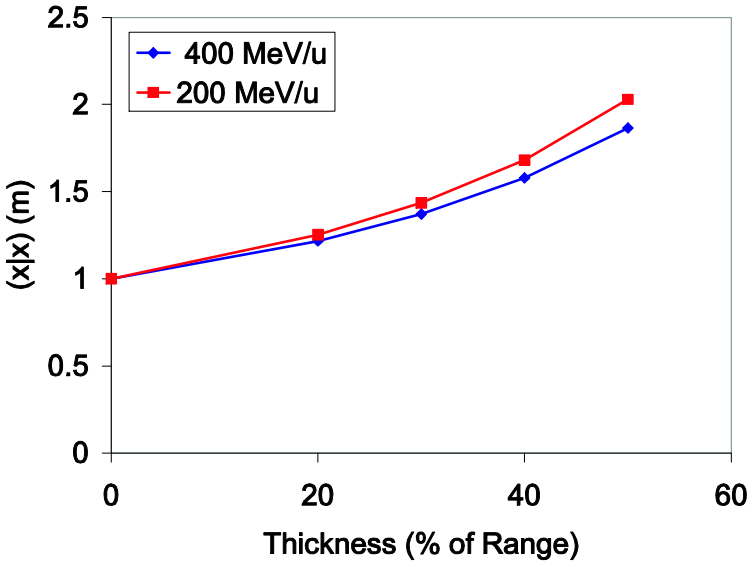

Figure 3.9. Magnification for a ^{132}Sn beam at two different energies as a function of wedge thickness.

The nonlinear effects of the wedge are quantified by looking at the values of the aberrations. The fragment separator is designed to be aberration-free to third order, so any aberrations that exist are directly due to the wedge. The largest aberrations that are induced depend on the initial angular and energy divergence of the beam as it emerges from the production target. The horizontal angular divergence is most important since the separation plane is in the horizontal direction. At both second and third order there are aberrations that result from the introduction of the wedge. These are shown in Figure 3.10.

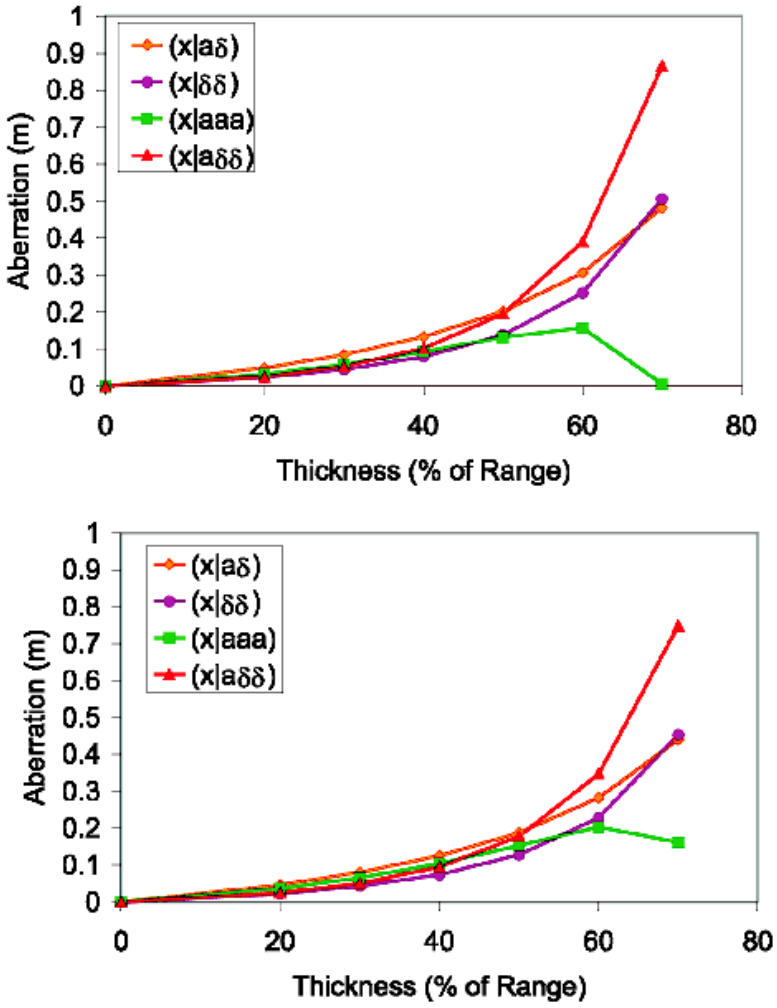

Figure 3.10. Large second- and third-order aberrations are induced at the no-wedge achromatic image for a ^{132}Sn beam at 200 MeV/u (above) and 400 MeV/u (below).

The initial values of the beam in all plots can be assumed to be: 1 mm spot sizes horizontally and vertically, ± 50 $mrad$ angular divergence in x and y, and $\pm 9\%$ momentum spread for the fission product ^{132}Sn. The magnitude of most

of these aberrations increase with wedge thickness. These aberrations are most dramatic in the case of fission since the initial a and δ are large. In a fragmentation case, these aberrations would not be quite as large as shown.

The sizes of the aberrations shown are extremely large, rendering the fragment separator useless for the most interesting rare isotopes, which are often fission products having large initial angular and energy divergence. To function in a high-performance mode, the separator must have aberrations that are no larger than a millimeter. With aberrations any larger, the resolution of the separator is greatly impeded, causing the overlapping of isotopes in real space, leading to the degradation of the separation purity.

Once the aberrations are realized, it is necessary to reduce them as much as possible by shaping the wedge. This is done by satisfying Eqn 3.21. To first order, the angle is the necessary parameter to fit. This is done within COSY [**31**]. Numerically, the matrix element $(x|\delta)$ is minimized. Once this is accomplished, the goal is to find how this angle depends on the thickness of the wedge and the energy of the beam. Figure 3.11 shows the optimal angle for three wedge thicknesses: 30, 50, and 70% of the range as a function of the energy of a ^{100}Sn beam. This dependence is essentially linear and increases with energy for all thicknesses. A thick wedge will require a larger angle in order to meet the criterion specified by Eqn 3.21. The same result applies to a ^{132}Sn beam, although, since it is heavier it requires slightly larger angles.

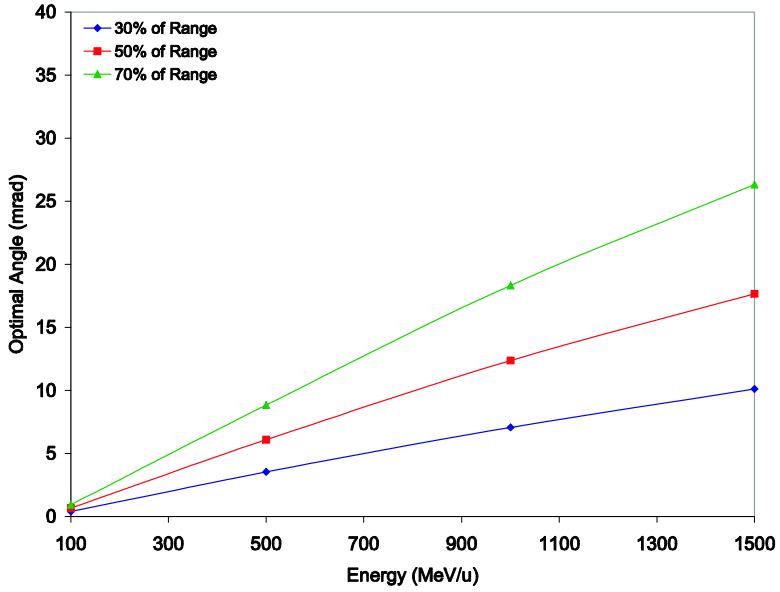

Figure 3.11. Optimal angle needed to maintain linear achromaticity for the case of a ^{100}Sn beam at various energies and three different wedge thicknesses.

Also shown (Figure 3.12) for a ^{132}Sn beam of two energies (200 and 400 MeV/u) is the angle as a function of the wedge thickness. This illustrates the fact that at lower energies, a smaller angle is needed to achieve achromaticity. Also, the slope of the line is different in the case of different energies. At a higher energy (400 MeV/u) the angle needed increases much more rapidly as a function of wedge thickness. There is a definite dependence on the Z of the primary beam on the angle needed. Figure 3.13 shows the angle as a function of the primary beam's Z value for two different types of wedge material, Al and Ta. For this comparison, the energy is 200 MeV/u in both cases. The dependence on Z is much greater for

low-Z isotope beams. These beams require large wedge angles. It should also be noted the lighter wedge material (Al) also requires a larger angle. This is because the energy lost per thickness is less than for Ta. The choice of wedge material is generally dictated by the types of nuclear processes that are happening in the wedge, i.e., fragmentation, of the beam, which produces contaminants, and energy and angular straggling.

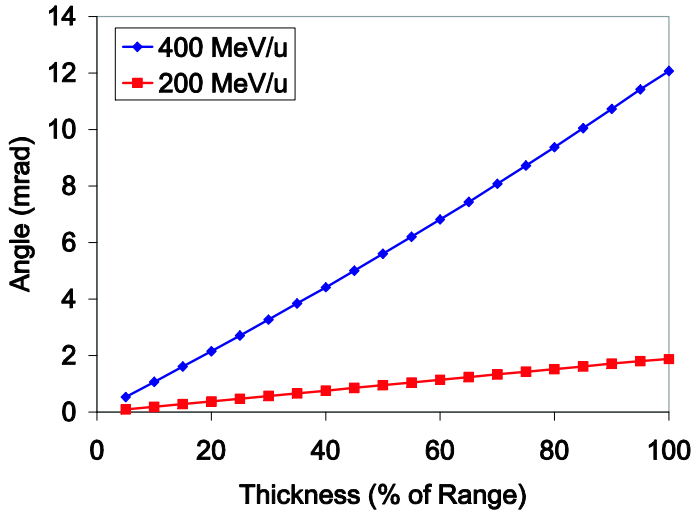

Figure 3.12. Optimal angle needed to maintain linear achromaticity for the case of a ^{132}Sn beam at various wedge thicknesses and two different energies.

Once the angle is found, the wedge is shaped accordingly and the higher order aberrations which are left need to be minimized. This is done by first looking at what can be done with the magnetic optics. The fragment separator has four

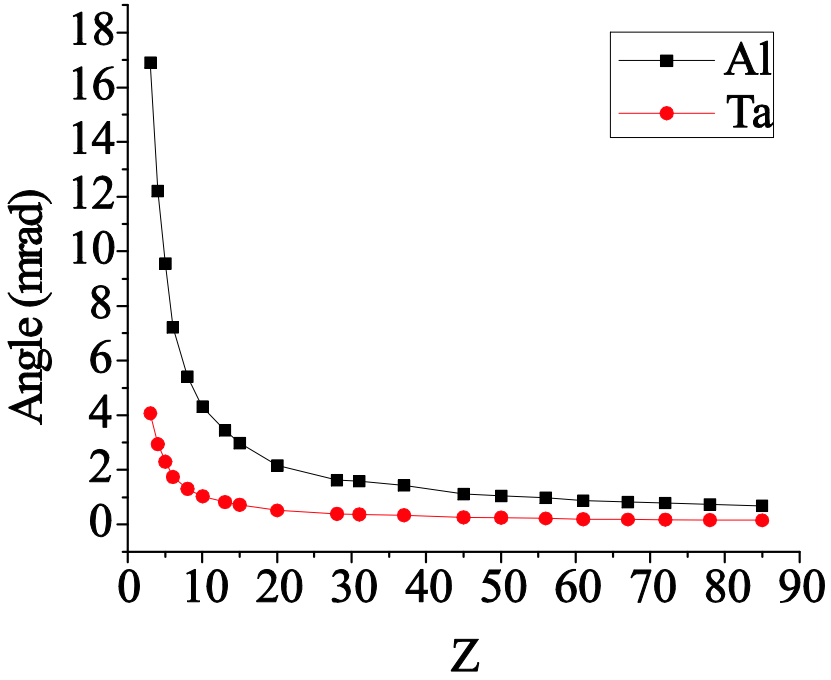

Figure 3.13. Optimal angle needed to maintain linear achromaticity for various beams of 200 MeV/u energy as a function of Z and two different wedge materials of 30% range thickness in all cases.

multipoles before the wedge and four after. These multipoles are superimposed having quadrupole, sextupole, and octupole terms. The quadrupoles and sextupoles are in a double-mirror symmetric arrangement and have four independent strengths. The octupoles are single-mirror symmetric and have eight independent strengths. Each of these strengths can be considered a "knob" in the system that can be used to optimally tune the separator. Once this is done, the only other knobs left are the curvature of the wedge at second order, and a cubic surface term at third order. After the magnet strengths are set, the curvature and cubic terms of the wedge are found by achieving nonlinear achromaticity, which, in practice,

means minimizing the aberrations $(x|\delta\delta)_{tot}$ and $(x|\delta\delta\delta)_{tot}$. The behavior of the high-order wedge coefficients is very similar to that of the wedge angle. Figures 3.14-3.16 highlight these values as a function of energy, wedge thickness, and Z of the beam.

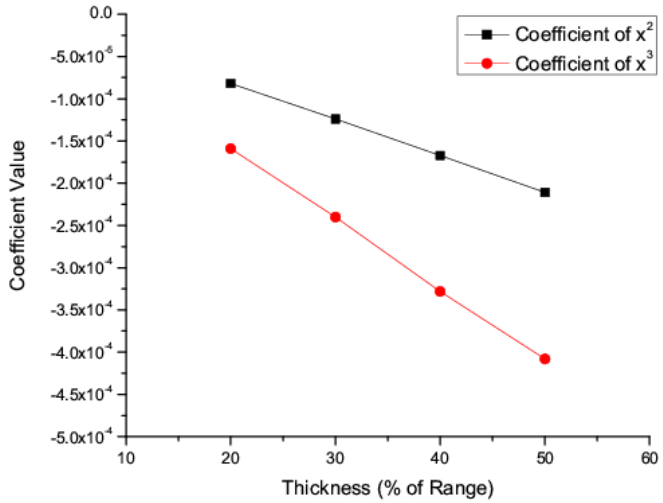

Figure 3.14. Second- and third-order wedge shape coefficients required to minimize aberrations in the system for a ^{132}Sn beam at 200 MeV/u.

After all of these steps have been taken to achieve the optimal separator, there are still a few small, but nonzero aberrations which remain. These aberrations result mainly from particles seeing different wedge thicknesses as a function of the incoming angles and the associated additional energy loss. These aberrations get worse as the wedge thickness is increased. The top three aberrations are

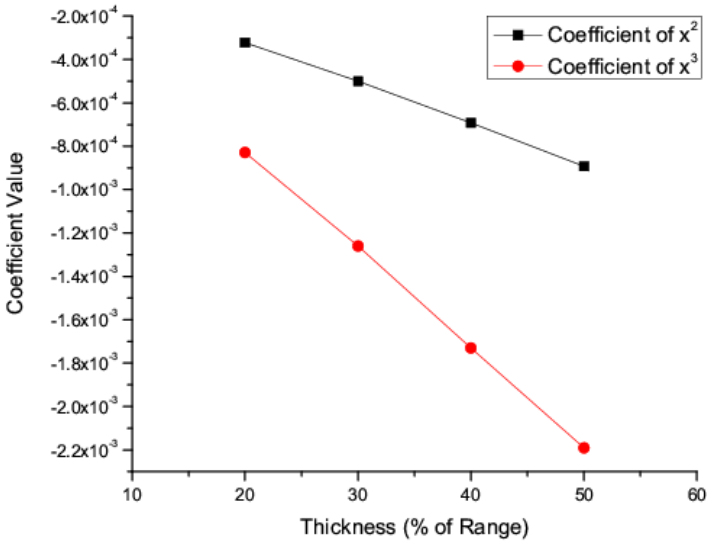

Figure 3.15. Second- and third-order wedge shape coefficients required to minimize aberrations in the system for a ^{132}Sn beam at 400 MeV/u.

$(x|xa)$, $(x|aaa)$, and $(x|a\delta\delta)$, and their behavior as a function of wedge thickness is highlighted in Figures 3.17 and 3.18.

3.9. Resolutions

When separating rare isotopes with a fragment separator, one of the most important features of the system is the resolution. In the case of separating exotic nuclei with a variety of masses and charge states, there are two types of resolution that are important, namely mass and charge. The mass resolution should be known for a fixed charge state and charge resolution for a fixed mass.

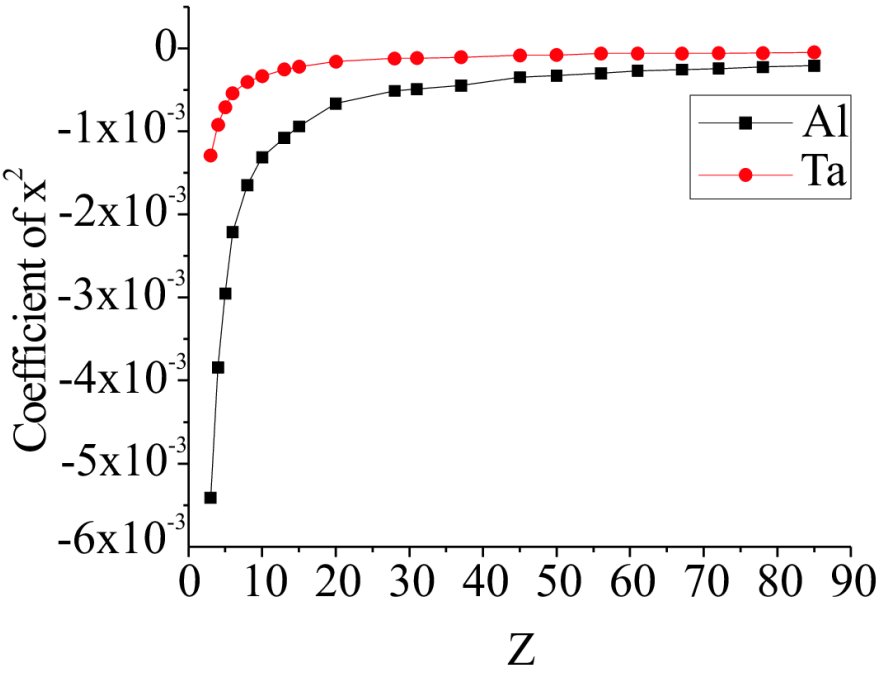

Figure 3.16. Scaling of the wedge curvature for the 200 MeV/u ^{132}Sn case as a function of Z for two different wedge materials with thickness equal to 30% of the range.

If both vary, then the best way to show the resolution is to plot a cut in the mass-charge plane, which is a line on which the selected mass and charge states that are transmitted lie.

The resolving power may be computed to any order, the linear case giving the "best" resolution since no aberrations are taken into consideration. At higher orders the image size at the end of the system increases due to aberrations and lowers the resolution in both mass and charge.

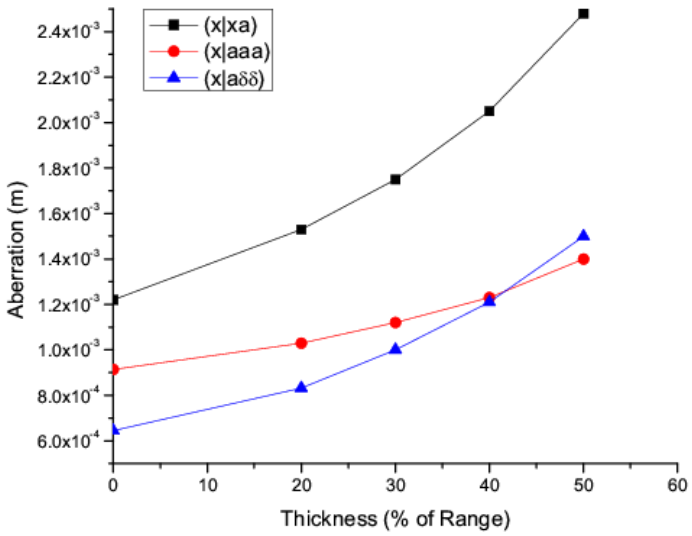

Figure 3.17. Largest remaining aberrations in the system after magnetic multipole correction and wedge shaping performed to third order with a ^{132}Sn beam at 200 MeV/u.

Analytically, the linear resolving power may be computed using the transfer matrix for the entire fragment separator. The mass $(_m)$ and charge $(_q)$ resolutions are computed by:

$$R_{m,q} = \left| \frac{(x|\delta_{m,q})_{total}}{2x_0(x|x)_{total}} \right| = \left| \frac{(x|\delta)(\delta|\delta_{m,q}) + (x|\delta_{m,q})(1-(\delta|\delta)_w)}{2x_0(\delta|\delta)_w} \right|, \tag{3.41}$$

where $(x|\delta_{m,q})$ are the mass and charge dispersions, respectively, and $(x|x)_{total}$ is the magnification of the whole system. $2x_0$ is the initial beam size in x. To maximize the resolution, one must maximize this equation. It is not obvious,

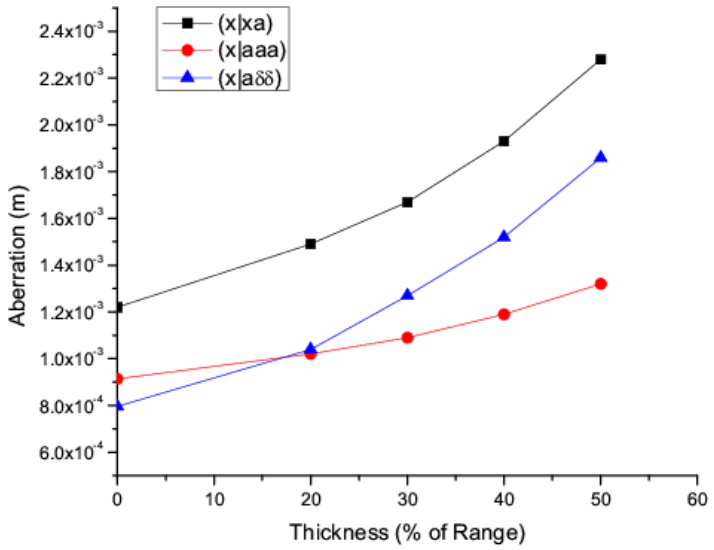

Figure 3.18. Largest remaining aberrations in the system after magnetic multipole correction and wedge shaping performed to third order with a ^{132}Sn beam at 400 MeV/u.

however, which wedge thickness gives a maximum resolution because all wedge map elements change with the wedge thickness. For some wedge thicknesses in some energy regimes it happens that the charge resolution vanishes. This not the case for the mass resolution, though.

Figure 3.19 shows the mass resolution as a function of the wedge thickness for a ^{132}Sn beam at 200 MeV/u. To first order, the mass resolution is nearly linear, increasing with wedge thickness. At second and third order, aberrations lower the resolution overall. At 400 MeV/u (Figure 3.20) the data appear almost identical with only slight differences in the linear and nonlinear resolutions.

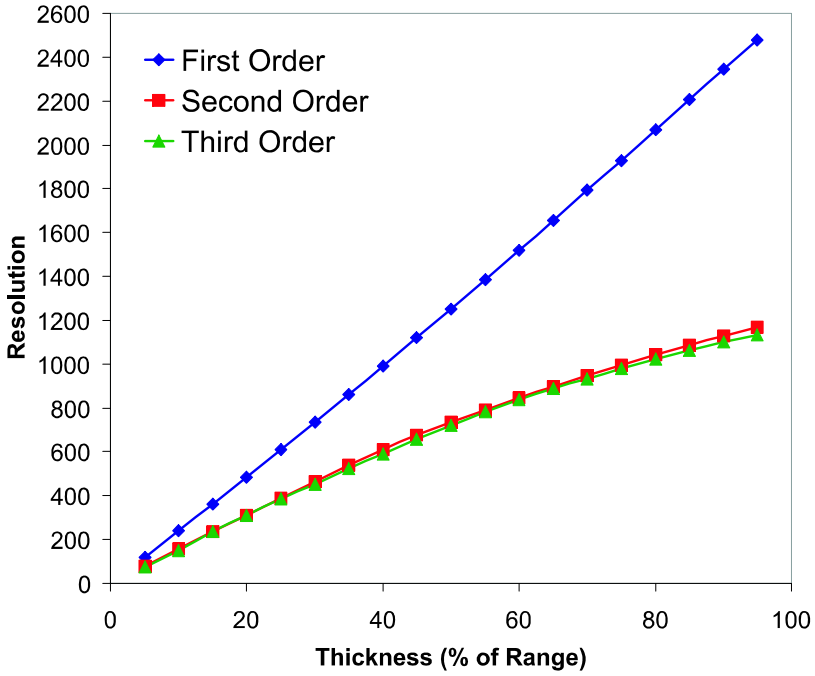

Figure 3.19. Mass resolving powers for a 200 MeV/u ^{132}Sn beam and Al wedge as a function of wedge thickness evaluated at different map orders.

There are overall greater differences in the charge resolution with respect to energy compared to the mass resolution. At 200 MeV/u, the resolution increases linearly with wedge thickness. When the energy of the beam is increased to 400 MeV/u, the increase in resolution with wedge thickness is slower. If nonlinear effects are taken into account, the resolution is almost double in the 400 MeV/u case for some wedge thicknesses.

In order to look at how the resolution varies with energy, the resolution was probed for three wedge thicknesses (30, 45, and 60% of the range) and energies from 100 to 1500 MeV/u. The mass resolution as a function of energy is decreasing

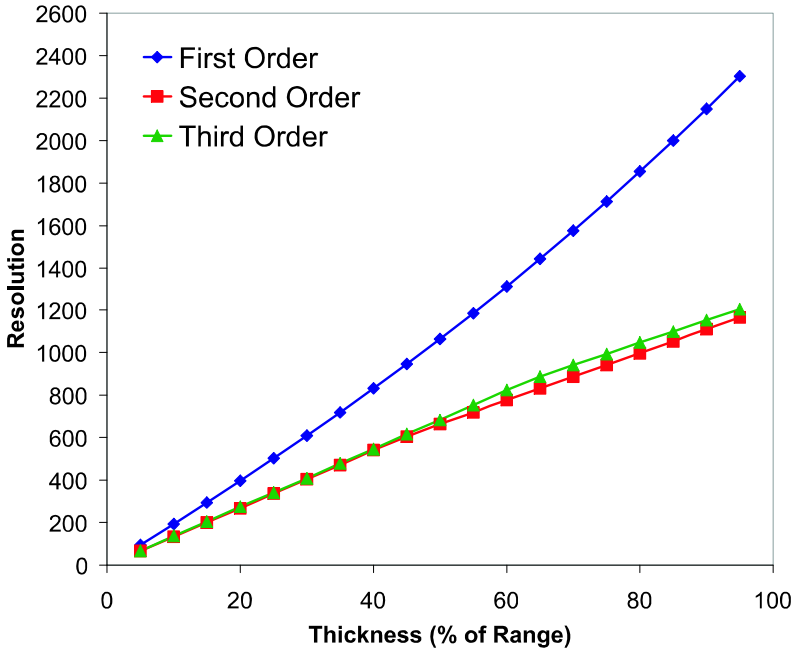

Figure 3.20. Mass resolving powers for a 400 MeV/u ^{132}Sn beam and Al wedge as a function of wedge thickness evaluated at different map orders.

as energy increases, as shown in Figure 3.21 The variation in resolution for different wedge thicknesses is less at higher energies than it is for low energies. The charge resolution has a different behavior altogether in the specified energy regime. (Figure 3.22) At low energy the charge resolution is large but decreases as energy increases up to around 600 MeV/u for large thickness and at 700 MeV/u for small thickness. At these points, the charge resolution almost vanishes completely. As the energy gets higher the resolution begins to increase again.

This "vanishing" phenomenon can be described in the following way. The explanation of the minimum resolution depends on the nature of the energy-loss

dependence on the parameters of the particles. When the wedge is not in the system, it is achromatic and the resolution is zero. So, any two particles with different rigidities due to a different charge state but same initial position will end up at the same final position at the achromatic image point. When the wedge is introduced and is shaped to keep the image achromatic, the relative rigidity dispersion of the particles changes after traversing the wedge, introducing a net dispersion at the end of the system. At certain energies and wedge thicknesses, the competing effects can cancel each other out. In this case, the higher charge states are less rigid and bend more. These particles will see smaller wedge thicknesses than lower charge states. Also, the charge dependence of the energy loss implies that the higher charge state has a larger energy loss rate, canceling the fact that the particle goes through a thinner portion of the wedge. The combined effect is that in some cases the particles will not change their relative rigidities after exiting the wedge, which will not induce a net charge dispersion at the end of the system.

If both the mass and charge are allowed to vary, then, to first order, the cut is a line in the $\delta_m\delta_q$-plane with slope given by:

$$\text{slope} = \frac{(\delta|\delta_m)_w + (x|\delta_m)(\delta|x)_w}{(\delta|\delta_q)_w + (x|\delta_q)(\delta|x)_w}. \tag{3.42}$$

If nonlinearities are taken into account with a map computed to seventh order, then the separation cut in the δ_m, δ_q plane for the ^{132}Sn-400 MeV/u, 45% range

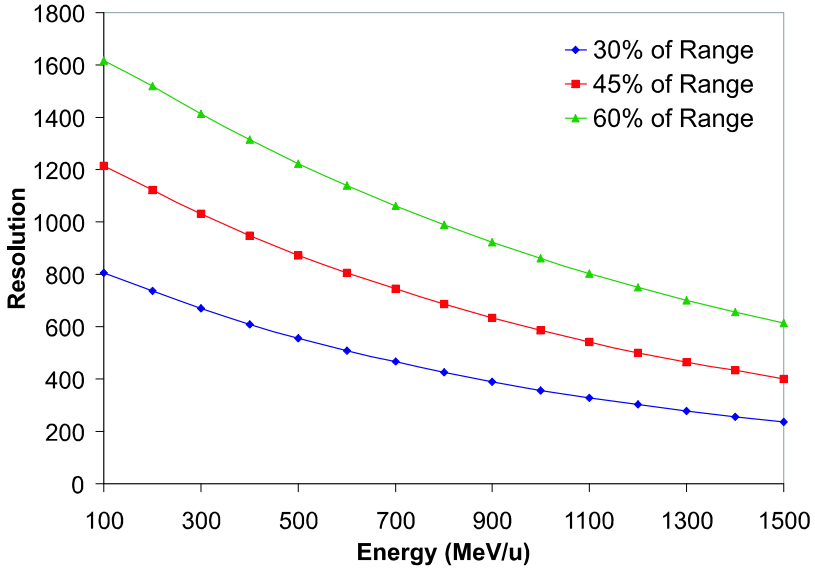

Figure 3.21. Mass linear resolving power as a function of energy for three different wedge thicknesses.

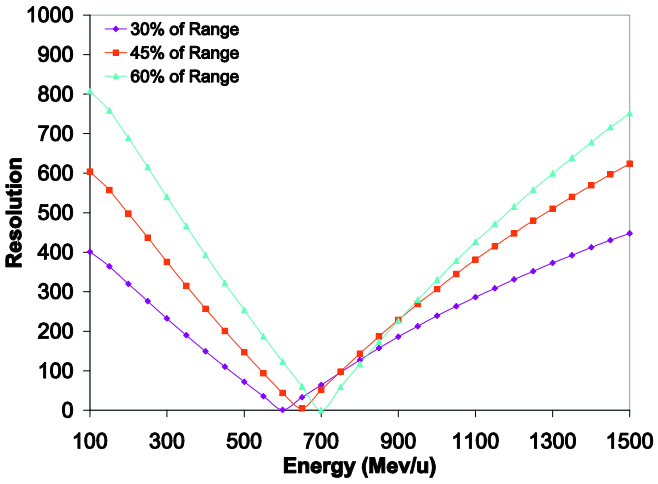

Figure 3.22. Charge linear resolving power as a function of energy for three different wedge thicknesses.

wedge thickness case is given by Figure 3.23. For this particular case the cut is still basically a line. However, this may not be the case for other isotope and energy combinations. At higher orders this line could be a curve or have other higher order features. The slope of the separation cut line depends on the wedge material and thickness as well as the beam energy. Figures 3.24 and 3.25 show the slope of the separation cut line as a function of wedge thickness. The data are given for three different wedge materials: carbon, lead, and aluminum (low Z, high Z, typical material) at four different energies: 100, 200, 400, and 1500 MeV/u. From these data it is obvious that the energy of the beam plays a huge role in determining the slope of the line at high energies. At lower energies the differences in slope are not as dramatic To a lesser extent the wedge materials influence the slope, but it is still advantageous in many instances to exploit the differences. The thickness of the wedge has some influence as well for a given energy and material. A thick wedge can also be used to cause a greater energy difference between the first and second stages.

All of these facts can be used together in the design of an experiment. For example, when implementing a two-stage separator, the separation cut lines from each separation stage would intersect at right angles to give perfect separation. From the first stage, every isotope along the separation cut line would be selected. In the second stage the separation cut would contain all the isotopes that lie along the current line that were transmitted from the first stage. If the two lines are of the same slope, the second stage is useless since it selects the same isotopes as

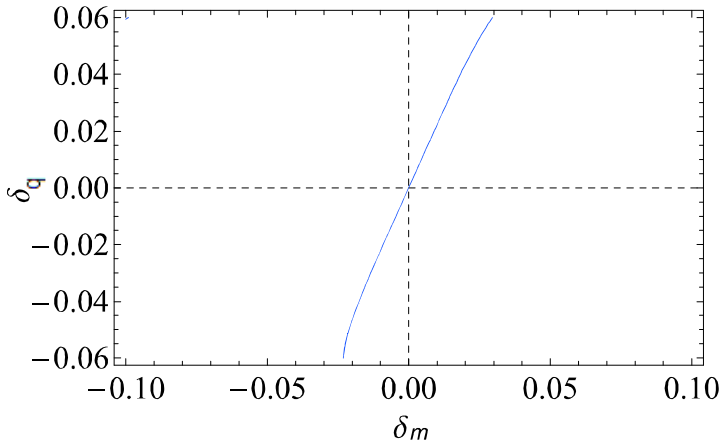

Figure 3.23. Separation cut, including nonlinearities, up to $7th$ order for a 200 MeV/u ^{132}Sn beam.

the first stage. If they are at right angles to one another, the two-stage setup will select only one rigidity. Of course, in practice there are no lines, but "bands" which contain many separation cut lines of slightly different rigidities. The size of these bands is determined by the slit settings used, i.e., the larger the slit the wider the band and the greater number of rigidities selected. The slit settings chosen for the system will have a direct impact on the separation purity.

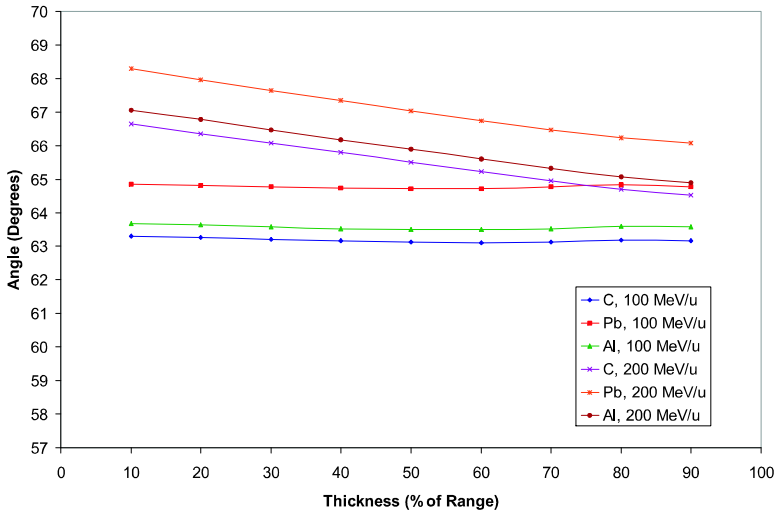

Figure 3.24. Separation cut angles for a ^{132}Sn beam with energies 100 MeV/u and 200 MeV/u and three wedge materials.

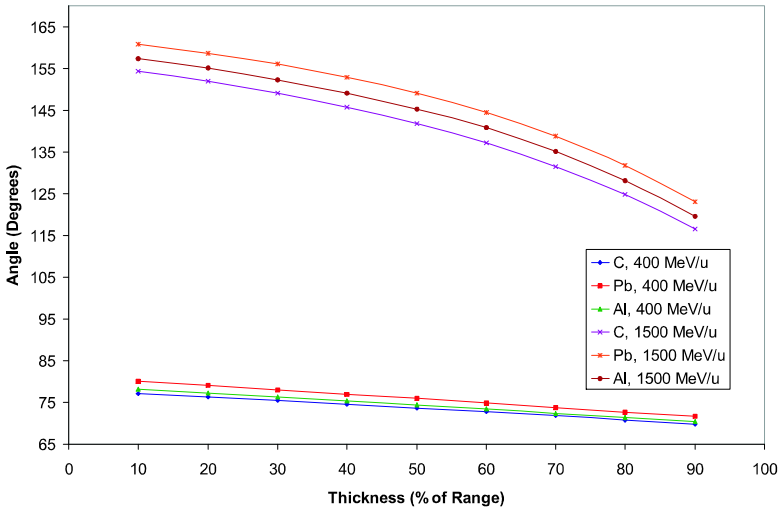

Figure 3.25. Separation cut angles for a ^{132}Sn beam with energies 400 MeV/u and 1500 MeV/u and three wedge materials.

CHAPTER 4

Monte Carlo Results

There are definite limitations to running the code in "map mode," meaning that only maps are computed for the optical elements and then composed and applied to the beam's initial coordinates in order to get the final coordinates. This method does not take into account either fragmentation or fission in the beam in matter or the stochastic effects such as energy and angular straggling of the beam. These effects are extremely important in the modeling of the beam and must be accurately computed. This can only be done when the code is run in "Monte Carlo mode."

The performance of the fragment separator can be described quantitatively by two values, namely the separation purity and transmission. These quantities are best calculated with the code in Monte Carlo mode. The separation purity is key to showing how much background contamination (isotopes other than the selected isotop) exists at the end of a separation. The transmission indicates the ratio of the number of particles of a particular rare isotope at the end of a separation stage to the number that is formed in the target. In some cases the separation purity may be good but the transmission is bad or vice versa. The two quantities must be evaluated together to effectively evaluate the performance of the separator.

4.1. Transmissions

The transmission of various isotopes in the fragment separator can vary dramatically, depending on the isotope the fragment separator is tuned for as well as how much absorber material is in the system. The dependence of the transmission on the separated isotope is mainly due to the mechanism that produced it. A particle is "lost" if its trajectory takes it beyond the magnet apertures or if it is stopped in absorber material. Fragmentation products are generally well within the limits of the acceptance of the separator and losses are minimal. Fission products are generally much trickier to keep within the limits of the separator. However, it is possible to find an optimal setting for target and absorber thicknesses that will maximize the transmission for a particular experiment.

Due to the challenges of fission products in particular, a comprehensive transmission study was conducted for the fission product ^{132}Sn. This isotope was chosen for its importance to the nuclear physics community and the fact that a beam of ^{132}Sn has a large emittance and, hence, is one of the most difficult to capture. This study was conducted by running the Monte Carlo version of the code with the wedge shaped to third order to maintain achromaticity. The slits were set at the magnet apertures in order to "capture" the particles that would be lost in a real-world experiment using the fragment separator. By this method, the number of particles lost at each location in the separator can be quantified and the coordinates of these particles saved for later analysis. This method has a

secondary advantage. Besides determining where the ^{132}Sn is lost, it is also easy to see where the primary beam, ^{238}U, is lost. This is necessary information for determining the best location for a beam dump. The primary beam is radioactive and can contaminate the experimental apparatus if not dealt with properly. In addition, losses from the fragmentation of ^{132}Sn in the target and wedge are taken into account.

For this study, a 200 MeV/u ^{238}U beam is incident on a Li target of variable thickness. It fissions, producing ^{132}Sn among thousands of other isotopes. The thicknesses of the target and the first and second wedges of a two-stage separator are varied in increments of 10% of the range of ^{238}U in the target (Li) and ^{132}Sn in the two wedges (Al) for all thickness combinations between 10% and 60% of the range for the target thickness and 10% and 70% of the range for the wedges. The transmission of of ^{132}Sn after two separation stages is shown in Figures 4.1-4.3 for constant target thickness and varied wedge thicknesses. While it is obvious that with increasing material in the system the transmission decreases, from the plots of the transmission it can be seen that the transmission depends slightly more on the first wedge thickness than the second. This difference is more pronounced for small target thicknesses. When using this information to plan an experiment, the overall transmission must be coupled with the contaminating particles that may be produced in greater numbers for some target and wedge thicknesses.

The transmissions of isotopes produced by the four general reaction mechanisms (Table 4.1) were also calculated for a target thickness of 20% of the range of the

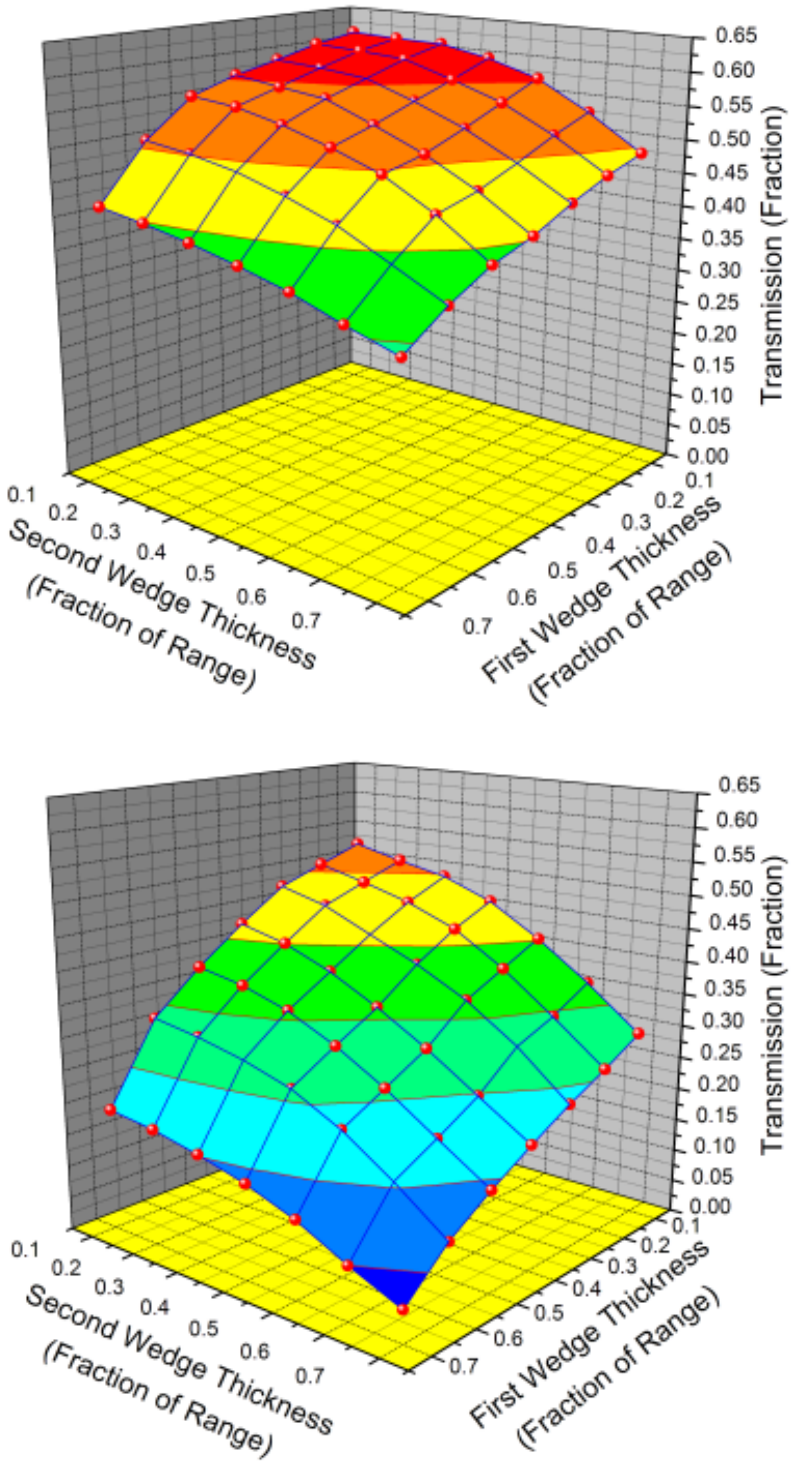

Figure 4.1. Transmission of ^{132}Sn after two separation stages as a function of wedge thicknesses for a Li target equal to 10% (top) and 20% (bottom) of the range for a 200 MeV/u ^{238}U beam.

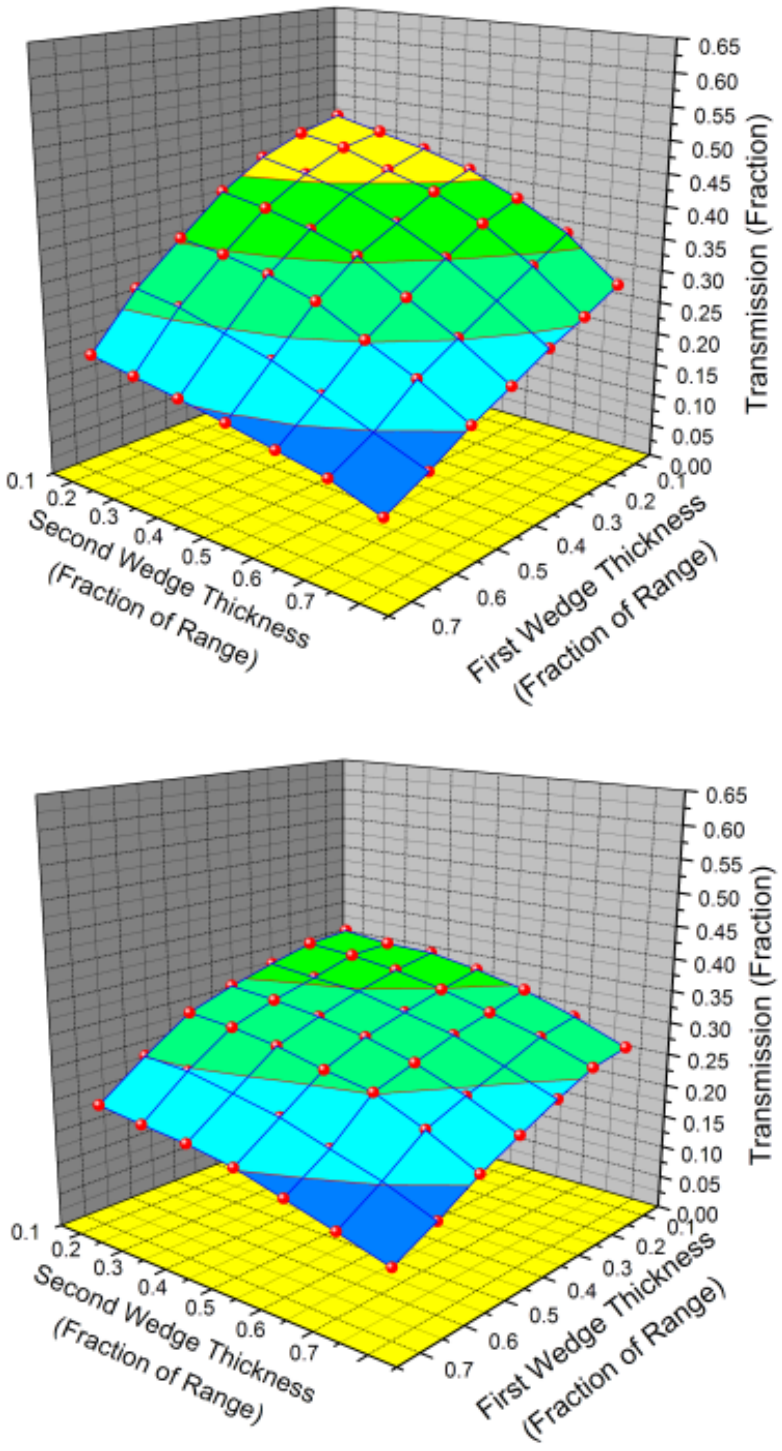

Figure 4.2. Transmission of ^{132}Sn after two separation stages as a function of wedge thicknesses for a Li target equal to 30% (top) and 40% (bottom) of the range for a 200 MeV/u ^{238}U beam.

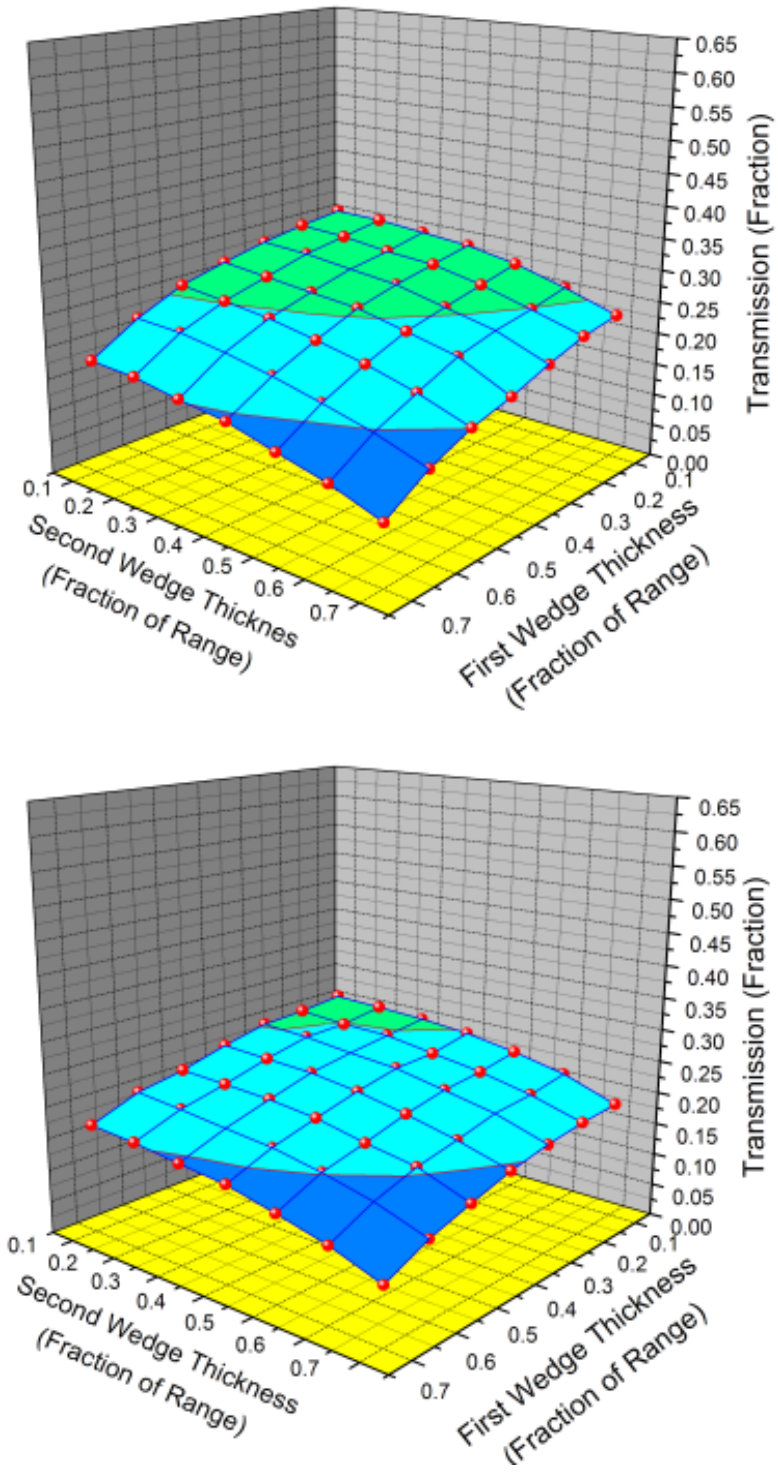

Figure 4.3. Transmission of ^{132}Sn after two separation stages as a function of wedge thicknesses for a Li target equal to 50% (top) and 60% (bottom) of the range for a 200 MeV/u ^{238}U beam.

Table 4.1. Transmission of various isotopes as a function of production mechanism.

Production Mechanism	Isotope	Transmission (%)
Light Fragmentation	^{14}Be	90.6
Heavy Fragmentation	^{100}Sn	91.0
Light Fission	^{78}Ni	21.5
Heavy Fission	^{132}Sn	42.9

primary beam in a Li target and wedge thicknesses of 30% of the range of the selected isotope beam energy in a two-stage separator. There is a great dependence of the transmission on the reaction mechanism which produces each isotope. The best transmission results from fragmentation, due to the low initial emittance of the rare isotope beam. The transmission is lower for fission products, as they are initially emitted from the target with large angular and energy spread. This causes the loss of the isotope since it travels beyond the apertures of the fragment separator.

4.1.1. Beam Dump

When charged particles pass through certain portions of the fragment separator such as the superconducting multipoles, there are dangers of radioactivity, overheating, and ultimately magnet failure. For this reason, it is necessary to prevent losses in magnets by placing a beam dump at the location where maximum particle losses occur. The vast majority of the particles that are incident on the beam dump are the primary beam.

Three test cases were run to determine where the greatest losses are along the fragment separator. These were the fission of a 200 MeV/u ^{238}U beam to produce ^{132}Sn, fragmentation of 245 MeV/u ^{124}Xe beam to produce ^{100}Sn, and fragmentation of a 305 MeV/u ^{18}O beam to produce ^{14}Be. Unfortunately, given the results of these three studies, there is no one optimal location to put a beam dump. Each of the three cases indicates a different location where the maximum losses occur. For the ^{132}Sn separation, the greatest losses were the ^{238}U beam at the second to last quadrupole of the first separation stage (Figure 4.4). The fragmentation cases had the greatest losses in the first half of the first stage. The ^{18}O beam used to produce ^{14}Be was lost in the middle of the first dipole (Figure 4.5). The ^{124}Xe beam to produce ^{100}Sn was lost just before the first absorber wedge (Figure 4.6). These results suggest that multiple beam dumps will be needed depending on the type of separation that is performed. If, however, only one location is possible, the best and easiest place to put the beam dump is just before the absorber in the first stage. This is because, under no circumstances can the primary beam hit the absorber wedge. The beam power for the FRIB is 400 kW. At this level, the primary beam would not only contaminate the wedge but destroy it due to thermal effects.

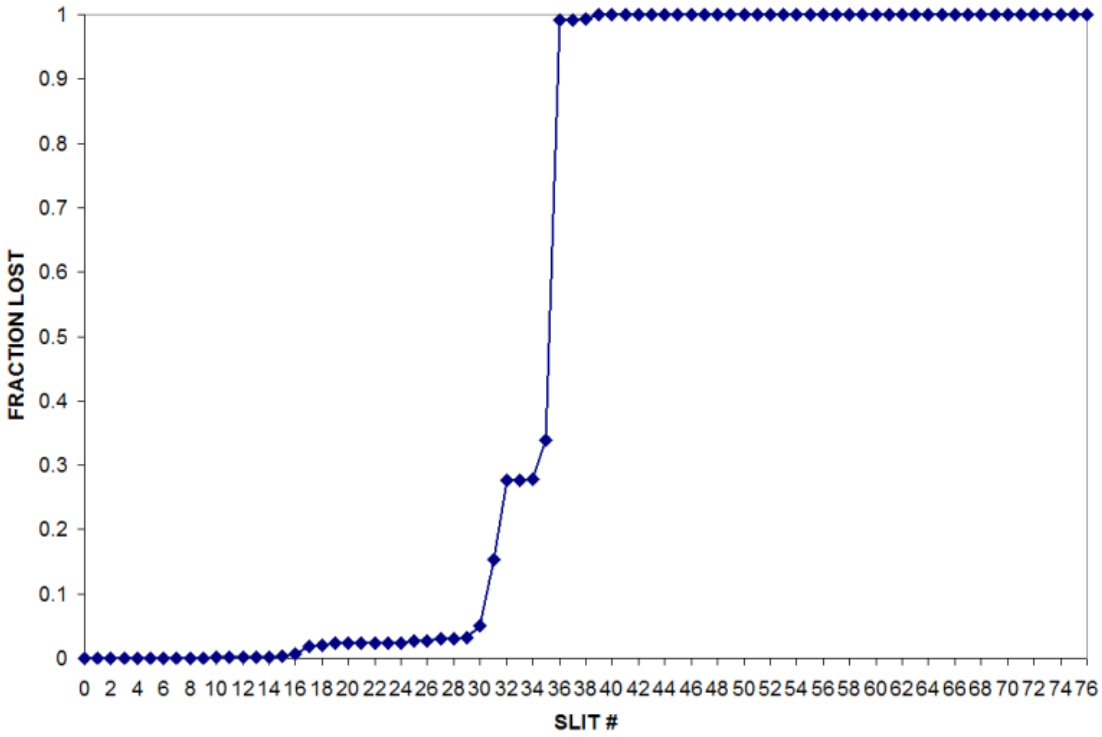

Figure 4.4. Transmission losses along the separator for the case of the separation of ^{132}Sn. Slit numbers 1-19 are within the optics of the first half of the first stage of the separator. The first wedge is located between Slit numbers 19 and 20. Slit numbers 20-38 are within the optics of the second half of the first stage. Slit numbers 39-57 are within the optics of the first half of the second stage. The second wedge is located between Slit numbers 57 and 58. Slit numbers 58-76 are within the optics of the second half of the second stage.

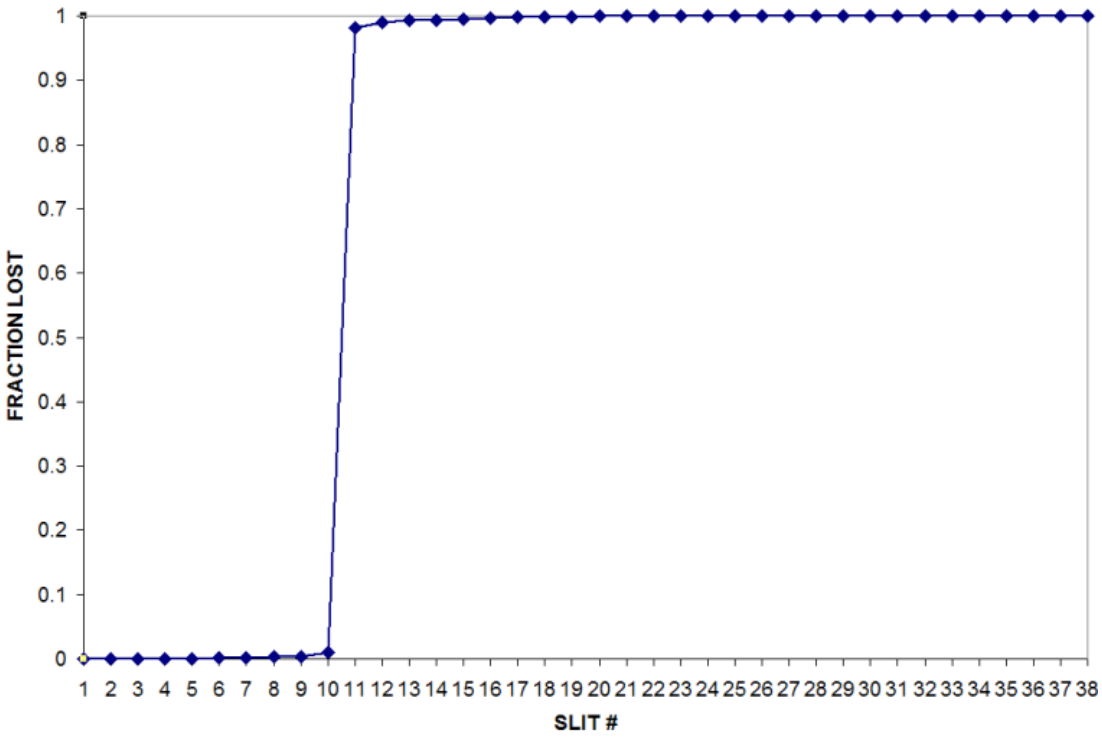

Figure 4.5. Transmission losses along the separator for the case of the separation of ^{14}Be. Slit numbers 1-19 are within the optics of the first half of the first stage of the separator. The first wedge is located between Slit numbers 19 and 20. Slit numbers 20-38 are within the optics of the second half of the first stage.

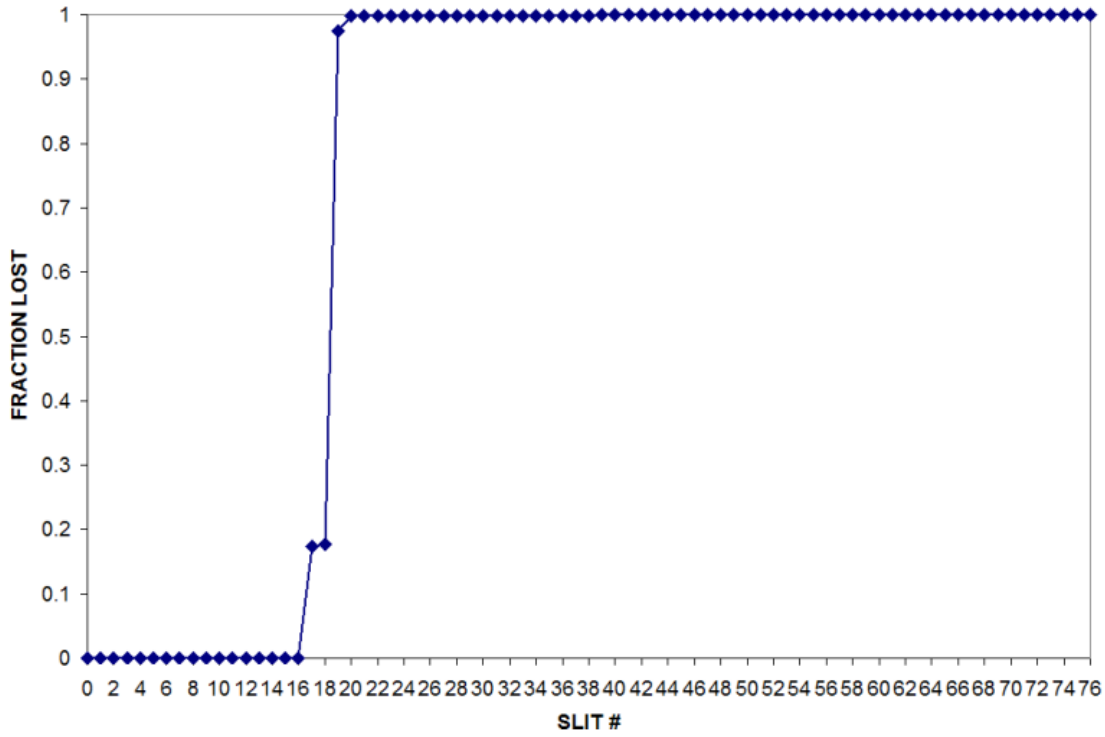

Figure 4.6. Transmission losses along the separator for the case of the separation of ^{100}Sn. Slit numbers 1-19 are within the optics of the first half of the first stage of the separator. The first wedge is located between Slit numbers 19 and 20. Slit numbers 20-38 are within the optics of the second half of the first stage. Slit numbers 39-57 are within the optics of the first half of the second stage. The second wedge is located between Slit numbers 57 and 58. Slit numbers 58-76 are within the optics of the second half of the second stage.

4.2. Separation purity

The separation purity is perhaps the most important quantity that describes the fragment separator since it describes the separator's ability to select one isotope from all others. The separation purity of the system is given by

$$\text{Separation Purity} = \frac{\text{Number of Particles of Selected Isotope}}{\text{Number of Particles (All Isotope Types)}}. \tag{4.1}$$

This quantity depends on many things which are not explicit in this expression. First, the optics of a fragment separator system must be optimal to focus the separted isotope in as small of a region in x as possible. The ability to do this differs according to the isotope and the reaction mechanism by which it is produced. The primary beam also plays a role in producing the background impurities (type and quantity) that exist. If the primary beam is of a low Z, the background impurities produced must have Z lower than this and the resulting impurities will only be within a small region of the $N-Z$ plane. If, however, a high Z beam such as uranium is used, the range of contaminating isotopes produced is vast. Also, a radioactive beam such as this will produce background that would not otherwise be seen with a fragmentation-only beam. The addition of fission as a production mechanism leads to an even broader range of isotopes produced and, in addition, these production rates are dependent on the energy of the primary beam.

There are four general reaction mechanisms that take place in the production target [**32**]. Each of these, because of the production mechanism and mass of the isotope to be separated, has different beam dynamics and background that either complicate or make the separation easier. These mechanisms represent the extremes of the dynamics in the separator. All other isotope production mechanisms fall between these extremes in beam dynamics. For each of these four reaction mechanisms, one isotope was selected to be studied in detail. Each is a rare isotope that is of interest to nuclear physicists that will be studied when a FRIB comes online. In these cases, the energy of the beam is limited by the parameters of the FRIB linear accelerator. The maximum energy that a primary beam attains is a ^{238}U primary beam at 200 MeV/u. Lighter primary beams can be accelerated to a higher energy (in MeV/u). The optimal target and wedge thicknesses in each case are computed using the program LISE++.[**33**] The optimization is done for a one-stage setup with the second stage having the same wedge thickness as the first in terms of fraction of range of the rare isotope beam. Also, since a thick wedge is used in the gas cell branch of the fragment separator, secondary fragmentations occur and alter the separation purity. The gas cell branch is a difficult problem because any contamination that is produced in the wedge can end up in the gas cell along with the separated isotope. There is no additional rigidity selection by a dipole after the monochromatic wedge. Only range selection in the He gas cell can be used for separation. All gas cell branch calculations are for a wedge that is 70% of the rare isotope's range in aluminum.

4.2.1. Light Fragmentation

^{14}Be is one isotope that is produced by light fragmentation. The primary beam is ^{18}O at 305 MeV/u that fragments on a 5000 mg/cm^2 lithium target. The wedge was 10,000 mg/cm^2 thick, which is 21% of the range of the rare isotope beam in aluminum. Of the rare isotopes used as test cases, ^{14}Be is the easiest to separate. Since it is of low Z, the number of background contaminants produced is small. Also, it has a relatively large cross-section. The separation purity after one stage is 100% so only one separation stage is needed. The transmission after one stage is 91%. The slit setting in x at the end of the first stage is -0.01 m to 0.015 m. Since the cross-section for ^{14}Be is high, there are no approximations needed to get statistically significant results. To produce this isotope, 20,000 primary beam particles were used with a weight factor of 2000 applied to the primary beam.

When the gas cell branch of the separator is added, the separation purity is slightly decreased due to fragmentation of ^{14}Be in the thick monochromatic wedge. There is only one contaminant that is produced, which is ^{11}Li. This brings the separation purity down to 96.77% in this case.

4.2.2. Heavy Fragmentation

^{100}Sn is produced by a 245 MeV/u ^{124}Xe primary beam. For the described studies, a 450 mg/cm^2 target and 700 mg/cm^2 wedge (44% of range) were used. The separation of ^{100}Sn should not be difficult if only the dynamics are considered.

A fragmentation product that is heavy emerges from the target with very small angular and energy divergence. For this reason, any aberrations at the end of one stage will be very small, which corresponds to a small beam spot. Since the beam is small at the end, the slit needed to capture the maximum number of ^{100}Sn should also be small. Unfortunately, there is another isotope, also a heavy fragmentation product that has almost the exact rigidity of ^{100}Sn, namely ^{99}In. This means that the two isotopes essentially are overlapping at the end of the separation stage. To add to the difficulties, ^{99}In has a much larger cross-section than ^{100}Sn by two orders of magnitude. So, while the dynamics of a ^{100}Sn beam alone would make for a good separation, the identical rigidities and large cross-section of the contaminant make it impossible to separate at the energies of the proposed FRIB. This case could be improved at higher energies because the separation cut angles after each separation stage could be rotated so that the intersection chooses mainly ^{100}Sn.

The first stage separation purity for ^{100}Sn is 7.73×10^{-7} (Figure 4.7). This corresponds to a slit setting in x of 0.006 m to 0.01 m. In order to rotate the separation cut angle as much as possible at the specified energy, a very thick wedge (80% of range) is used in the second separation stage. The separation purity and slit settings are 7.5% and 0.005 m to 0.028 m, respectively (Figure 4.8). While having a thick wedge in the second stage does not solve the separation problem entirely, it does improve the separation purity by one order of magnitude compared to the case where a thickness of 44% of the range in the second stage is used. The transmission is 40.5% after the first stage and 11.6% after the second.

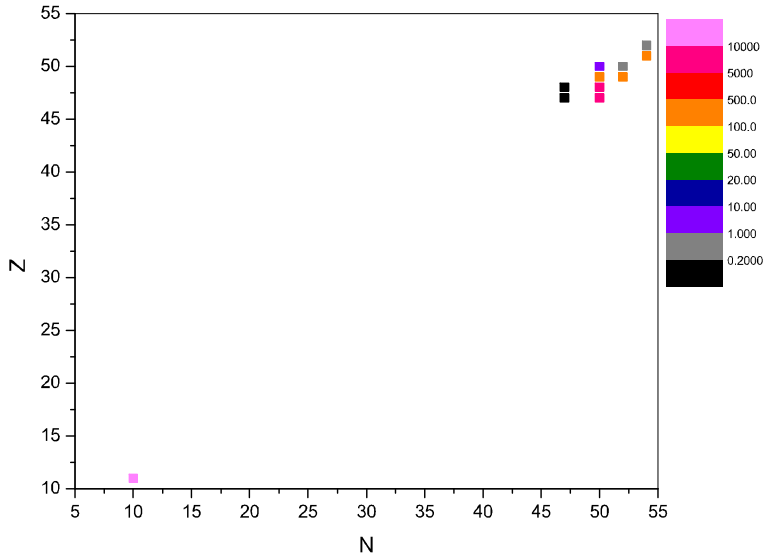

Figure 4.7. Distribution of isotopes that remain after one-stage separation of ^{100}Sn.

The separation purity is not good in the case of the gas cell branch, 1.48×10^{-5}%, mainly because a significant fraction of the ^{99}In is let through (Figure 4.9). This isotope fragments in the monochromatic wedge, and since there is only one and a half separation stages, this leads to much contamination at the end.

4.2.3. Light Fission

^{78}Ni is a light fission product that is produced by a 200 MeV/u ^{238}U primary beam. Due to the fact that ^{78}Ni is produced by fission and is light, it is very difficult to separate. In the optimized setup, a 125 mg/cm^2 Li target and 800 mg/cm^2 Al wedge were used. Despite the optimization performed to increase the separation purity, it is only a dismal 2.79×10^{-4}% after the first separation stage

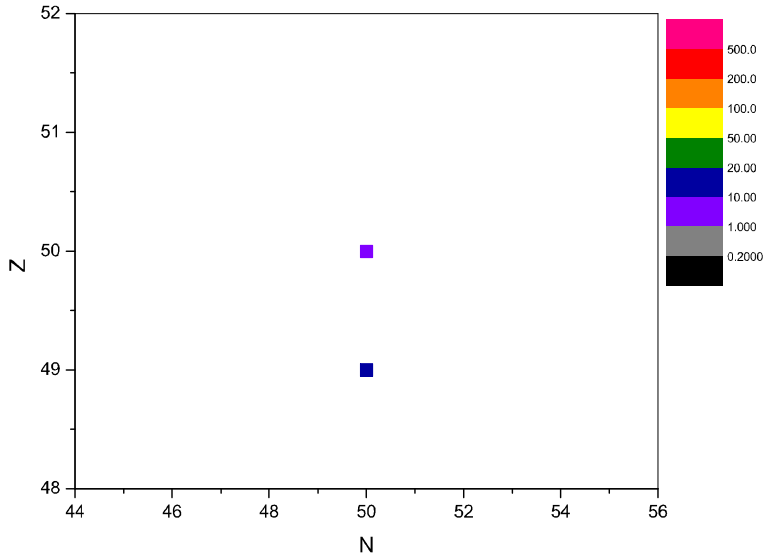

Figure 4.8. Distribution of isotopes that remain after two-stage separation of ^{100}Sn.

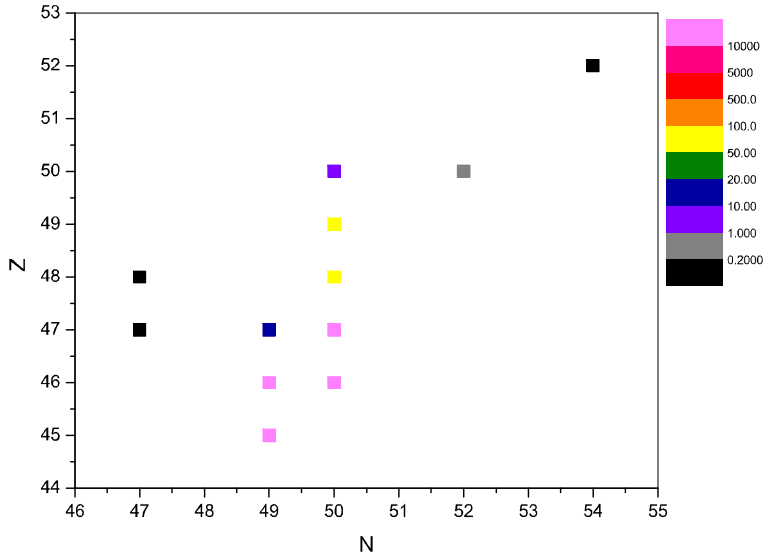

Figure 4.9. Distribution of isotopes that remain after one-stage separation of ^{100}Sn, including gas cell branch.

(Figure 4.10). The transmission was 13.1%. For this stage a slit setting of 0.025 m to 0.035 m in x was used. For the second stage, a wedge equal to 80% of the range was used with a slit setting in x of -0.05 m to 0 m. This resulted in a separation purity of 3.64×10^{-3}% after two separation stages (Figure 4.11). The second stage transmission was 6.1%.

While a thick wedge directly results in better mass and charge resolution, it has the downside of added straggling. For this reason, a thinner wedge (40% of the range) was used to try to improve the separation purity; however, this endeavor was not successful. The separation purity after two stages is just 5.89×10^{-4}%. It is necessary to keep a thick wedge in the second stage to keep close to maximum resolution. The gas cell branch yielded a separation purity of 2.94×10^{-4}% and a transmission of 24.8%.

4.2.4. Heavy Fission

^{132}Sn is a heavy fission product that is produced by the fission of a 200 MeV/u ^{238}U beam. To produce this beam, a 125 mg/cm^2 target and 800 mg/cm^2 wedge in the first stage were used. The slit setting in x at the end of the first stage was -0.06 m to -0.04 m to capture the bulk of the ^{132}Sn going into the second stage. The second stage contained an Al wedge equal to 49% of the range and had a slit setting in x of -0.1 m to -0.08 m. The separation purity at the end of the first stage was 1.15% with a transmission of 19.18% (Figure 4.13). The second stage improves the separation purity to 4.04%.(Figure 4.14). This also translates

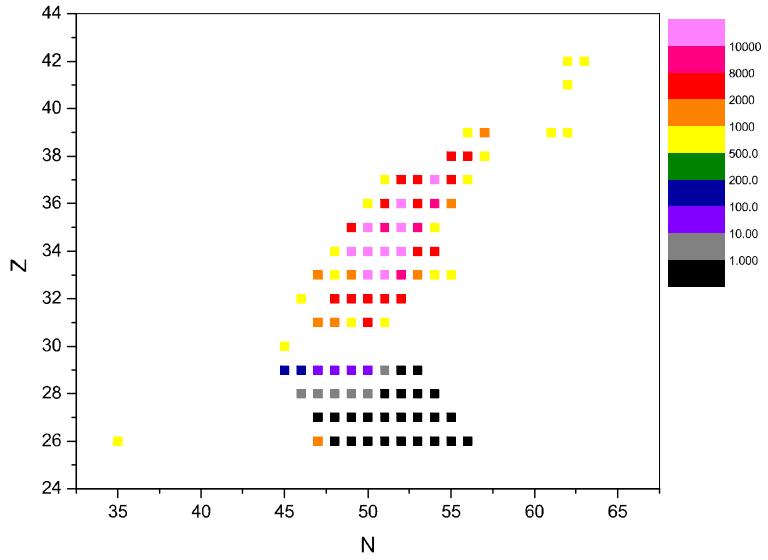

Figure 4.10. Distribution of isotopes that remain after one-stage separation of ^{78}Ni.

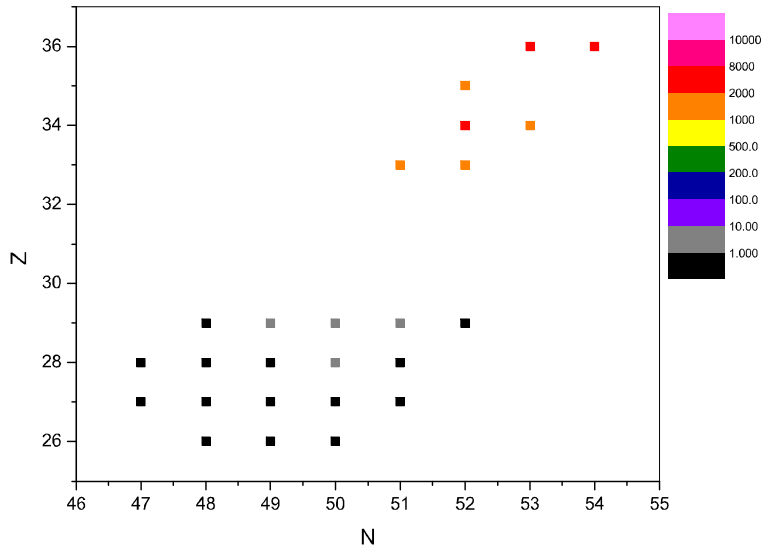

Figure 4.11. Distribution of isotopes that remain after two-stage separation of ^{78}Ni.

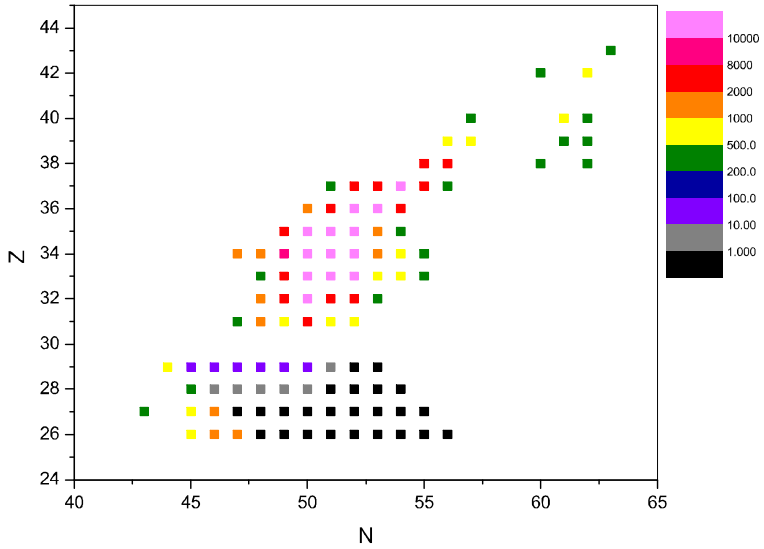

Figure 4.12. Distribution of isotopes that remain after one-stage separation of ^{78}Ni, including gas cell branch.

into greater transmission losses with a decrease to 3.2%. The gas cell branch has a separation purity that is almost identical to a first-stage separation at 1.52% (Figure 4.15). The transmission in this case is 17.6%.

^{199}Ta is also a heavy fission product of great interest. This isotope was produced by the fission of a 200 MeV/u ^{238}U beam incident on a 850 mg/cm^2 target. The first-stage wedge was 350 mg/cm^2, which corresponds to 70% of the range. In this case it was advantageous to increase the thickness of the wedge in the second stage to 80%. After a one-stage separation, the separation purity is 8.35×10^{-3}% with a transmission of 18.8 % (Figure 4.16). The second stage increases the separation purity significantly to 10.8% and the transmission is decreased to 7.9%

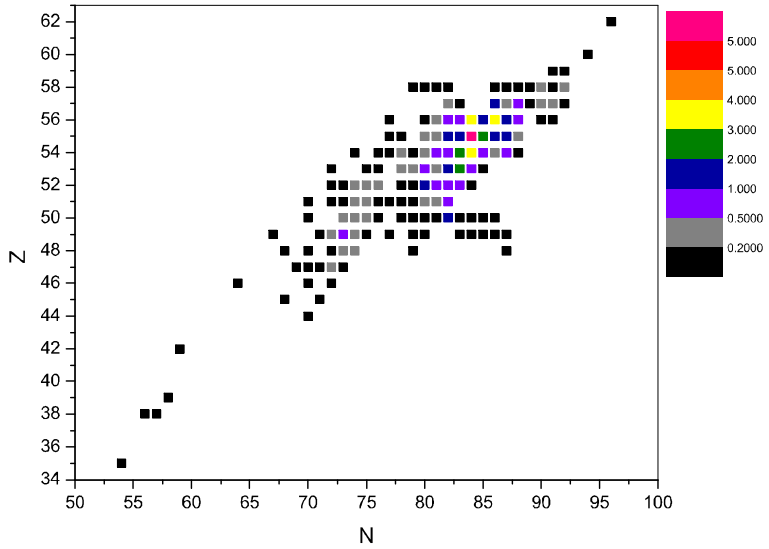

Figure 4.13. Distribution of isotopes that remain after one-stage separation of ^{132}Sn.

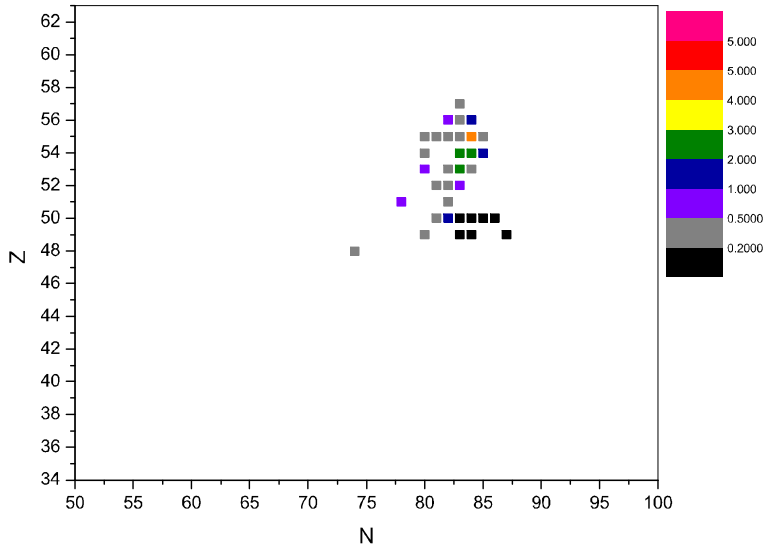

Figure 4.14. Distribution of isotopes that remain after two-stage separation of ^{132}Sn.

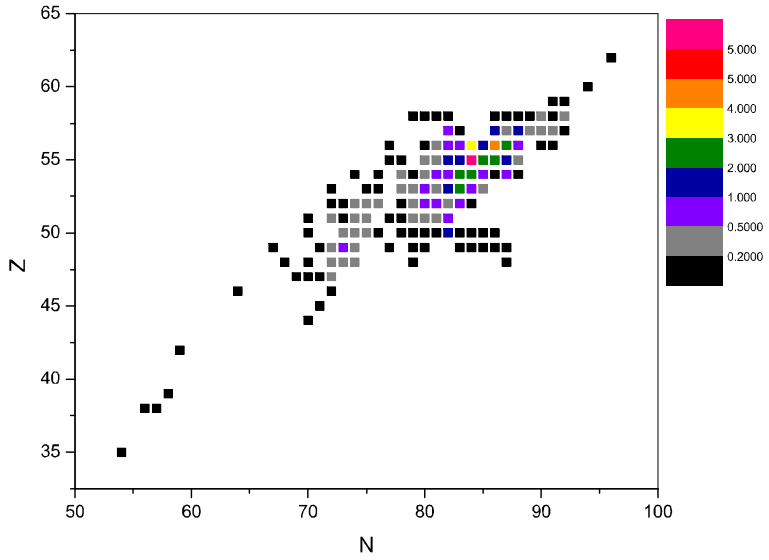

Figure 4.15. Distribution of isotopes that remain after one-stage separation of ^{132}Sn, including gas cell branch.

(Figure 4.17). The gas cell branch has a separation purity of 6×10^{-2}% and a transmission of 30.34% (Figure 4.18).

4.2.5. Approximations

Due to the extremely low cross-sections of the rare isotopes, some approximations must be used in order to get statistically significant results in the separation purity studies. The main approximation used is the weighting of the primary beam. For most of the cases presented, 10,000 primary beam particles are used for the primary beam. While this number is sufficient to accurately predict the dynamics of the beam, it is not, however, large enough to obtain an accurate numbers for the background contamination relative to the separated rare isotope beam. The

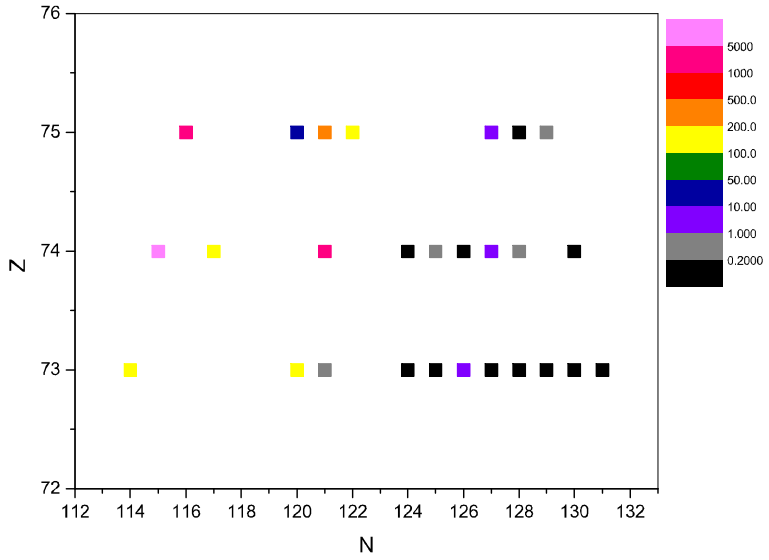

Figure 4.16. Distribution of isotopes that remain after one-stage separation of ^{199}Ta.

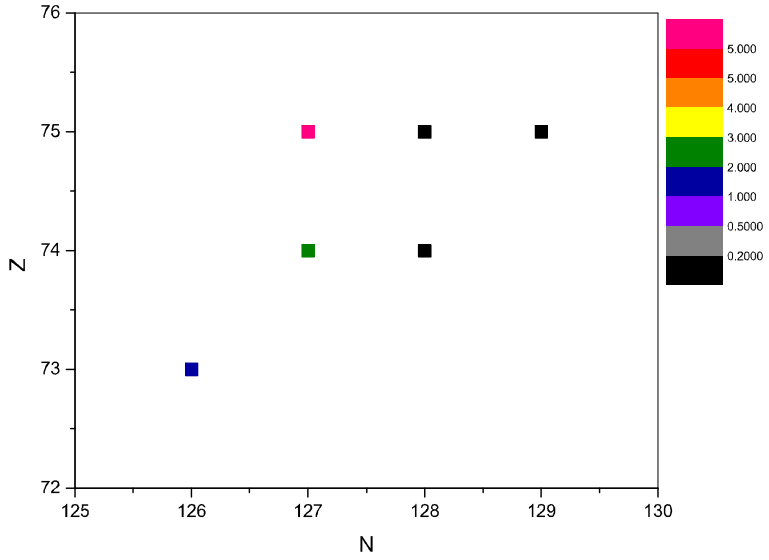

Figure 4.17. Distribution of isotopes that remain after two-stage separation of ^{199}Ta.

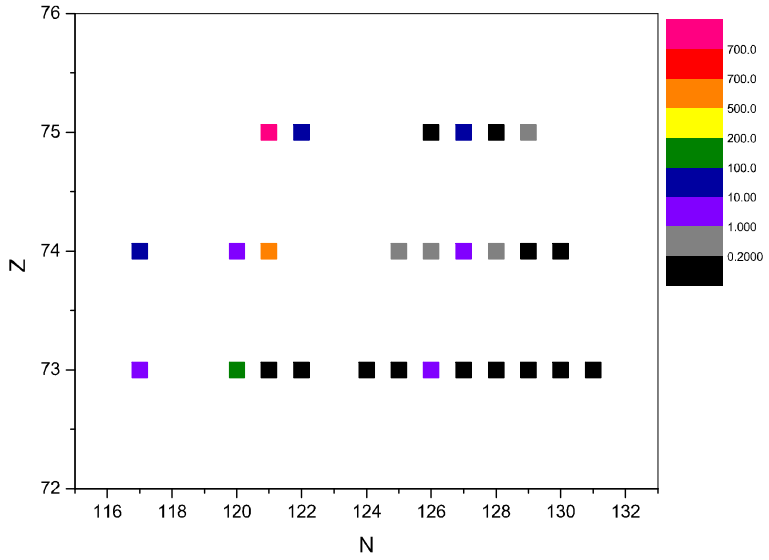

Figure 4.18. Distribution of isotopes that remain after one-stage separation of ^{199}Ta, including gas cell branch.

primary beam is weighted by a factor of 1000 in order to produce some of the very low-cross-section isotopes that would otherwise not have been produced by a 10,000-particle primary beam. In many cases, not even the isotope of interest is produced with a beam of 10,000 particles or even with the added weight factor of 1000. This leads to another approximation that must be made in some cases.

In these types of cases the following procedure is employed. First, run the code, calculating all fragmentation and fission reactions in the target. When this is complete, the isotopes that are produced are plotted in the N (neutron number) vs. Z (proton number) plane. In these cases the rare isotope is either produced in extremely low quantities or not at all. To produce them and the isotopes nearby, a box containing the rare isotope and its nearest neighbors in the NZ-plane is

constructed. In a second Monte Carlo target calculation each isotope in the box is produced in a fix quantity in each target slice. In the case of fission, since the cross-section depends on the energy, the number of isotopes that exist of each type at the end of the separation is scaled by the average cross-section in the target to get the actual number of particles that would exist in a realistic experiment.

To illustrate the necessity of these approximations, Table 4.2 shows how many primary beam particles would be necessary in each case to produce just one particle of the rare isotope. These numbers are for two optimized separation stages taking into account transmission losses along the separator due to magnet apertures and slits.

Currently, there are plans to extend the code for extreme computing. Parallel computing would allow for large numbers of primary beam particles to be used which would produce the appropriate number of rare isotopes to be tracked through the system. Approximations would not be necessary in this case.

Table 4.2. Number of primary beam particles required to form one particle of each listed rare isotope.

Rare Isotope	Cross-section (mb)	Number of Primary Beam Particles
^{14}Be	2×10^{-3}	1.13×10^{6}
^{100}Sn	7.12×10^{-9}	3.79×10^{12}
^{78}Ni	8.8×10^{-6}	1.04×10^{10}
^{132}Sn	9×10^{-2}	1.03×10^{6}
^{199}Ta	4.5×10^{-8}	1.02×10^{12}

CHAPTER 5

Sensitivity Studies

There are several errors that could occur in the construction and implementation of the fragment separator. Each of these types of errors can be analyzed using the powerful map computation capabilities of COSY. Among the errors that can occur are rotational and translational placement errors of the dipoles and quadrupoles, powering of quadrupoles, and thickness variations of the absorber wedge. To first order, the magnitude of these errors can be calculated by applying these errors systematically to each magnet or wedge in the fragment separator. The relative effect of each element can be seen by looking at the value of $(x|\delta_\pi)$ to first order. Second- and third-order effects are indicated by the map elements $(x|...\delta_\pi)$.

5.1. Magnet Errors

The first type of error is a tilt of the magnets (quadrupoles and dipoles) in x or y. It is the only magnet error, that has a first-order effect on the map. A tilt was applied to each magnet individually in x and then in y. The first-order map element $(x|\delta_\pi)$ was computed. In y, this quantity is zero in the case of all magnets. If the tilt is in x, however, it is nonzero for most magnets and is plotted

in 5.1. For all quadrupoles, $(x|\delta_\pi)$ is nonzero. In between the two dipoles it is positive and before the first and after the last it is negative. In contrast, for the dipoles $(x|\delta_\pi)$ is zero. The tilt has a small effect on the map, where the maximum value of $(x|\delta_\pi)$ is 0.045.

A tilt in x also leads to two second-order aberrations, namely, $(x|a\delta_\pi)$ and $(x|\delta\delta_\pi)$. The absolute value of the map elements corresponding to the aberrations are plotted in Figures 5.2 and 5.3. $(x|a\delta_\pi)$ is the largest map element and has maximum values for a tilt in x of the dipoles. The first dipole has a larger value, where $(x|a\delta_\pi) = 1.7$. For the second dipole, $(x|a\delta_\pi) = 1.2$. The quadrupoles in the first half of the one-stage separator overall have larger $(x|a\delta_\pi)$ compared to the second half. The largest multipole in the first half has $(x|a\delta_\pi) = 1.2$ and the largest in the second half has $(x|a\delta_\pi) = 0.45$. The last four quadrupoles have very little effect on $(x|a\delta_\pi)$ and it actually drops down to zero for the last two quadrupoles. $(x|\delta\delta_\pi)$ has similar behavior to $(x|a\delta_\pi)$ along the separator, but is less in magnitude (Figure 5.3). Again, the maximum values are for the dipoles, where $(x|\delta\delta_\pi) = 0.09$ and 0.062, respectively. The main different feature of the element is that it drops to zero for three magnet locations. The first two quadrupoles, central two, and last two all have essentially no effect on $(x|\delta\delta_\pi)$.

There are no first-order effects due to a tilt in y. In general, a tilt in y has a larger effect for quadrupoles at the beginning of the separator with the only exception being the quadrupole immediately after the first dipole where the map element $(x|b\delta_\pi)$ drops to zero (5.4). The effect decreases for magnets further

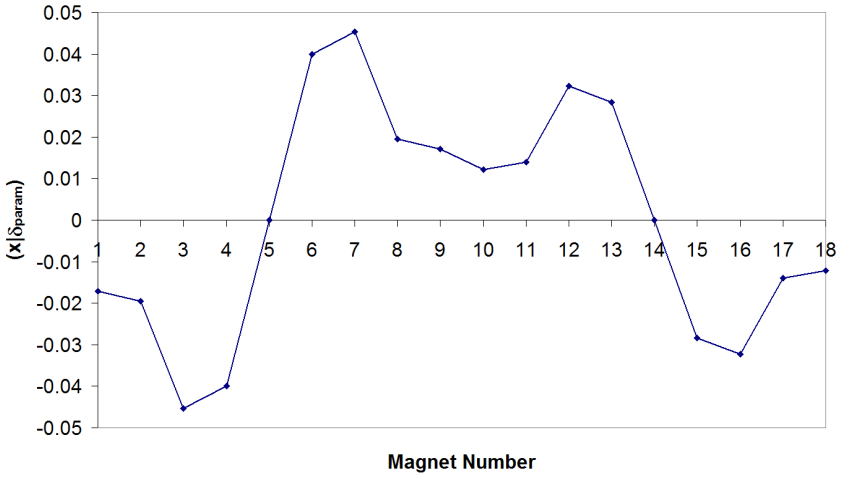

Figure 5.1. $(x|\delta_\pi)$ along the fragment separator for a tilt in x. The x-axis indicates the magnet number in order along the separator, where #'s 5 and 14 are the dipoles. All others are quadrupoles.

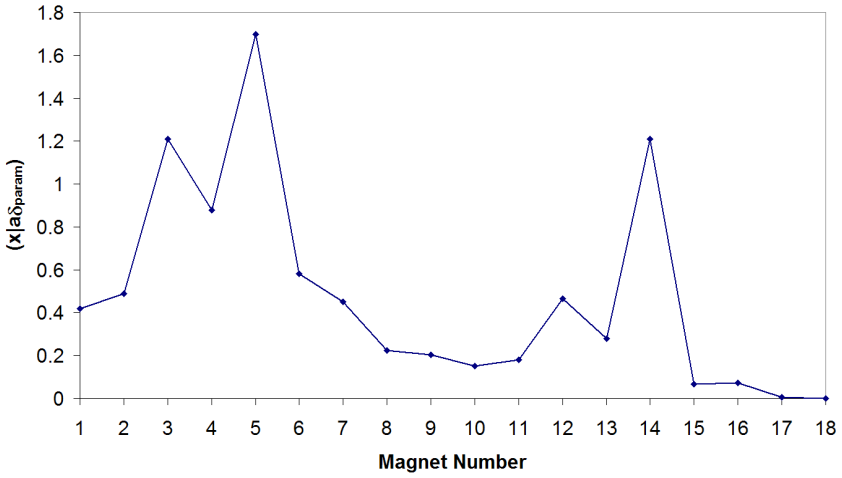

Figure 5.2. $(x|a\delta_\pi)$ along the fragment separator for a tilt in x. The x-axis indicates the magnet number in order along the separator, where #'s 5 and 14 are the dipoles. All others are quadrupoles.

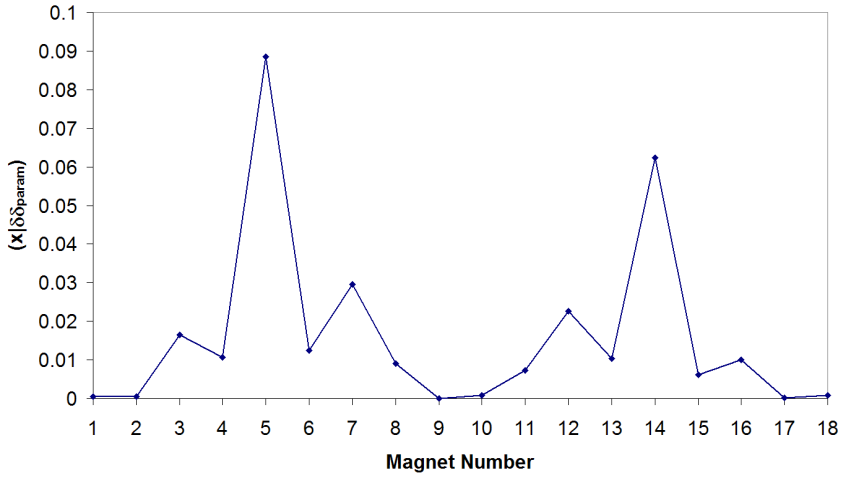

Figure 5.3. $(x|\delta\delta_\pi)$ along the fragment separator for a tilt in x. The x-axis indicates the magnet number in order along the separator, where #'s 5 and 14 are the dipoles. All others are quadrupoles.

along the separator. In this case the dipoles follow the same decreasing trend for $(x|b\delta_\pi)$ as the quadrupoles. This map element has a maximum value for the first quadrupole, which is 0.21, and is zero for the quadrupole after the first dipole and also the last quadrupole.

A rotation about the z-axis has a large effect mainly on the quadrupoles that are adjacent to the two dipoles. The map element $(x|b\delta_\pi)$ is also large for a rotation (Figure 5.5). Maxima occur for the quads next to the first dipole, where $(x|b\delta_\pi)$ is approximately 0.25. Both dipoles and also the quadrupoles farthest from the dipoles have the least influence on $(x|b\delta_\pi)$. Again, overall, the magnets in the first half have the most influence.

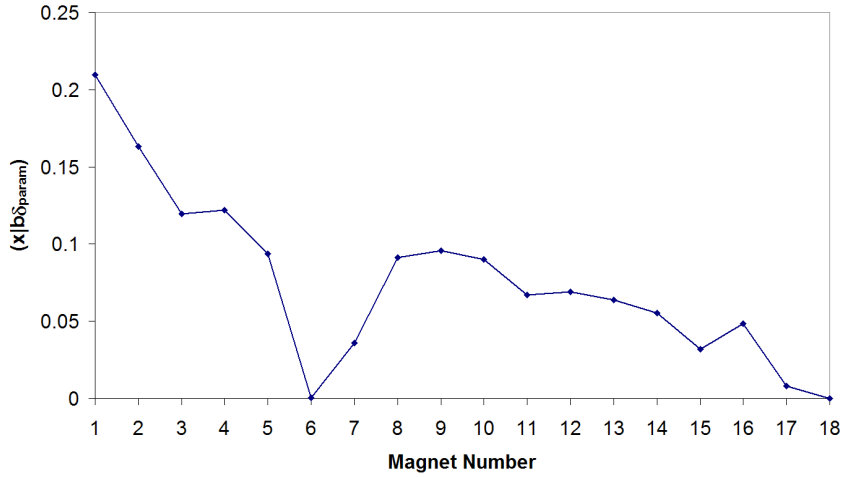

Figure 5.4. $(x|b\delta_\pi)$ along the fragment separator for a tilt in y. The x-axis indicates the magnet number in order along the separator, where #'s 5 and 14 are the dipoles. All others are quadrupoles.

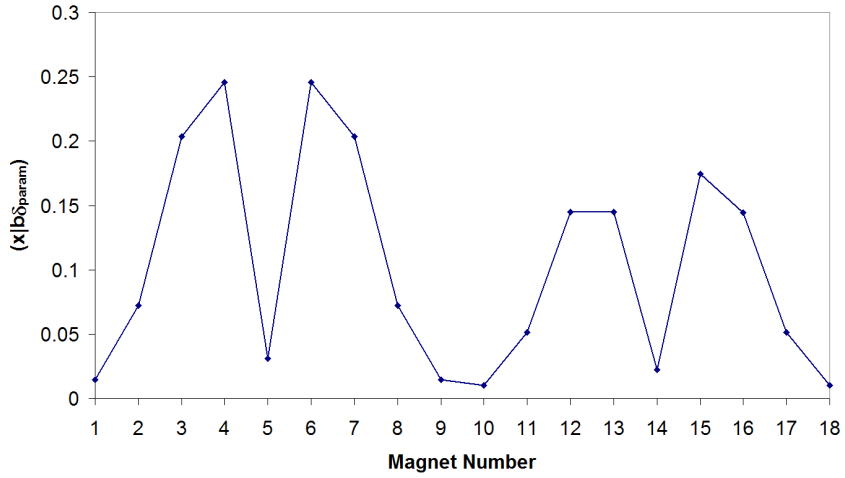

Figure 5.5. $(x|b\delta_\pi)$ along the fragment separator for a rotation about z. The x-axis indicates the magnet number in order along the separator, where #'s 5 and 14 are the dipoles. All others are quadrupoles.

Only the quadrupoles are subject to powering errors. Of all the map elements, $(x|a\delta_\pi)$ is the largest due to a powering error. The maximum value for$(x|a\delta_\pi)$ is 24 and it occurs for the quadrupoles that sit adjacent to the first dipole (Figure 5.6). A powering error for the quadrupoles next to the second dipole cause $(x|a\delta_\pi)$ to have a value of approximately 17. The quadrupoles adjacent to these magnets have less influence the farther from the dipole that they are. $(x|\delta\delta_\pi)$ is another second-order map element that is nonzero due to a powering error. This element has the characteristic that it is nonzero only for the quadrupoles that are in between the two dipoles (Figure 5.7). It is largest, reaching a maximum of 2.75, for the quadrupole next to the first dipole and gradually falls to a minimum of 0.35 for magnets at the center of the separator. This behavior is mirror symmetric about the center.

The largest aberrations result from the powering of the quadrupoles. In particular, magnets 4 and 5 have the largest effect on $(x|a\delta_\pi)$, and magnet 5 also has the largest effect on $(x|\delta\delta_\pi)$. The largest aberration is $(x|a\delta_\pi) = 1.20 \times 10^{-2}m$. The second largest is $(x|\delta\delta_\pi) = 1.54 \times 10^{-3}m$. Aberrations are calculated assuming the following initial conditions: $x, y = 0.5\ mm$, $a, b = 0.5$, $\delta = 0.154$, and $\delta_\pi = 0.01$.

5.2. Absorber Wedge Errors

The main errors involving the wedge absorber are thickness variations. The variations that have an effect up to third order include the length, angle, and curvature at the wedge. These all result from mistakes in the machining of the wedge.

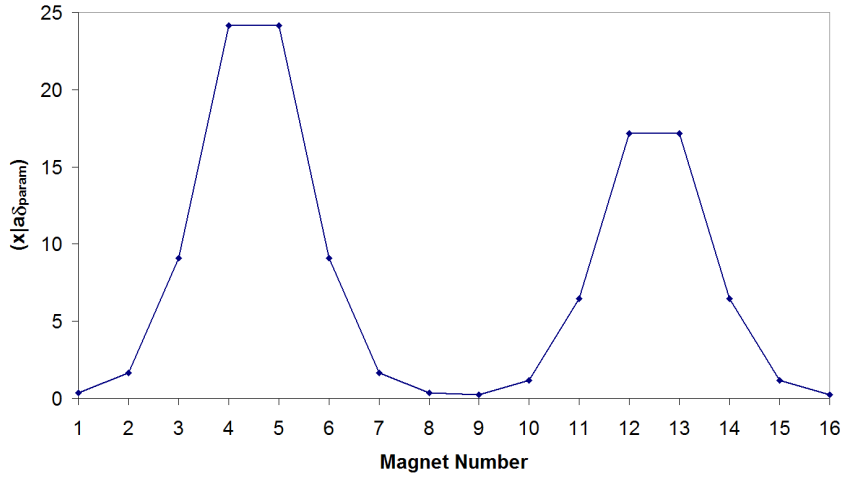

Figure 5.6. $(x|a\delta_\pi)$ along the fragment separator for a quadrupole powering error. The x-axis indicates the magnet number in order along the separator, where #'s 1-16 are all quadrupoles.

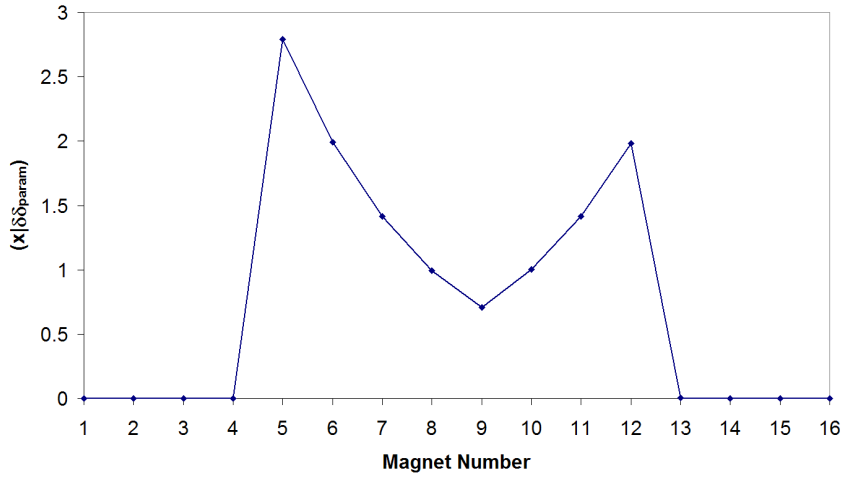

Figure 5.7. $(x|\delta\delta_\pi)$ along the fragment separator for a quadrupole powering error. The x-axis indicates the magnet number in order along the separator, where #'s 1-16 are all quadrupoles.

Often, it is very difficult to get a wedge machined precisely to specifications. For the machinist, the most difficult shaping to do is at higher orders. To second order, a curvature is difficult to produce exactly as needed. To third order, it just becomes increasingly difficult to impossible. All of the largest map elements that result from an error of the shaping of the wedge are represented in Tables 5.1-5.3 below in decreasing importance.

Of all the types of errors, the largest results from a variation in the length of the wedge. The largest map element that grows as a result of the length error is $(x|yy\delta_\pi) = 285.63$. Also large is $(x|yb\delta_\pi) = 181.159$. Fortunately, of all the thickness errors, the length is the easiest to correct.

Next are the shaping errors, namely the angle and the curvature. The third-order cubic shaping does not have an influence on the map below fourth order. For variations in the angle, $(x|a\delta\delta_\pi)$ and $(x|xa\delta_\pi)$ are the largest map elements equal to 10.836 and 9.92145, respectively. The largest for a variation in curvature are $(x|\delta\delta\delta_\pi) = 0.7462$ and $(x|x\delta\delta_\pi) = 0.6834$.

Aberrations may be computed by multiplying the map elements by realistic initial conditions. To compute the aberrations, the map elements above were multiplied by the assumed initial coordinates with $x, y = 0.0005m$, $a, b = 0.05$, and $\delta = 0.154$. δ_π is assumed to be equal to 0.01. The largest map aberrations that occur as a result of the wedge are from length errors, with the largest being $(x|a\delta_\pi) = 3.56 \times 10^{-3}m$. The second largest is $(x|\delta\delta\delta_\pi) = 2.45 \times 10^{-3}m$. These can be reduced by more precisely machining the wedge absorber. The largest

Table 5.1. Largest map elements that result from a variation in the reference length of the wedge. (In decreasing order of importance.)

Map Element	Value
$(x\|yy\delta_\pi)$	285.630
$(x\|yb\delta_\pi)$	181.159
$(x\|aa\delta_\pi)$	47.0466
$(x\|xa\delta_\pi)$	33.2297
$(x\|a\delta\delta_\pi)$	18.5310
$(x\|bb\delta_\pi)$	16.7989
$(x\|\delta\delta\delta_\pi)$	10.3277
$(x\|a\delta_\pi\delta_\pi)$	7.45861
$(x\|a\delta_\pi)$	7.12281
$(x\|x\delta\delta_\pi)$	4.89934
$(x\|xx\delta_\pi)$	4.11552
$(x\|x\delta_\pi\delta_\pi)$	2.16568
$(x\|\delta\delta_\pi\delta_\pi)$	1.11228
$(x\|\delta\delta_\pi)$	1.10967
$(x\|\delta_\pi)$	0.58399
$(x\|x\delta_\pi)$	0.27770
$(x\|\delta_\pi\delta_\pi\delta_\pi)$	0.22930
$(x\|\delta_\pi\delta_\pi)$	0.16305

Table 5.2. Largest map elements that result from a variation in the angle of the wedge. (In decreasing order of importance.)

Map Element	Value
$(x\|a\delta\delta_\pi)$	10.8362
$(x\|xa\delta_\pi)$	9.92145
$(x\|yb\delta_\pi)$	2.55005
$(x\|\delta\delta\delta_\pi)$	2.24432
$(x\|yy\delta_\pi)$	1.96572
$(x\|\delta\delta_\pi)$	0.88772
$(x\|x\delta_\pi)$	0.40652
$(x\|x\delta\delta_\pi)$	0.34556
$(x\|xx\delta_\pi)$	0.17692
$(x\|aa\delta_\pi)$	0.09534
$(x\|bb\delta_\pi)$	0.07221
$(x\|a\delta_\pi)$	0.00040

Table 5.3. Largest map elements that result from a variation in the curvature of the wedge. (In decreasing order of importance.)

Map Element	Value
$(x\|\delta\delta\delta_\pi)$	0.74623
$(x\|x\delta\delta_\pi)$	0.68345
$(x\|xx\delta_\pi)$	0.15649
$(x\|a\delta\delta_\pi)$	0.00068
$(x\|xa\delta_\pi)$	0.00031

aberration due to the angle of the wedge is $(x|\delta\delta_\pi) = 1.37 \times 10^{-3} m$. Errors in the curvature lead to the large aberration $(x|\delta\delta\delta_\pi) = 1.77 \times 10^{-4} m$. These aberrations are still slightly smaller than the aberrations induced by a powering error, though, which reaches a maximum value of $(x|a\delta_\pi) = 1.20 \times 10^{-2} m$.

CHAPTER 6

Gas Cell Branch

6.1. Map with Monochromatic Wedge

ISOL (Isotope Separation On-Line) is not sufficient to study some isotopes. These isotopes need to be studied at a lower energy, and therefore are stopped in a neutral He gas cell [**34**]. This low-energy regime is key for many nuclear physics and astrophysics experiments. For these cases, the second separation stage of a two-stage fragment separator is replaced with a monochromatizing gas cell branch. This is necessary in order to stop all of the particles selected in as small as a region as possible in the He gas cell. In some cases, after stopping the isotopes in the gas cell, they may be reaccelerated to a desired energy.

After the achromatic image of the first stage, the optics from the first half of the first stage are repeated followed by a wedge that is shaped to monochromatize the beam. When the map (in x, a, and δ) of the first stage is composed with map of gas cell branch, the following is obtained:

$$M_{tot} = \begin{pmatrix} -1-(\delta|x)_1(x|\delta)_2 & \\ 0 & \\ -(\delta|\delta)_{w2}(\delta|x)_1-(\delta|x)_{w2}-(\delta|x)_1(\delta|x)_{w2}(x|\delta)_2 & \\ 0 & (x|\delta)_2 \\ -1 & 0 \\ -(\delta|a)_2-\frac{(\delta|x)_2 l_{w2}}{2} & (\delta|\delta)_{w2}-(\delta|x)_{w2}(x|\delta)_2 \end{pmatrix}, \tag{6.1}$$

where the subscript $_1$ represents map elements from the first stage and the subscript $_2$ represents elements from the second stage. It is necessary to minimize $(\delta|a)_{tot}$ and $(\delta|\delta)_{tot}$ to make the wedge monochromatic. As in the achromatic case, the shape can be used to control $(\delta|x)_2$. By doing this we arrive at the following relations:

$$-(\delta|a)_{w2}-\frac{(\delta|x)_{w2}l_{w2}}{2}=0, \tag{6.2}$$

$$(\delta|\delta)_{w2}-(\delta|x)_{w2}(x|\delta)_2=0. \tag{6.3}$$

The condition stated by Eqn 6.2 is always true. However $(\delta|x)_{w2}$ is used to make Eqn 6.3 true. The map of the system is now given by:

$$M_{tot} = \begin{pmatrix} -1-(\delta|x)_1(x|\delta)_2 & 0 & (x|\delta)_2 \\ 0 & -1 & 0 \\ -(\delta|x)_{w2} & 0 & 0 \end{pmatrix}. \tag{6.4}$$

The monochromatic wedge is shaped to first order with an angle that meets these conditions. .At second and third order the map aberrations $(\delta|\delta\delta)_{tot}$ and $(\delta|\delta\delta\delta)_{tot}$, respectively, are cancelled by further shaping the wedge to have a curvature and a cubic term in the surface equation.

6.2. Monte Carlo Results

It is worthwhile to systematically investigate the function of the monochromatic wedge in Monte Carlo mode. There are five cases for which σ_{δ_E} is found for a variety of monochromatic wedge thicknesses. A lower value of $\boldsymbol{\sigma}_{\delta_E}$ indicates a better monochromatization. Along with σ_{δ_E}, the average energy of the beam is plotted as a function of the monochromatic wedge thickness (Figures 6.1-6.5). These plots are useful in determining the most desirable thickness for the monochromatic wedge. Depending on the nature of the experiment, different thicknesses may be useful depending on the final energy of the beam. It should be noted that there are no apertures in this study, so all particles of the separated isotope are accounted for in the calculation of σ_{δ_E}. Also, the same first-stage setup is used for all of the cases.

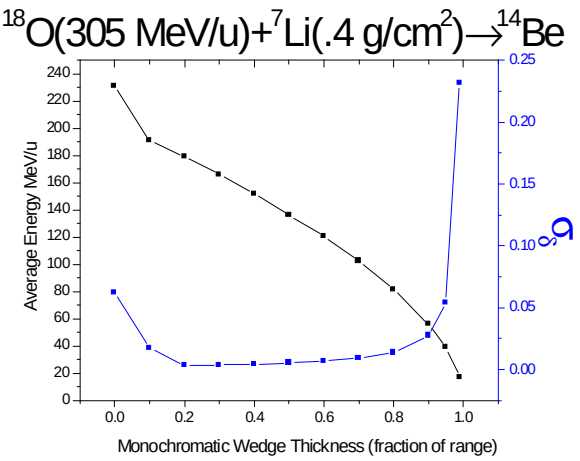

Figure 6.1. σ_{δ_E} and average energy of the ^{14}Be beam as a function of monochromatic wedge thickness after traversing the wedge.

In the ^{14}Be case, Figure 6.1 shows that the monochromatization of ^{14}Be is good for most wedge thicknesses. σ_{δ_E} remains rather stable and very small (≈ 0.01) for thicknesses of 20% of the range to about 80-90% of the range. It is obvious that after a certain point the wedge thickness gets to be too large ($\sigma_{\delta_E} = 0.05$ to 0.24) at approximately 90 to 95% of the range. There is no improvement in σ_{δ_E} and it increases dramatically after this point. This is a problem since the beam must lose most of its energy before it enters the gas cell following the wedge. This issue is discussed in the next section and a solution to this problem is presented.

^{78}Ni is a difficult isotope to monochromatize as well as a difficult isotope to obtain with good purity. According to the plot (Figure 6.2), there is a definite minimum σ_{δ_E} that occurs for a wedge thickness of 20% of the range. Here σ_{δ_E} is around 0.042. There is no monochromatization of the beam starting at wedge

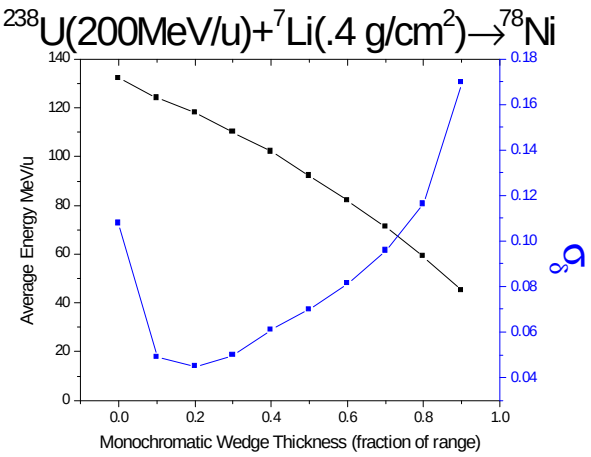

Figure 6.2. σ_{δ_E} and average energy of the ^{78}Ni beam as a function of monochromatic wedge thickness after traversing the wedge.

thicknesses around 80% of the range. For larger thicknesses, σ_{δ_E} grows to about 0.17.

^{199}Ta has virtually no monochromatization (Figure 6.3); however, σ_{δ_E} is kept constant for thicknesses of 0% of the range to about 50% of the range. The value of σ_{δ_E} in this region is 0.05. At a thickness of about 90% of the range it grows to about 0.47.

^{100}Sn is also not monochromatized for any thickness. For wedge thicknesses of 10% of the range to about 45% of the range, σ_{δ_E} ranges from about 0.025 to 0.05. This is shown in Figure 6.4.

^{132}Sn has monochromatization at thicknesses equal to 10 and 20% of the range ($\sigma_{\delta_E} \approx 0.075 - 0.1$). σ_{δ_E} steadily increases to about 0.32 and then decreases

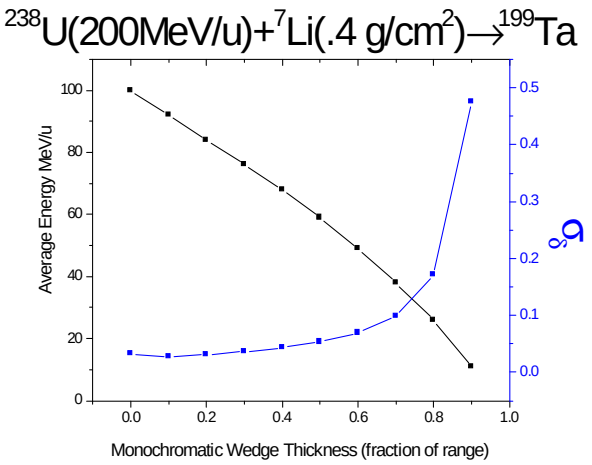

Figure 6.3. σ_{δ_E} and average energy of the ^{199}Ta beam as a function of monochromatic wedge thickness after traversing the wedge.

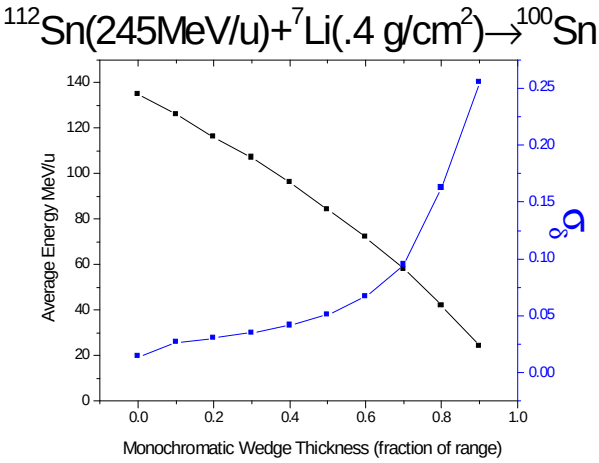

Figure 6.4. σ_{δ_E} and average energy of the ^{100}Sn beam as a function of monochromatic wedge thickness after traversing the wedge.

slightly to around 0.30 at thicknesses of 70 and 80% of the range. It increases again at 90% of the range back to 0.32.

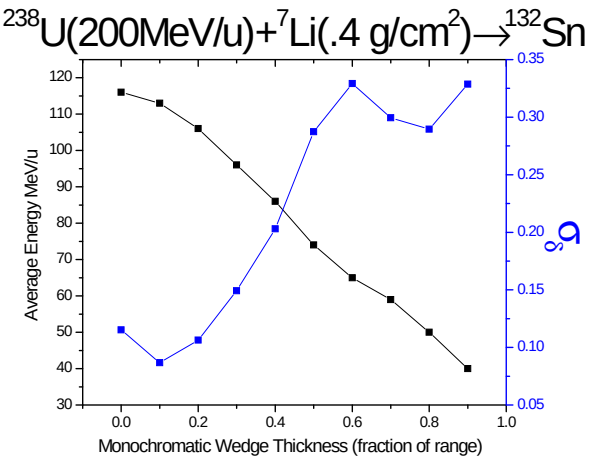

Figure 6.5. σ_{δ_E} and average energy of the ^{132}Sn beam as a function of monochromatic wedge thickness after traversing the wedge.

A second study was performed using the optimized first-stage setup described in the section Separation Purity (target thickness, wedge thickness, slit setting). In every case, a monochromatic wedge equal to 70% of the range was used. The effectiveness of the monochromatization can be described by the standard deviation of the coordinate δ, which is the energy deviation from the reference particle. Table 6.1 shows the values of σ_{δ_E} after the monochromatic wedge in the gas cell branch of the separator in order from best monochromatization to worst.

The easiest isotope to monochromatize with the gas cell branch is ^{100}Sn. The $\boldsymbol{\sigma}_{\delta_E}$ in this case is 0.004. This is not too surprising since it is a heavy fragmentation product that is emitted from the target with small angles and energy deviations. Also, since it is heavier, there is minimal straggling in the wedges, so $\boldsymbol{\sigma}_{\delta_E}$ is kept low. ^{199}Ta is the next best case, with $\boldsymbol{\sigma}_{\delta_E} = 0.11$. Although it is a fission product,

Table 6.1. Standard deviation of delta energy after the monochromatic wedge

Isotope	$\boldsymbol{\sigma}_{\delta_E}$
^{100}Sn	0.004
^{199}Ta	0.011
^{14}Be	0.013
^{78}Ni	0.021
^{132}Sn	0.028

since its mass is so large, the initial a_i's and δ_i's are not too large. ^{14}Be is a very light fragmentation product and is, therefore, subject to straggling in the wedges. The $\boldsymbol{\sigma}_{\delta_E}$ is close to that of the ^{199}Ta case and is equal to 0.013. ^{78}Ni and ^{132}Sn are medium mass fission products and have comparable $\boldsymbol{\sigma}_{\delta_E}$'s equal to 0.021 and 0.028, respectively. It would be expected that ^{78}Ni would be slightly worse than ^{132}Sn, but this can be easily explained by the slit settings chosen in each case in the first-stage separation.

After the monochromatizing wedge in the gas cell branch, the He gas cell is placed. The particles within the aperture of the gas cell are collected and stopped. A simulation of the stopping of the isotope ^{100}Sn (Figure 6.6) was performed using the program SRIM [**35**] by Guy Savard. From Figure 6.6, most of the ^{100}Sn particles are stopped at a depth of 2.2 cm in the gas cell. The particles stopped at this location are of one charge state. The other distribution is also ^{100}Sn, but a different charge state.

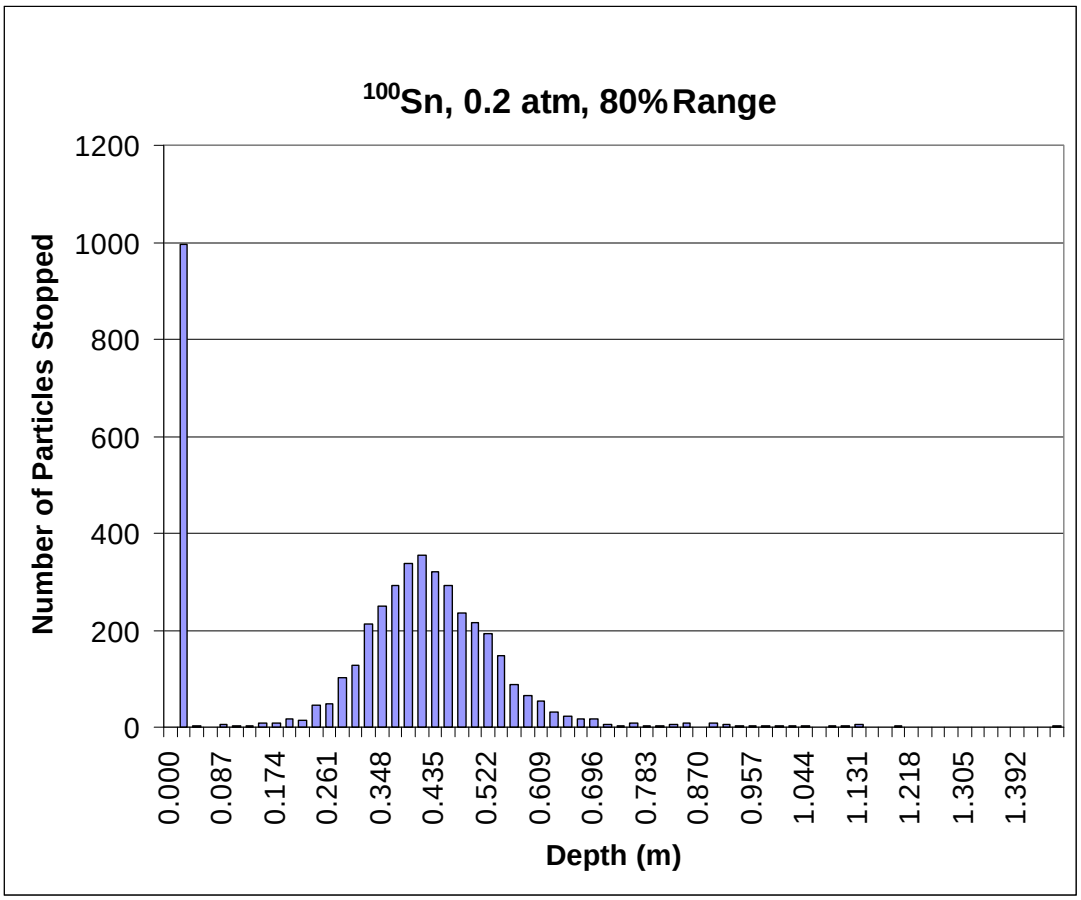

Figure 6.6. Number of particles stopped in the He gas cell as a function of the depth.

6.3. Optimization of ^{14}Be Gas Cell Branch

If the goal is to monochromatize a ^{14}Be beam and stop it in the gas cell, there are two possible ways of doing so. There is the method described above where a first-stage separator is followed by the optics of a half stage and a thick monochromatic wedge to slow down the beam enough for stopping in the gas cell. In the case of ^{14}Be there is a small momentum spread after one separation stage.

The momentum spread of the beam is well within the acceptance of the gas cell branch of the separator. For this reason it could be advantageous to slow down the beam as much as possible at the achromatic image location of the first stage. A thick uniform absorber was placed at this location so that most of the energy of the ^{14}Be beam is lost. A thin monochratic wedge is then used to monochromatize the beam going into the gas cell. Since ^{14}Be is light, it is subject to more straggling when passing through the absorber material. Since there is still a half-separation stage after this absorber, the effect of the straggling can be minimized and the beam can be better monochromatized.

These two methods of monochromatization were compared. In each case, a 305 MeV/u ^{18}O beam incident on a Li target with thickness equal to 30% of the range of the primary beam was used to produce the ^{14}Be beam. In the first stage, an Al achromatic wedge equal to 20% of the ^{14}Be range was used. In the case of using only a monochromatic wedge in the gas cell branch, a wedge with thickness 0.127153 m was used. The value of $\boldsymbol{\sigma}_{\delta_E}$ after the wedge was 2.28% (Figure 6.7). In the other setup, an absorber equal to 0.124168 m was used at the end of the first stage to slow down the beam. In the gas cell branch a wedge equal to 0.004 m was used to monochromatize the beam. In this case, $\boldsymbol{\sigma}_{\delta_E}$ was equal to 0.31%, a huge improvement over using just one wedge in the gas cell branch (Figure 6.8).

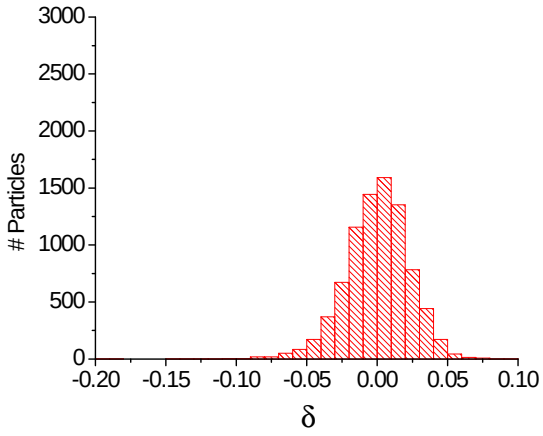

Figure 6.7. $\boldsymbol{\delta_E}$ after the wedge for one stage separation and gas cell branch with monochromatic wedge.

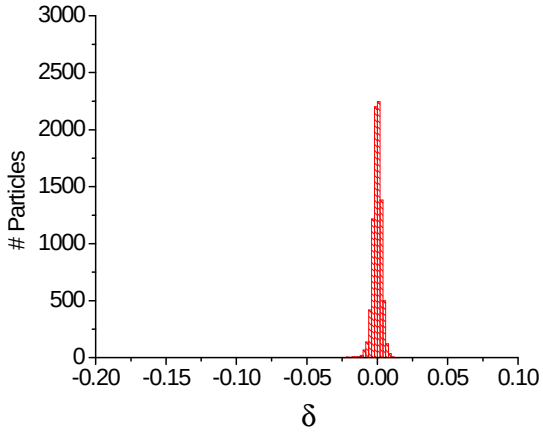

Figure 6.8. $\boldsymbol{\delta_E}$ after the wedge for one stage separation with additional wedge at achromatic image and gas cell branch with monochromatic wedge.

CHAPTER 7

Summary

There are many challenges that must be overcome in order to successsfully develop accurate simulation code for the development of next-generation fragment separators. The master version of COSY INFINITY has provided the basic DA framework for the accurate high-order modeling of beam dynamics in electromagnetic systems. The successful development of a hybrid map-Monte Carlo presented here has allowed the integration of beam-material interactions such as nuclear fragmentation and fission into electromagnetic systems for a cohesive and very accurate simulation of all aspects of a fragment separator, including target and absorber interactions and dynamics in one code. The developments made have been essential in order to compute important quantities that describe the quality of the fragment such as resolution and separation purity.

The implementation of auxiliary codes like ATIMA, GLOBAL, EPAX, and MCNPX into COSY has led to the most state-of-the-art computer code for modeling heavy-ions in a fragment separator system. The integration of ATIMA splines into COSY has given the user access to experimentally verified energy loss data for nuclei in matter. GLOBAL is the most reliable code for charge evolution of heavy-ions in matter. EPAX returns cross-sections for fragmentation reactions.

The integration of MCNPX data for the fission of a ^{238}U beam is a milestone that has led to the modeling of the unique beam dynamics of fission products.

Map methods available in COSY have made it easy to implement various symmetries in the setup of an aberration-free third-order design. These symmetries were necessary given the design constraints such as the 40 cm large aperture superconducting magnets with superimposed multipoles with minimal drift lengths (10 cm) between the magnets. The system was optimized for a 8 Tm ^{132}Sn beam with energy 200 MeV/u. The system that was chosen for additional study posessed maximum quadrupole fields of 2.4 T at 40 cm. An additional design that was aberration-free up to the tolerance of 1 mm had maximum quadrupole fields that were too large to realize in practice (5 T). The maximum octupole field was also too extreme (5.99 T).

The map representation of the energy absorber has made its integration seamless into the fragment separator. The effects of the wedge were studied systematically and all aberrations induced into the system by the wedge were reduced to the tolerance of 1 mm. The dispersion introduced by the wedge as a function of the wedge thickness goes from 10 cm for a wedge thickness of 20% of the range up to 50 cm for a wedge that is 60% of the range. There is little difference in the dispersion for a beam at 200 MeV/u and 400 MeV/u. The magnification of the separator without the wedge is unity. Once the wedge is added, it increases, doubling for a wedge that is 50% of the range for a ^{132}Sn beam. The optimal angle of the wedge to cancel the dispersion $(x|\delta)$ as a function of the ion species,

energy, and wedge thickness was determined. For a ^{100}Sn beam, the optimal angle of the wedge increases from 5 mrad at 300 MeV/u up to 25 mrad for a wedge that is 30% of the range of the beam. Though the wedge material of choice for most of the studies was Al, other materials were investigated as well. An achromatic beam can be attained for all species and wedge material combinations. Higher order shaping of the wedge using global numerical optimization procedures has been made possible with surface curvature and cubic terms added to reduce higher order aberrations up to third order induced by the wedge.

This optimized optical system was used to perform map-Monte Carlo code simulations to give the transmission and separation purity for a variety of separated isotopes. The transmission of ^{132}Sn in a two-stage separator has been studied in detail as a function of the target thickness and first and second wedge thicknesses. The best transmission attained for this isotope was over 60% for a target thickness of 10% of the range of the ^{238}U beam in a Li target and wedge thicknesses of 10% of the range. The transmission was found to decrease as the thickness of the target and wedges increased. In general, however, for practical target and wedge thicknesses, an average transmission of 50% is possible. The ability to track all particles in the fragment separator system has led to a practical solution to the location of a beam dump, which is immediately before the first wedge.

The separation purity, one of the most important quantities describing the quality of the fragment separator, has been calculated for four types of production mechanisms representing the extremes in beam dynamics. Fission products are

emitted from the target with large emittance and fragmentation products are usually contained in a very small phase space volume and are easier to capture and less prone to transmission losses. The separation purity of different isotopes can vary up to many orders of magnitude due to several factors, including beam dynamics complications and slit settings chosen or from isotopes having very similar rigidities. Also, contaminants may be produced in the energy degraders. The four cases studied for separation purity were light fragmentation (^{14}Be produced from ^{18}O), heavy fragmentation (^{100}Sn produced from ^{124}Xe), and light and heavy fission (^{78}Ni and ^{132}Sn produced from ^{238}U). The separation purity of each of these isotopes has been computed for an optimized setup (target, wedge thickness) determined from LISE++. The results were generally good, with ^{14}Be having a separation purity of 100% after just one separation stage. Results from other isotopes are also promising, yielding a 7.5% separation purity for ^{100}Sn after two separation stages, with only one major contaminant. The case of light fission remains challenging with ^{78}Ni having a separtion purity of 0.003% after two stages. The heavy fission product ^{132}Sn has been separated relatively well with a purity of 1.15% after one stage and 4.04% after two stages. Another heavy fission product, ^{199}Ta, has been separated with a purity of 10.8% after two stages. Gas cell branch results are also good. For a monochromatic wedge of 70% of the range for all isotopes, the gas cell branch results are as follows. Separation purity for ^{14}Be is 96.77% and for ^{100}Sn it drops down to 1.48×10^{-5}%. For ^{78}Ni the separation

purity is $2.94\times10^{-4}\%$ and for ^{132}Sn it is 1.52%. For ^{199}Ta the purity after the gas cell branch is 0.06%.

Errors in the system have been investigated analytically by looking at the effects of the errors on various map elements. The values of these map elements are in direct proportion to the degree of the effect of each systematic error. Errors may result from positioning of the magnets or machining of the wedge. After systematically examining the errors that can result from a magnet translation, tilt, rotation, or powering, the errors due to powering were the greatest with the most influence on the map element $(x|a\delta_\pi)$. For the central quadrupoles in the first half of the first stage and the second half of the first stage the effect was greatest with the map element $(x|a\delta_\pi)$ rising to about 25. However, the errors resulting from machining of the wedge are the most sensitive in the system. The largest map aberrations that grows as a result of a length error is $(x|a\delta_\pi) = 3.56\times10^{-3}m$. The second largest aberration is $(x|\delta\delta\delta_\pi) = 2.45\times10^{-3}m$. These are easy to correct by carefully machining the wedge and measuring to verify its correct length.

The monochromatic wedge in the gas cell branch has been studied analytically to second order, and the relationships among the wedge map elements have led to an optimized wedge to reduce the energy spread of the isotopes entering the He gas cell. All of the isotopes in the separation purity study were examined in the gas cell branch; however, for these studies no slits at the end of the first separation stage were used, so the full energy spread of the beam was seen. For ^{100}Sn, the standard deviation of the energy spread, σ_δ, at the end of the wedge was 0.4%.

This was the best monochromatization of the isotopes. For ^{132}Sn, the standard deviation grows to 2.8%.

A novel approach to monochromatizing a ^{14}Be beam has been developed by placing an additional absorber at the end of the first stage of the fragment separator. The standard deviation of the energy spread of the beam is over seven times smaller with the new setup. This concept may be applied to other light fragmentation beams like ^{14}Be.

The DA framework provided by COSY along with the Monte Carlo extensions developed in this thesis have provided the experimenter with an easy-to-use code which can be utilized to design a rare isotope experiment. Parameters of magnets, targets, and absorbers can be tested with the code to determine an optimized setup to achieve the best separation purity or transmission with a fragment separator.

The code development presented in this dissertation does not have limited applicability. It can be used to model fragment separator facilities that are in use today. These facilities include BigRIPS at RIKEN in Japan and SuperFRS at GSI in Germany. The hybrid map-Monte Carlo approach is unique to this code and cannot be found in any other existing codes at the present time.

References

[1] RISAC. Scientific Opportunities with a Rare-Isotope Facility in the United States. Technical report, NRC, 2006.

[2] J. Nolen. Overview of the U.S. Rare Isotope Accelerator Proposal. *Nucl. Phys.*, A734:661–668, 2004.

[3] Y. Yano. RI Beam Factory project at RIKEN. In *Proc. 17th Int. Conf. Cycl. Appl.*, pages 169–173, Tokyo, Japan, 2004.

[4] W. Henning. The GSI project: An International Facility for Ions and Antiprotons. *Nucl. Phys.*, A734:654–660, 2004.

[5] M. Lewitowicz. Physics with SPIRAL and SPIRAL2. Status of the EURISOL project. *Nucl. Phys.*, A734:645–653, 2004.

[6] A. Stolz, T. Baumann, T. Ginter, and D. Morrissey et al. Production of rare isotope beams with the NSCL fragment separator. *Nuclear Instruments and Methods Section B: Beam Interactions with Materials and Atoms*, 241:858–861, 2005.

[7] T. Kubo, K. Kuska, and K. Yoshida et al. Status and overview of superconducting radioactive isotope beam separator BigRIPS at RIKEN. *IEEE Transactions on Applied Superconductivity*, 17:1069–1077, 2007.

[8] U.S. Department of Energy Office of Public Affairs. U.S. Department of Energy Selects Michigan State University to Design and Establish a Facility for Rare Isotope Beams. http://www.energy.gov/print/6794.htm, 2008. www html page.

[9] U.S. Department of Energy Office of Public Affairs. Fact Sheet: Facility for Rare Isotope Beams (FRIB) Applicant Selection. http://www.energy.gov/print/6795.htm, 2008. www html page.

[10] O. Tarasov and D. Bazin. LISE++: design your own spectrometer. *Nuclear Physics A*, 746:411–414, 2004.

[11] M. Mazzocco, D. Ackerman, M. Blocke, and H. Geissel et al. MOCADI FUSION: Extension of the Monte-Carlo code MOCADI to heavy-ion fusion-evaporation reations. *Nuclear Instruments and Methods Section B: Beam Interactions with Materials and Atoms*, 266:3467–3480, 2008.

[12] L. Waters, G. McKinney, and J. Durkee et al. The MCNPX Monte Carlo radiation transport code. *Hadronic Shower Simulation Workshop. AIP Conference Proceedings*, 896:81–90, 2007.

[13] D. Brice. Stopping powers for electrons and positrons ICRU Report 37. *Nuclear Instruments and Methods in Physics Research Section B: Beam Interactions with Materials and Atoms*, 12:187–188, 1985.

[14] N. Mokhov, K. Gudima, and S. Mashnik. Towards a heavy-ion transport capability in the MARS15 code. *Radiation Protection Dosimetry*, 116:104–108, 2005.

[15] N. Mokhov and K. Gudima. Recent enhancements to the MARS15 code. In *10th Internatinal Conference on Radiation Shielding*, volume FERMILAB-Conf-04/053-AD, Portugal, 2004.

[16] H. Iwase, K. Nita, and T. Nakamura. Development of general purpose particle and heavy ion transport Monte Carlo code. *Journal of Nuclear Science and Technology*, 39:1142–1151, 2002.

[17] K. Makino and M. Berz. COSY INFINITY version 9. *NIM A*, 558:346–350, 2006.

[18] M. Berz. *Modern Map Methods in Particle Beam Physics*. Academic Press, San Diego, 1999.

[19] M. Berz. Differential algebraic formulation of normal form theory. In *Proc. Nonlinear Effects in Accelerators*, page 77, London, 1992. IOP Publishing.

[20] M. Berz et al. Publications. http://www.bt.pa.msu.edu/pub/.

[21] M. Berz. COSY INFINITY Version 7. In *1997 Particle Accelerator Conference*. APS, 1997.

[22] B. Erdelyi, L. Bandura, and J. Nolen. Code Development for Next-Generation High Intensity Fragment Separators. In *Proceedings 2007 Particle Accelerator Conference*, Albuquerque, 2007.

[23] K. Summerer and B. Blank. EPAX version 2: a modified empirical parameterization of fragmentation cross sections. *Nuclear Physics A*, 701:161C–164C, 2002.

[24] C. Scheidenberger, T. Stohlker, W. Meyerhof, H. Geissel, P. Mokler, and B. Blank. Charge states of relativistic heavy ions in matter. *Nuclear Instruments and Methods in Physics Research Section B: Beam Interactions with Materials and Atoms*, 142:441–462, 1998.

[25] H. Weick. http://www-linux.gsi.de/ weick/atima/. www html page.

[26] M. James, G. McKinney, J. Hendricks, and M. Moyers. Recent enhancements in mcnpx: Heavy-ion transport and the laqgsm physics model. *Nuclear Instruments and Methods in Physics Research Section A-Accelerators Spectrometers Detectors and Associated Equipment*, 562(2):819–822, 2006.

[27] B. Erdelyi, J. Maloney, and J.A. Nolen. Symmetry-Based Design of Fragment Separator Optics. *Phys. Rev. ST Accel. Beams*, 10(6):064002, 2007.

[28] S. Wolfram. *The MATHEMATICA Book*. Wolfram Media, 5th ed., 2003.

[29] B. Erdelyi, L. Bandura, and J. Nolen. Transfer map approach to and optical effects of energy degraders on fragment separators. *Phys. Rev. ST Accel. Beams*, 12(014003):14 pages, 2009.

[30] K. Makino and M. Berz. COSY INFINITY Version 9. *NIM A*, 558:346–350, 2006.

[31] L. Bandura, B. Erdelyi, and J. Nolen. Optical Effects of Energy Degraders on the Performance of Fragment Separators. In *Proceedings 2007 Particle Accelerator Conference*, Albuquerque, 2007.

[32] L. Bandura, B. Erdelyi, and J. Nolen. Beam Purity Studies for a Facility for Rare Isotope Beams. In *Proceedings 2009 Particle Accelerator Conference*, Vancouver, 2009.

[33] O. Tarasov and D. Bazin. LISE++ Version 8.0.2. http://groups.nscl.msu.edu/lise. www html page.

[34] Argonne National Lab Publication. ATLAS Upgrade Allows Scientists to Reach Even Further for the Stars. http://www.anl.gov/MediaCenter/News/2007/PHY070608.pdf.

[35] J. Ziegler. SRIM. http://www.srim.org.

[36] J. Grote, K. Makino, and M. Berz. Supplemental Manual for Wedge Tools in COSY INFINITY, 2005. Programming Manual.

[37] T. Barlow. COSY Absorber Addition Final Report, 2006. Programming Manual.

APPENDIX A

COSY EXTENSIONS AND USER'S MANUAL FOR FISSION & FRAGMENTATION

APPENDIX A

COSY Extensions User's Manual for Fission & Fragmentation

A.1. Physics Extensions

A.1.1. Procedures Visible to User

WAS <MODE>;

This procedure controls the wedge computation mode. If MODE=0, then the computations involving the absorber wedge cannot be executed. If wedge computations are desired, **WAS** must be called with MODE=1 just before the procedure **OV** is called.

WA <S1> <S2> <N> <LENGTH> <APERTURE>;

This allows for a wedge absorber with shaped entrance and exit surfaces to act on the map. [**36**] The physical properties of the absorbing material must be specified by calling BBC before WA, which sets the parameters for the BETHE-BLOCH formula described below. The entrance and exit surfaces are specified by S1, S2, and N, where S1 and S2 are two-dimensional arrays containing the coefficients of polynomials of order N describing the shape of the edge surfaces as

$$g_1(x,y) = \sum_{j,k=0}^{n} S_1(j+1,k+1)x^j y^k \tag{A.1}$$

$$g_2(x,y) = \sum_{j,k=0}^{n} S_2(j+1,k+1)x^j y^k \tag{A.2}$$

Figure A.1 shows the positive value of the polynomials g1 and g2 corresponding to the inward direction in the wedge. The polynomials g1 and g2 must not have nonzero constant parts, so S1(1,1)=S2(1,1)=0. For mirror symmetric edges, S1(j,k)=S2(j,k)$\forall 1 \leq j,k \leq$N+1. The LENGTH is the thickness that the reference particle sees.

The particles in the absorber lose energy depending on the distance s traveled within the absorber. This energy is given by the Bethe-Bloch formula:

$$\frac{dE}{ds} = -K\rho\frac{Z}{A}\frac{z^2}{\beta^2}\left(\log\left(\frac{2m_e c^2\beta^2\gamma^2 T_{\max}}{I^2}\right) - 2\beta^2 - \delta - 2\frac{C}{Z}\right) \tag{A.3}$$

where the parameters are given by Table A.1. T_{max} is the maximum energy transferred to a single electron in the absorber in a collision and given by the formula:

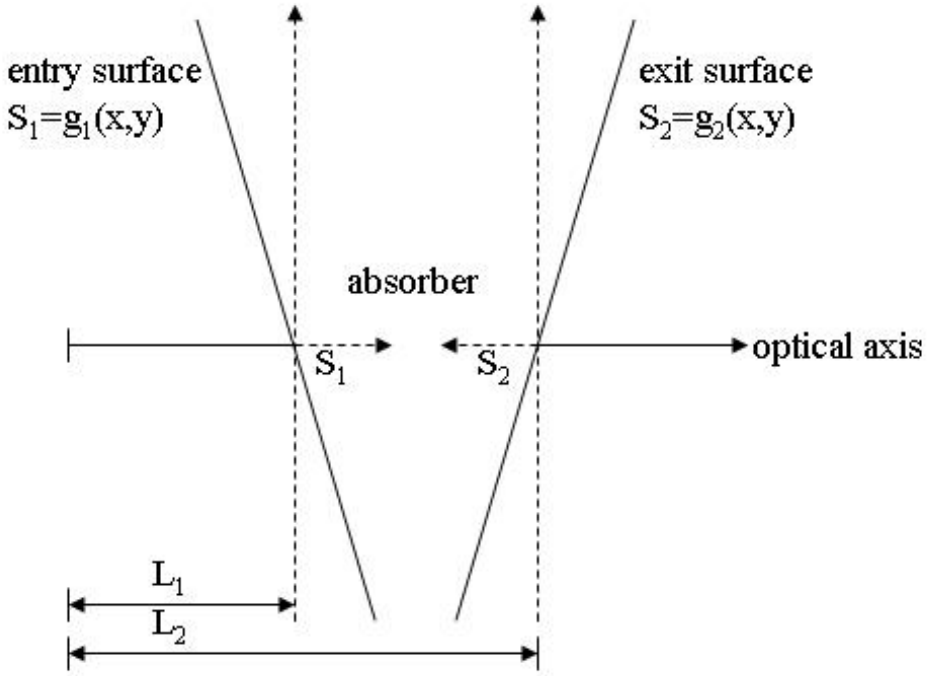

Figure A.1. The geometric setup for the procedures **WA** and **WL**.

$$T_{\max} = \frac{2m_e c^2 \beta^2 \gamma^2}{1 + 2\gamma \frac{m_e}{m_0} + \left(\frac{m_e}{m_0}\right)^2} \tag{A.4}$$

It should be noted that the function **BETHEBLOCH**(E) is a function of the total energy. In order to use this function to calculate the energy loss in the absorber, the procedure **BBC** must be called to set the parameters for **BETHE-BLOCH(E)**. If a different method for calculating the energy loss in absorber

Table A.1. Parameters for the Bethe-Bloch function.

Parameters
K=15.35375 $(\mathrm{MeV}\cdot\mathrm{cm}^3)(\mathrm{m}\cdot\mathrm{g})^{-1}$
Z is the nuclear charge of the absorber material
A is the nuclear mass of the absorber material
ρ is the density of the absorber material in g·cm^{-3}
I is the ionization potential in MeV
δ is the density correction parameter
C is the shell correction parameter

material is preferred, one must replace BETHEBLOCH(E) with a different function in cosy.fox. An example of this is in the procedure **NWA** described below.

BBC <Z> <A> <ρ> <I> <δ> <C>;

Sets the parameters for **BETHEBLOCH**(E) and must be called prior to **BETHEBLOCH**(E). Parameters are given in Table A.1.

EL <EI> <CTI> <L> <EF> <CTF>;

This procedure calculates the kinetic energy and time of flight times the speed of light as an expansion in the arclength s for the currently set beam after it traverses an absorber of thickness L. The input parameters are the the initial energy EI in MeV and time of flight times the speed of light, and the thickness L in meters. The output variables are the final energy EF and time of flight times the speed of light after the wedge. **EL** calls the function **BETHEBLOCH(E)**, so the user must call **BBC** with the correct parameters before calling **EL**.

WL <S1> <S2> <N> <L1> <L2> <LF>;

The function of this procedure is to calculate the total distance that a particle travels inside the wedge depending on its initial conditions. S1 and S2 are the

same two-dimensional arrays for the entrance and exit surfaces as described in **WA**. N gives the order of the polynomials describing the surfaces and L1 and L2 (Figure A.1) are the positions in meters of the entrance and exit surfaces, respectively. The output of the procedure is the distance LF, which gives the total length traveled inside the wedge for a particle depending on initial conditions as a DA vector taking into account the shaping of the edges.

EPAX <A> <Z> <TA> <TZ> <AF> <ZF> <CS>;

Returns the cross-section CS in mb for the production of the fragment given by AF, ZF (nuclear mass of fragment, nuclear charge of fragment) for the beam A, Z (nuclear mass of beam, nuclear charge of beam), and target TA, TZ (nuclear mass of target material, nuclear charge of target material).

GLOBAL <A> <Z> <Q> <E> <TA> <TZ> <L> <X>;

Given the nuclear mass (A), nuclear charge (Z), total charge (Q), and energy (E) in MeV/u of the beam and the nuclear mass (TA), nuclear charge (TZ), and thickness L of the target, returns the vector X containing up to 10 charge states.

ATMRNG <A> <Z> <E> <ABSA> <ABSZ> <RNGE> <RNGES>;

This procedure returns ATIMA spline interpolation data for the range and range straggling. In this case, the range RNGE and range straggling RNGES are returned in g/cm^2. The input values that are needed are the nuclear mass A, nuclear charge Z, and energy of the beam E in MeV/u. Also the absorber nuclear mass A (ABSA) and nuclear charge Z (ABSZ) must be provided.

ATMEN <A> <Z> <E> <TA> <TZ> <L> <EF> <I>;

Gets the final energy EF in MeV/u of the particle after passing through a thickness of L in mg/cm^2. A and Z are the nuclear mass and charge of the particle, respectively. TA and TZ are the nuclear mass and charge of the target material. E is the initial energy of the particle in MeV/u. EF returns the final energy in MeV/u and I returns 1 if the particle was stopped, otherwise 0.

ATMGAN <A> <Z> <E> <EF> <TA> <TZ> <AS>;

Gets the angular straggling AS in mrad given the initial and final energy of the beam (E,EF) in MeV/u, the beam nuclear mass (A) and nuclear charge (Z). TA and TZ are the nuclear mass and nuclear charge of the target material, respectively.

ATMGEN <A> <Z> <E> <EF> <TA> <TZ> <ES>;

Gets the energy straggling ES in MeV/u given the beam nuclear mass A, nuclear charge Z, initial energy E, and final energy EF. TA and TZ are the nuclear mass and nuclear charge, respectively.

ATMSSD <ISZIPPED> <DIRNAME>;

Sets the spline directory: DIRNAME is a string and ISZIPPED is 0 for unzipped, 1 for zipped. This is only necessary if splines are not in the default directory. By default, the splines will be located in the "splines_gz" directory located under the current directory and will be zipped, except under Windows, where they will be located in the splines directory and unzipped. The "masswbn" file will be located in the same directory as the splines.

ATMGSP <AF> <ZF> <TA> <TZ> <I> <N> <K> <T> <B>;

Returns spline info, N, K, T, B for fragment and target described by AF (nuclear mass of fragment) , ZF (nuclear charge of fragment), TA (nuclear mass of target material), TZ (nuclear charge of target material). It describes which spline to return: 0 for range spline, 1 for range straggling, 2 for angular straggling.

ATMINT <XT> <LXT> <LEFT> <MFLAG>;

Given vector XT of length LXT and value X, will determine LEFT and MFLAG using energy loss, straggling, and charge state information. Also, the shape of the target must be further specified in DA.

NWA <TA> <TZ> <RHO> <S1> <S2> <N> <L> <D>;

Computes the map of a shaped wedge absorber. TA and TZ are the nuclear mass and nuclear charge of the absorber material, respectively. RHO is the physical density of the absorber material. S1 and S2 are the same as described in procedure **WA** above. N is the order in **OV** + 1. L is the reference thickness in meters, and D is the preceding magnet's aperture in x (meters). **NWA** is different from **WA** in that it uses ATIMA splines rather than the Bethe-Bloch function to compute energy loss.

WEDGELEN <S1> <S2> <N> <XAP> <YAP> <X> <Z>;

The function of the procedure **WEDGELEN** is to compute the lengths X and Z as shown in Figure A.1. Input to this function are the arrays S1 and S2. Also N should be set to the order that is given by **OV** + 1. XAP and YAP are the apertures of the magnet that precedes the wedge in x and y, respectively.

ABSORBER <WT> <TA> <TZ> <RHO> <S1> <S2> <ORD> <L1> <L2> <L3> <NS> <DIR> <GLOBFL> <ESTRAG> <ASTRAG>;

The main function of **ABSORBER** is to call the procedure **SLICE** a specified number of times given by the input variable NS, which is the number of slices indicated for computing the target or absorber. To achieve the best approximation for the coordinates of the beam and for the number of fission products produced, a large number of slices should be used. A good rule of thumb for choosing the number of slices is about one slice per 10% of the projectile's range in the absorber or target material. More or less may be used, but the computation time increases linearly with the number of slices chosen.

Other input variables describe the properties of the absorber being used. These define the material and the shape, accordingly. TA and TZ are the absorber's nuclear mass A and nuclear charge Z and RHO is the physical density. S1 and S2 are two-dimensional arrays which determine the entrance and exit surfaces of the wedge. The polynomials are described in the procedure **WA**. If an absorber of uniform thickness is desired, then these should be set to zero.

L1, L2, and L3 are lengths of different parts of the absorber in meters. In Figure A.2, L1 is equal to X, L2=X+Y, and L3=X+Y+Z. In the case of a unshaped absorber, X and Z are zero.

The order for the map computation is given by the variable ORD. It cannot have a value greater than the value of the order set by the procedure **OV**. S1 and

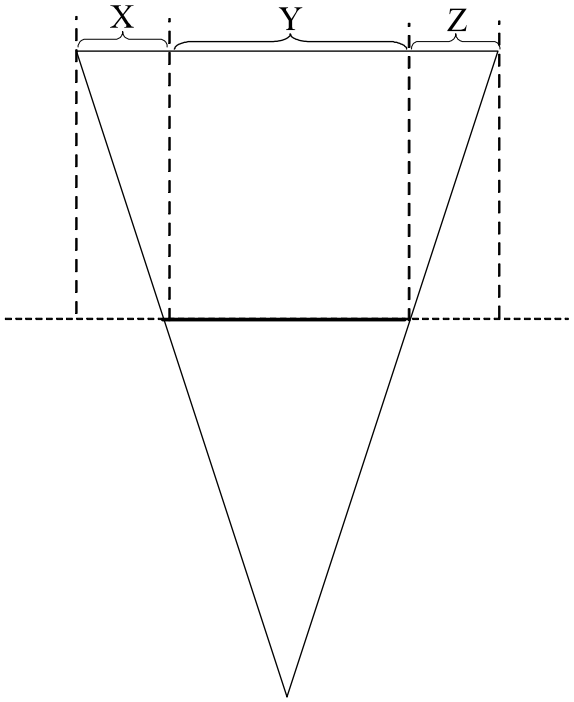

Figure A.2. Diagram illustrating lengths X, Y, and Z for a wedge-shaped absorber.

S2 will only use terms up to the order set by ORD. DIR is the directory where the particle and isotope files are located for transport through the absorber.

GLOBFL, ESTRAG, and ASTRAG are flags for charge exchange, energy straggling, and angular straggling, respectively. There are three options for GLOBFL. If it is set to 0, then no charge state is calculated. All isotopes remain fully stripped as they pass through matter. If it is set to 1, then the charge state of each particle is calculated by the thickness of absorber that it sees. If GLOBFL is set to 2, then the average thickness seen by each isotope is used to assign a charge state. GLOBFL=2 is much faster than GLOBFL=1 and gives the same result

if a statistically significant number of particles is used for large enough thickness. ESTRAG and ASTRAG compute the energy and angular straggling in matter by ATIMA splines if they are set equal to 1. They are turned off if set to 0.

SLIT <XMIN> <XMAX> <YMIN> <YMAX> <DIR> <SLTS> <PBSV>;

The main function of SLIT is to create a slit of a specified size. Particles that pass through the slit continue to be transported. The particles that don't pass through the slit are "lost" and the x and y coordinates are written to a file. When calculating the transmission of a beam, including background, in the separator, the procedure SLIT is used. There are several functions of the procedure and several files produced. The aperture size for the slit must be input. XMIN and XMAX are the coordinates in x for the slit and YMIN and YMAX are the coordinates in y in meters. DIR is the directory where the particle files to be evaluated are located and also where the files produced by this procedure are created. SLTS is a flag for turning the procedure on (SLTS=1) or off (SLTS=0). PBSV is a flag that is equal to 1 if the primary beam coordinates are to be saved in the file "primbeam.dat." Otherwise it is off and equal to 0. The file "apertures.dat" is generated and includes the slit number in the system as well as the nuclear mass A, nuclear charge Z, and number of particles of each isotope that exist after SLIT is executed. Also, for each slit, the file "slit#.dat" is created and the A, Z, and x and y coordinates of the particles lost at the slit are written to the file.

CALCAVGS <SEPA> <SEPZ> <SEPQ> <DIR> <AVGEN> <AVGRIG> <AVGQ> <XMIN> <XMAX> <YMIN> <YMAX> <QTOT> <AVGS>

<SIGMAQ> <SIGMA>;

CALCAVGS is a procedure that is used to retrieve the parameters that are necessary for the tuning of the separator. SEPA and SEPZ are the nuclear mass A and nuclear charge Z of the isotope one wishes to separate. SEPQ can be set equal to a particular charge state or set to 0 to compute the parameters of the beam in terms of the average charge state. DIR is the directory where the files are located. AVGEN (average energy), AVGRIG (average rigidity), and AVGQ (average charge state) are output from the procedure and used to set the next section of the separator by calling the procedure RP. If SEPQ is not equal to 0, then AVGQ is equal to SEPQ. If SEPQ is equal to 0, then AVGQ is the average charge state. XMIN, XMAX, YMIN, and YMAX are the minimum and maximum x and y coordinates computed from the particle files located in DIR. QTOT is always the average charge state over all particles of the specified isotope. AVGS is an array with five components that gives the averages of each phase space coordinate. SIGMAQ is the standard deviation of the charge states. SIGMA is an array with five components that gives the standard deviation of each phase space coordinate.

RECALCDELTA <EZEROOLD> <EZERONEW> <DIR>;

As the reference particle passes through material, it loses energy. Since the δ-coordinates of all particles are in terms of this energy, they must be recalculated since different particles may lose energy at different rates. EZEROOLD is the reference energy before the absorber material. EZERONEW is the energy of the

reference particle after it has passed through the material. DIR is the directory of the particle files which must be modified.

A.1.2. Procedures Not Directly Visible to User

SLICE

Contains procedures necessary to calculate parameters for each slice of absorber material:

CALCAVGTHK

Returns average thickness of material in a slice by the function AVGTHICK.

CALCPARAM

Returns average energy, standard deviation, and mean from interpolations of fission dynamics.

AMD

Applies map to distribution of particles. Contains the function PARTTHICK to calculate the thickness of absorber that each particle sees.

COORDUPDATE

Updates particle coordinates and charge state data from parameters returned from GLOBAL (charge state) and ATIMA (energy and angular straggling).

DRIFTMAP

Calculates the map of a drift of a specified length.

GENERATE <J> <A> <Z> <DIR>;

The procedure **GENERATE** is used to produce a primary beam with a Gaussian distribution defined in the procedure **SB** which must be called with **GENERATE**. J is the number of primary beam particles desired. The maximum number allowed is J=2147483647. DIR is the directory in which the particle coordinate files are to be created.

PRIMARYBEAM <A> <Z>;

This procedure sets the nuclear mass A and nuclear charge Z of the primary beam macroparticles.

TPMM <DIR>

Transports particles by momentary map. DIR is the directory where the particle files are located.

A.2. File Operations and Bookkeeping

RAOPEN <UNIT> <FILENAME> <MODE>;

Opens a file for random access [**37**]. MODE is 1 to modify an existing file, 2 to create/overwrite, 3 to append (creating the file if it doesn't exist).

RACLOS <UNIT>;

Closes file.

RAAPND <UNIT> <REC> <STR>;

Appends STR to the file specified by UNIT, and returns its record position REC.

RAWRIT <UNIT> <REC> <STR>;

Overwrites the record position REC with STR. REC=0 indicates writing at the current position.

RADEL <UNIT> <REC>:

Marks the indicated record as deleted. REC=0 indicates deleting the record at the current position.

RAUPDT <FILENAME>;

Updates the file specified by FILENAME. This removes deleted records, and modifies the position of existing records. This must be called when the file is closed.

FREN <FILENAME> <NEWFILENAME>;

Renames FILENAME to NEWFILENAME. The file names can include full paths.

FDEL <FILENAME>;

Deletes FILENAME if it exists.

FDDEL <DIRECTORY>;

Deletes DIRECTORY if it exists.

FCPY <FILENAME> <DIRECTORY>;

Copies FILENAME to DIRECTORY.

FMKDIR <DIRECTORY>;

Creates DIRECTORY.

GAUSSIAN(SIGMA);

Function returns a random number chosen according to a Gaussian distribution given the standard deviation SIGMA.

RAND(VAR);

Function returns a random number chosen according to a uniform distribution within the range -VAR to VAR.

APPENDIX B

DATA FILE STRUCTURES

APPENDIX B

Data File Structures

The user specifies a main directory which contains all subdirectories files related to the run. The files ISOTOPES.DAT and PARTICLESAAAZZZ.DAT are updated after each slice of target or wedge material and at several key locations in the separator. There are several directories set up to store the ISOTOPES.DAT files and the PARTICLESAAAZZZ.DAT files as well as the files HISTORY.DAT, APERTURES.DAT, and SLITXX.DAT.

The format of ISOTOPES.DAT is as follows. The first line of the file gives the total count of all particles being tracked through the system. The second number gives the number of different types of isotopes being tracked. The third number gives lists the LastID, which is the highest unique ID which has been given to a particle. The subsequent lines of the file give the A, Z, and particle count for each isotope being tracked. The old files describing the particle counts after earch slice are renamed ISOTOPES.XX, where XX is the slice number. Figure B.1 is a sample ISOTOPES.DAT file from a fragment separator run set up to separate the isotope ^{100}Sn.

The PARTICLESAAAZZZ.DAT file is updated at each point that the ISOTOPES.DAT file is updated. For each isotopes that exists in the ISOTOPES

```
TOTAL PARTICLES:        6458
NUM OF ISOTOPES:          20
LAST ID:                   0     4872244
BELOW IS A, Z, and COUNT for each isotope
  10    6           1
  14    7           1
  18    9           2
  20   10           1
  23   12           1
  26   13           1
  94   47          20
  97   47          49
  95   48          34
  98   48        1748
  99   49        2245
 101   49           2
 100   50        2272
 102   50           1
 104   50           1
 105   51          39
 106   52          37
  92   45           1
 105   50           1
 103   49           1
```

Figure B.1. The file "ISOTOPES.DAT" from a sample run.

file, a PARTICLESAAAZZZ file will exist that contains the phase space data for each particle as well as a unique identifying ID number for each particle. A sample file, "PARTICLES094047.DAT," is shown in Figure B.2. The first number that appears is the total number of particles of the isotope A=94, Z=47. This number should always match the number listed in the current ISOTOPES.DAT file. The subsequent lines contain the phase space information for each particle of the isotope. The first number is an ID, which will be zero for almost all cases. The second number is the unique ID for the particle. Next, the horizontal position coordinate x is listed in m. Then, the horizonal angle a is listed in radians. The vertical position y is given in m, and the vertical angle b is given in radians. The next column is the rigidity deviation from the reference particle defined as $\delta_{rig} = \frac{\delta_{rigparticle} - \delta_{rigrefparticle}}{\delta_{rigparticle}}$. In the last column, the energy deviation is given.

The HISTORY.DAT file records the creation of new particles from the old for each slice in target or absorber wedge material. In Figure B.3 the first line is the slice number from a sample run where ^{238}U was used as the primary beam. The subsequent lines list the isotopes that are produced by the fragmentation or fission of the ^{238}U beam in the first target slice. The word "PRODUCED" is followed first by the A of the isotope that fragments or fissions as well as that particle's Z number. Listed next is the new particle's A and Z. This recording process is repeated for all slices of material.

```
 20.000000000000000
 0    233840  46  0.960628716E-01 -0.119479162E-02  0.374699954E-03 -0.224015246E-02  0.265341922E-01 -0.517476772E-01
 0    233925  46  0.976664431E-01  0.151457555E-02  0.385515918E-03 -0.390381423E-02  0.281927635E-01 -0.488865260E-01
 0    233955  46  0.914367295E-01 -0.186551576E-02  0.516066335E-03 -0.910881398E-02  0.260856324E-01 -0.525208786E-01
 0    721609  46  0.816610955E-01 -0.166817696E-02  0.787576131E-04  0.262077048E-02  0.236174747E-01 -0.567708050E-01
 0    721743  46  0.105000074E+00  0.178381673E-02 -0.458397976E-03  0.471823422E-02  0.290615852E-01 -0.473863654E-01
 0   1207434  46  0.863535556E-01 -0.284835311E-02  0.431604102E-03 -0.469980142E-02  0.250035947E-01 -0.543849883E-01
 0   1207439  46  0.943342938E-01 -0.656471462E-02 -0.450444293E-04  0.217353040E-02  0.256794910E-01 -0.532207428E-01
 0   1207479  46  0.865856750E-01 -0.152675532E-01  0.900183297E-04 -0.483865383E-02  0.232620152E-01 -0.573822379E-01
 0   2176750  46  0.967607344E-01  0.906057147E-02 -0.119222064E-03  0.255893170E-03  0.262886533E-01 -0.521709544E-01
 0   2176929  46  0.107057101E+00 -0.853507263E-02 -0.791014763E-03  0.123212016E-01  0.292561821E-01 -0.470502323E-01
 0   2661424  46  0.919693802E-01  0.850655099E-02 -0.491111624E-03  0.493183252E-02  0.262706759E-01 -0.522019421E-01
 0   2661454  46  0.962069148E-01 -0.272167818E-02 -0.599824250E-03  0.572619237E-02  0.271531192E-01 -0.506803904E-01
 0   2661530  46  0.999367560E-01  0.118448001E-02 -0.908316214E-03  0.116128306E-01  0.285826773E-01 -0.482133946E-01
 0   3146032  46  0.796059042E-01 -0.106457810E-01  0.110634403E-03 -0.493678204E-02  0.222190385E-01 -0.591753612E-01
 0   3146097  46  0.955188944E-01  0.614141533E-02 -0.531641715E-03  0.757967370E-02  0.277762427E-01 -0.496053793E-01
 0   3630906  46  0.950876583E-01  0.192821148E-02  0.217408543E-03 -0.227403424E-03  0.264007748E-01 -0.519776809E-01
 0   4115868  46  0.938027200E-01  0.796482697E-03  0.132288783E-03 -0.321621716E-02  0.261423155E-01 -0.524231857E-01
 0   4115938  46  0.877527874E-01  0.903630802E-03 -0.674182689E-03  0.912435040E-02  0.247281391E-01 -0.548593010E-01
 0   4600374  46  0.851162407E-01 -0.331873901E-02  0.975280196E-04 -0.444487564E-02  0.234608918E-01 -0.570401661E-01
 0   4600639  46  0.660936300E-01 -0.582248197E-02  0.161438391E-03 -0.754965112E-02  0.191115526E-01 -0.645097046E-01
```

Figure B.2. The sample file "PARTICLES094047.DAT."

```
SLICE          1
Produced:   238   92    3    2          1
Produced:   238   92    4    2         15
Produced:   238   92    5    2         12
Produced:   238   92    6    2        313
Produced:   238   92    8    2         11
Produced:   238   92    9    2         13
Produced:   238   92   10    2          5
Produced:   238   92    5    3         39
Produced:   238   92    6    3        150
Produced:   238   92    7    3        319
Produced:   238   92    8    3        104
Produced:   238   92    9    3         25
Produced:   238   92    7    4         10
Produced:   238   92    9    4         76
Produced:   238   92   10    4        102
Produced:   238   92   11    4         11
Produced:   238   92   12    4          1
Produced:   238   92    8    5          3
Produced:   238   92   10    5         28
Produced:   238   92   11    5         38
Produced:   238   92   12    5         27
Produced:   238   92   13    5          3
Produced:   238   92   11    6          2
Produced:   238   92   12    6         16
Produced:   238   92   13    6         20
Produced:   238   92   14    6         18
Produced:   238   92   15    6          5
Produced:   238   92   14    7          5
Produced:   238   92   15    7         10
Produced:   238   92   16    7          3
Produced:   238   92   17    7          5
Produced:   238   92   16    8          2
Produced:   238   92   17    8          1
Produced:   238   92   18    8          4
Produced:   238   92   19    8          2
Produced:   238   92   19    9          1
Produced:   238   92   20   10          1
Produced:   238   92   22   10          1
```

Figure B.3. Part of a sample HISTORY.DAT file.

APPENDIX C

EXAMPLE OF INPUT CODE

APPENDIX C

Example of Input Code

There are several parameters that must be input to the Monte Carlo code that are unique to the case that the user wants to look at. These parameters are summarized in short in Table C.1 and a sample case is shown in Figure C.1.

Table C.1. Input parameters for Monte Carlo code.

Input Parameters
Directory name
Directory name for files to be used (previously created), including flag for use of files
Directory location for ATIMA splines
Flags to fit wedges to a particular computation order (up to order of map computations)
Flag for GLOBAL charge state computations (on/off) (averages/particle by particle)
Flags for energy and angular straggling given by ATIMA (on/off)
Flag for magnet apertures (on/off)
Option to call several fragment separator optics designs
Option to call only certain sections of fragment separator
Order for map computations
Primary beam A, Z, energy, number of particles, weight factor
Standard deviations in all coordinates for primary beam
Separation isotope A, Z, and Q
Target A, Z, density, thickness, number of slices
Each wedge A, Z, density, thickness, number of slices
Reference energy for secondary beam (if files from a different run are used)

COMMAND	DESCRIPTION
DIR:='100Sn';	DIRECTORY FOR ISOTOPE AND PARTICLE FILES
ODIR:='100Sn_target';	DIRECTORY FOR ISOTOPE AND PARTICLE FILES
TARGFLAG:=0;	=0 FOR TARGET CALCULATIONS ON, =1 FOR USE OF PARTICLE FILES IN OLD DIRECTORY
ATMSPL:='/cygdrive/c/cosy/splines/';	=0 IF ATIMA SPLINES ARE IN DEFAULT DIRECTORY
OBYO1:=2;	NO FIT=0, FIT ALL ORDERS=1, ORD. BY ORD.=2, 1ST WEDGE
OBYO2:=2;	NO FIT=0, FIT ALL ORDERS=1, ORD. BY ORD.=2, 2ND WEDGE
GLOBFL:=2;	GLOBAL OFF=0, GLOBAL PART. BY PART.=1, AVGS=2
ESTRAG:=1;	ENERGY STRAGGLING OFF=0, ENERGY STRAGGLING ON=1
ASTRAG:=1;	ANGULAR STRAGGLING OFF=0, ANGULAR STRAGGLING ON=1
SLTS:=1;	SLTS=0 FOR MAG. AP. OFF, SLTS=1 FOR ON
FRAGDES:=1;	FRS DESIGN: ORIGINAL=1, ALTERNATE=2
FRSSEGMENT:=1;	=1 FOR 1ST HALF,=2 FOR WHOLE,=-1 FOR 2ND HALF ONLY, =3 FOR 1ST HALF WITH GAS CELL BRANCH, =-3 ONLY GAS CELL BRANCH
ORDER:=3;	ORDER OF COMPUTATION FOR MAP
PBA:=124;	PRIMARY BEAM A (nuclear mass)
PBZ:=54;	PRIMARY BEAM Z (nuclear charge)
PBE:=245;	PRIMARY BEAM ENERGY (MeV/u)
PBNUM:=10000;	# OF PRIMARY BEAM PARTICLES
PBSV:=0;	=1 TO SAVE PRIMARY BEAM PARTICLES AT EACH SLIT, MUST HAVE SLTS=1
WT:=1000;	WEIGHT FACTOR FOR PRIMARY BEAM
SBX:=.001/6;	X FOR PROCEDURE SB (m)
SBA:=.002/3;	A FOR PROCEDURE SB (rads)
SBY:=.001/6;	Y FOR PROCEDURE SB (m)
SBB:=.002/3;	B FOR PROCEDURE SB (rads)
SBD:=.002/3;	DELTA FOR PROCEDURE SB
TARGA:=7;	TARGET A (nuclear mass)
TARGZ:=3;	TARGET Z (nuclear charge)
RHOTARG:=.534;	TARGET DENSITY (g/cm^3)
TTHK:=.5;	TARGET THICKNESS (FRACTION OF RANGE)
NST:=10;	NUMBER OF SLICES TARGET
SEPA:=100;	A OF ISOTOPE TO BE SEPARATED (nuclear mass)
SEPZ:=50;	Z OF ISOTOPE TO BE SEPARATED (nuclear charge)
SEPQ:=0;	Q (CHARGE) OF ISOTOPE TO BE SEPARATED,IF=0, THEN AVERAGE VALUES ARE CALCULATED FOR ALL CHARGE STATES OF ISOTOPE IN CALCAVGS
WEDGA:=27;	A OF WEDGE1 (nuclear mass)
WEDGZ:=13;	Z OF WEDGE1 (nuclear charge)
WEDGRHO:=2.702;	DENSITY OF WEDGE1 (g/cm^3)
WTHK:=.3;	WEDGE1 THICKNESS (FRACTION OF RANGE)
NSW:=5;	NUMBER OF SLICES WEDGE1
WEDGA2:=27;	A OF WEDGE2 (nuclear mass)
WEDGZ2:=13;	Z OF WEDGE2 (nuclear charge)
WEDGRHO2:=2.702;	DENSITY OF WEDGE2 (g/cm^3)
WTHK2:=.44;	WEDGE2 THICKNESS (FRACTION OF RANGE)
NSW2:=5;	NUMBER OF SLICES WEDGE2
WEDGAMW:=27;	A OF WEDGEMW (nuclear mass)
WEDGZMW:=13;	Z OF WEDGEMW (nuclear charge)
WEDGRHOMW:=2.702;	DENSITY OF WEDGEMW (g/cm^3)
WTHKMW:=.7;	WEDGE THICKNESS (FRACTION OF RANGE)
NSWMW:=7;	NUMBER OF SLICES WEDGEMW

Figure C.1. Sample input commands and description for Monte Carlo code.